The influence of baryons on dark matter halos: A cosmic tale of stripping, destruction, and statistics

JACK DAVID RICHINGS

The influence of baryons on dark matter halos

A cosmic tale of stripping, destruction, and statistics

Jack Richings

A thesis presented for the degree of
Doctor of Philosophy

Institute for Computational Cosmology
Department of Physics
Durham University
United Kingdom

October 2019

The influence of baryons on dark matter halos

A cosmic tale of stripping, destruction, and statistics

Jack Richings

Submitted for the degree of Doctor of Philosophy

October 2019

Abstract: Small scale tests of the nature of dark matter require simulations which incorporate baryonic physics. In this thesis we study how the inclusion of baryonic physics affects the abundance and properties of dark matter halos and their substructures. We introduce a new high-resolution hydrodynamical zoom simulation of a 10^{13} $M_\odot$ galaxy group, which we use to study the properties of halos and subhalos relevant to strong lensing tests of the cold dark matter model. We also compare two hydrodynamical simulations of Milky Way-mass halos, Apostle and Auriga. We find that the number of subhalos, as well as the slope of the subhalo mass function and the subhalo velocity distribution, is altered significantly depending on the implementation of baryonic physics.

Contents

List of Figures

List of Tables

Declaration

The work described in this thesis was undertaken between October 2015 and August 2019 while the author was a research student under the supervision of Prof. Carlos S. Frenk and Prof. Adrian R. Jenkins in the Department of Physics at the University of Durham. This work has not been submitted for any other degree at the University of Durham or any other University.

Chapter 3 is based on

Subhalo destruction in the Apostle and Auriga simulations

[arXiv:1811.12437 [astro-ph]

J. Richings, C. Frenk, A. Jenkins, A. Robertson, A. Fattahi, R. Grand, J. Navarro, R. Pakmor, F. Gomez, F. Marinacci (submitted to MNRAS)

All figures in this thesis have been produced by the author. The copyright of this thesis rests with the author. No quotation from it should be published without prior written consent and information derived from it should be acknowledged.

Acknowledgements

The path from starting my PhD to finishing this thesis has been a rather circuitous one. It has required a great deal of support, guidance and friendship to see it through to its completion. I must firstly thank my supervisors Carlos and Adrian. Carlos, your irrepressible enthusiasm and knack for spotting when something is fishy have shaped almost every aspect of this thesis. Adrian, your impeccable attention to detail has elevated the quality of my science at every turn. I would like to thank you both for the patience you have shown me as I slowly found my way over these last four years, and a special thank you must go to Adrian for all his help when he didn't even sign up to supervise me.

The ICC has been a wonderful family to be a part of, and I shall miss it deeply. The camaraderie of my thesis-writing cohort has sustained me - long evenings in shanty town were made bearable by the company of Oliver, Piotr, Stefan and Griffin. Thank you to Andrew, whose assistance has undoubtedly improved this thesis. Thank you to Louise for being a willing debate partner, and Tom Rose for moderating us. I must give special mention to the boundless curiosity and enviable work ethic of Tom Callingham, who has been a wonderful friend, rubber duck, and badminton buddy. Thank you to my housemates, for your friendship and tolerance of my strange behaviours. Thank you Phil, for the many years of academic brotherhood, and for the transport, be it unprompted hospital visits or piggy backs to the department. Thank you Kris, for never being boring, and for always sharing your tiramisu. Thank you Jacob, for always lending a helping hand, and always being willing to talk. Thank you also Matheus, your enthusiasm, companionship, and top-quality rapping made

sure that our adventures in Italy, Switzerland and Portugal were some of the happiest times of my life.

Few things have taken up more of my time, or given me more happiness and satisfaction than the Durham University badminton team. You have been a consummate architect of distraction, and the source of many of my most important friendships through these last four years. I would especially like to thank Clemens, Kieran, Tom, Ho Chi and the boys of the mens second team for their companionship, guidance and sense of humour.

This thesis would not have been started let alone finished without the incredibly generous sponsorship of David and Anne. I have found our discussions illuminating, your advice sage, and your hospitality impeccable. I cannot express how deeply grateful I am for giving me this opportunity.

Thank you to my family, who have always supported my academic endeavours in any way they can, and who have always provided a welcome retreat from the Durham bubble. Finally, Amy - thank you for cultivating my love of houseplants, for the unceasing provision of snacks, and for being a wonderful partner. I have loved every minute.

"In the beginning the Universe was created. This has made a lot of people very angry and been widely regarded as a bad move."

— from *The Restaurant at the End of the Universe* by Douglas Adams

Dedicated to

Steve, Rachel, Lizzie,
Betty, and Nel

Chapter 1

Background and Theory

1.1 The standard cosmological model

The standard model of cosmology describes the composition of our Universe, and its evolution from an initially tiny, hot, dense, and almost completely homogeneous region to the complex large scale structure we observe today. Hubble (1929) found that more distant galaxies are moving away from the Milky Way faster than nearby galaxies. This relationship demonstrates that the Universe is expanding, and has led astronomers to conclude that the Universe we see today was at one point contained in an extremely small region of space. This idea, known as the *Hot Big Bang* model, is the foundation for our current understanding of the evolution of the Universe.

In the standard model of cosmology, the present day Universe has three principal components; baryonic matter, dark matter and dark energy. Baryonic matter comprises only 5% of the energy density of the Universe, and is described by the standard model of particle physics. Around 25% of the the energy density of the Universe is in the form of cold collisionless non-baryonic matter, referred to as *cold dark matter* (CDM). The dark matter interacts only very weakly with standard model particles, and so the only current evidence for its existence comes from its gravitational interactions with baryonic matter. The remaining 70% of the energy density of the Universe takes the form of dark energy, often denoted with the symbol Λ. The defining quality of dark energy is its persistence, unlike matter or radiation its density remains constant as the Universe expands. Between them, dark matter and dark energy contribute over 95% of the total energy density of the Universe in the standard cosmological model, and for this reason the standard model of cosmology is also referred to as the ΛCDM model.

1.1.1 The evidence for dark matter

By measuring the velocity dispersion of galaxies in a cluster, Zwicky (1937) presented the first evidence that much of the matter in the Universe is non-luminous. Further evidence for dark matter was found by Rubin & Ford (1970), who measured the rotation curve of nearby galaxies and found that the total mass implied by their results exceeded the observed luminous mass by a factor of roughly five. Further research (Einasto et al., 1974; Ostriker et al., 1974; Rubin et al., 1980) established the current consensus that virutally all visible galaxies reside at the centre of massive dark matter halos.

The current conception of dark matter was first described by Peebles (1982), who proposed that the dark matter was composed of weakly-interacting massive particles (WIMPs). These WIMPs are thought to be a fundamentally new form of matter, not described by the Standard Model of particle physics. The best evidence for the non-baryonic nature of dark matter comes from the cosmic microwave background (CMB). The sizes and distribution of temperature anisotropies of the CMB imply that around 30% of the energy density of the Universe is in the form of matter, whilst only 5% of the energy density is accounted for by baryons.

Gravitational lensing also provides strong evidence for the existence of dark matter. The trajectory of a photon is bent when it passes by a massive object. By measuring the distortion of light from distant galaxy clusters, it is possible to infer the mass of galaxies that lie along the line of sight between the source galaxy and the observer. The total mass of galaxy clusters inferred from their lensing arcs is several times larger than the mass of the stellar and gaseous matter. (Taylor et al., 1998).

Simulations of universes dominated by cold dark matter allow for precise predictions of the spatial distribution of galaxies in the observable Universe. The predicted distribution of galaxies (Springel et al., 2005) agrees strikingly well with the distribution of galaxies observed in the real Universe (Rodríguez-Torres et al., 2016).

1.1.2 The evidence for dark energy

Cosmic inflation theory (Starobinsky, 1980; Guth, 1981; Linde, 1982) predicts that the Universe has a flat geometry, yet the combined mass of dark and baryonic matter can only account for around one third of the required energy density. The measured brightness of Type Ia supernovae at different redshifts (Riess et al., 1998; Perlmutter et al., 1999) implies that the expansion rate of the Universe is accelerating. The missing energy density and mysterious acceleration could be simultaneously explained if the vacuum itself possessed an inherent energy density. In the standard cosmological model, this vacuum energy density is described as a cosmological constant.

1.2 Small scale challenges to the ΛCDM paradigm

As the accuracy and resolution of numerical simulations has increased, a number of tensions have arisen between predictions of the distribution of dark matter in dark matter-only (DMO) simulations, and the distribution of dark matter inferred from observations. These discrepancies, collectively known as the small scale problems of CDM (or more sensationally as the small-scale crisis of CDM), are often attributed either to the inability of DMO simulations to model baryonic physics, uncertainties and assumptions in the modelling used to infer the distribution of dark matter from observations, or the misapplication of statistics. Below, we introduce and discuss each of the small scale problems and their proposed solutions.

1.2.1 The missing satellites problem

By 1999, astronomers had identified 11 satellite galaxies of the Milky Way (the so-called “classical” satellites). Simulations of galactic halos predicted around 500 subhalos with circular velocities larger than the Draco system. The discrepancy

between these two numbers was first highlighted by Moore et al. (1999) and Klypin et al. (1999), and has come to be known as the missing satellites problem. Moore et al. (1999) also argued that a large abundance of substructure in galactic halos would prevent the formation of spiral disk galaxies due to the shocks in the gravitational potential caused by clumpy collapse.

The missing satellites problem may be alleviated if galaxy formation is inefficient in halos below a certain mass. If the potential well of a halo is not sufficiently deep, then processes such as reionisation[1] and supernova feedback heat up and expel gas from the halo. Consequently, most of the satellites in the Milky Way have very high mass-to-light ratios, or may even be devoid of baryonic matter (Bullock et al., 2000; Benson et al., 2002; Somerville, 2002; Okamoto et al., 2008; Macciò et al., 2010). This idea has since been confirmed using hydrodynamical simulations of galaxy formation (Sawala et al., 2016; Wetzel et al., 2016). It is also worth noting that the number of detected satellites in the Milky Way currently stands at 56 with only half the night sky having been surveyed by the deepest observing telescopes. Estimates for full-sky coverage expect to find roughly 120 satellites brighter than $M_V = 0$ within 300 kpc of the Sun (Newton et al., 2018).

1.2.2 The "too big to fail" problem

The too big to fail (TBTF) problem is a refinement of the missing satellites problem. A potential route to alleviate the missing satellites problem is to note that we only observe gas and stars, and so we will fail to observe many of the subhalos present in our galaxy if they have been stripped of their baryonic material by interactions with the host galaxy. Boylan-Kolchin et al. (2011) refined this idea by comparing kinematic measurements of the masses of Milky Way satellites with high-resolution simulations of Galactic halos. They found that a Milky Way-mass halo should typically contain at least six subhalos with a maximum circular velocity at infall of

[1]Reionisation refers to the epoch in cosmic history when radiation from the first stars ionised neutral hydrogen.

at least 30 km/s. This predicted population of subhalos have central densities which are too great to be compatible with the measured density profiles of the classical Milky Way satellites.

As with the missing satellites problem, a promising solution to the TBTF problem lies in the inability of DMO simulations to model baryonic effects. Reionisation and supernova feedback expel gas from small halos at high redshift. This process cannot be accounted for in a DMO simulation. A DMO halo will be approximately 15% more massive than its hydrodynamical counterpart, due to its inability to lose its baryonic matter. As more massive halos tend to grow faster, this discrepancy in the masses of the hydrodynamical and DMO realisations of a halo only grows over time. At the present day, this effect equates to a 15% reduction in $V_{\rm max}$ (or around 25% in total mass) for simulated subhalos (Sawala et al., 2013; Schaller et al., 2015). Hydrodynamical simulations, which can account for this early mass loss, do not suffer from the TBTF problem (Sawala et al., 2016; Wetzel et al., 2016).

1.2.3 The cusp-core problem

One of the key predictions of the ΛCDM model is the universality of the NFW density profile (Navarro et al., 1996). The NFW density profile describes the density of dark matter in halos and subhalos as a function of radius. The density profile can be expressed as

$$\rho_{\rm NFW}(r) = \frac{\rho_s}{(r/r_s)(1+r/r_s)^2} \ . \tag{1.2.1}$$

The NFW profile is a broken power law, with an inner slope of -1, and an outer slope of -3. The location of the transition between the inner and outer slopes is given by the scale radius, r_s, and the amplitude of the density profile is fixed by the scaled density, ρ_s, which is 4 times the density of dark matter at r_s.

However, observational data suggest that halos and subhalos may have constant density cores, i.e. the slope of the density profile tends toward 0 for decreasing radius, inside some radius. Claims for the existence of cored density profiles typically

focus on dwarf spheroidal galaxies and low surface brightness (LSB) galaxies (Moore, 1994; Flores & Primack, 1994; Burkert, 1995; Walker & Peñarrubia, 2011; Agnello & Evans, 2012; Oh et al., 2015), using some analytic model to infer the properties of the dark matter from kinematics of stars and gas.

Whether or not observations of dwarf galaxies imply the existence of a cored dark matter density profile remains an unsolved problem (Strigari et al., 2010; Adams et al., 2014; Oh et al., 2015; Oman et al., 2019). Much of the modelling of stellar kinematics in dwarf galaxies relies on the assumption of spherical symmetry. For example, Walker & Peñarrubia (2011) reported finding cores in Sculptor and Fornax, using the mass estimator method of Wolf et al. (2010). However, when the asymmetry of the stellar populations was taken into account, Genina et al. (2018) found that observations are consistent with both cuspy and cored density profiles .

Cored density profiles are produced in some hydrodynamical simulations, but not others. The uncertainties in the modelling of baryonic processes are large enough that it is impossible to say whether observations of cored density profiles in the real universe would present a challenge to the CDM model. For example, repeated bursts of star formation can produce cores at the centre of dwarf galaxies (Pontzen & Governato, 2012; Brooks & Zolotov, 2014). However, the ability of these processes to drive core formation depends strongly on the choice of numerical parameters, particularly the density threshold at which cold gas begins to form stars (Benitez-Llambay et al., 2018). Such parameters are not physical, and so cannot be constrained by observation.

1.2.4 The planes of satellites problem

The 11 classical satellites of the Milky Way lie in the plane of a thin disc, with most of satellites sharing a common rotational direction (Lynden-Bell, 1976). A similarly anisotropic distribution of satellites is seen in the Andromeda system (McConnachie et al., 2009). Ibata et al. (2015) calculated the probability of observing such a configuration is less than 0.1% in ΛCDM.

Such claims of extremely high detection significance levels for the planes of satellites in the Milky Way and Andromeda fail to account for the *look-elsewhere* effect. This accounts for the probability of finding seemingly highly significant fluctuations by chance when searching an extremely large parameter space. When searching for planes of satellites, there is no a priori definition of the number of satellites necessary to define a plane, or how precisely the satellites should lie in the plane. The detection significance of a particular configuration of satellites should be measured by fraction of satellite systems drawn from an sample distribution which have a more prominent plane. When accounting for this effect, and comparing observations to high resolution numerical simulations, Cautun et al. (2015) find that around 10% of CDM halos have more prominent planes of satellites than Andromeda. They also show that the failure to account for the look-elsewhere effect resulted in Ibata et al. (2015) overestimating the significance of the LG satellite planes by two orders of magnitude.

1.3 Alternative cosmological models

In addition to the standard ΛCDM cosmology, there exist a wide variety of alternative cosmological models. The CDM model treats dark matter particles as collisionless, and with primordial thermal velocities which are negligible compared to the velocities induced by gravitational instabilities. Each of these assumptions may be tested by considering scenarios where the dark matter differs in at least one of these properties. Alternative models of dark matter also merit investigation for the simple fact that no experiment has detected the dark matter particle so far (if it is indeed a particle at all). Probing the viability of alternative cosmological models also provides justification to build detection experiments that probe parameter spaces beyond the WIMPs assumed in the standard model of cosmology.

1.3.1 Warm dark matter

Warm dark matter (WDM) cosmologies describe a universe where the primordial velocities of dark matter particles were large enough to reduce the abundance of structure on the scale of dwarf galaxies relative to CDM at the present day. The effect of greater thermal velocities at high redshifts is to suppress the formation of structure through a process known as *free-streaming*, where the random thermal motion of particles tends to erase structures forming due to gravitational collapse. More precisely, free-streaming prevents the formation of structure below some characteristic mass scale, resulting in the absence of low-mass halos and subhalos at the present day. Structures in WDM cosmologies also form later, and so are less concentrated than halos in the CDM model (Hellwing et al., 2016; Bose et al., 2017). Early cosmological models considered massive neutrinos with a mass of 30 eV as a candidate for dark matter. These models were motivated by claims to have measured the mass of the neutrino to be around 30 eV (Lubimov et al., 1980)[2], a value which would account for all the Universe's missing mass. The characteristic free-streaming mass scale for such a particle is around 10^{15} $M_{\odot}$, meaning that these models were quickly ruled out (Schramm & Steigman, 1981).

A particularly interesting WDM candidate is motivated by the observations of a 3.5 keV emission line in the X-ray spectra of galaxies and clusters (Bulbul et al., 2014; Boyarsky et al., 2014). Whilst the nature of the origin of this line is disputed (Malyshev et al., 2014; Anderson et al., 2015; Jeltema & Profumo, 2015; Franse et al., 2016; Riemer-Sørensen, 2016), if its origin is not explicable within the standard model of particle physics, it could be the result of the decay of 7 keV sterile neutrino dark matter (Dodelson & Widrow, 1994). Sterile neutrino dark matter is an attractive proposition, as it has the potential to simultaneously resolve multiple outstanding problems in cosmology and neutrino physics, including the origin of the observed matter-antimatter asymmetry (Asaka & Shaposhnikov, 2005) and neutrino

[2]These claims were later shown to be incorrect

flavour oscillations.

1.3.2 Interacting dark matter

Another common alternative to the CDM model is to consider forms of dark matter which interact weakly with standard model particles (typically photons or neutrinos) at early times. The coupling of relativistic standard model particles to the dark matter causes the dark matter to free stream when the low-velocity dark matter particles in overdense regions interact with relativistic particles (a process known as collisional damping), with a characteristic scale below which structure formation is suppressed (Boehm & Schaeffer, 2005; Bœhm et al., 2014). Once these early time interactions have taken place, (usually before matter-radiation equality), structure formation proceeds in a similar fashion to WDM cosmologies (Schewtschenko et al., 2015). The matter power spectrum in interacting dark matter cosmologies is distinct from the power spectrum in WDM cosmologies, as the dark matter-photon interactions produce characteristic oscillations on the scale of dwarf galaxies, in a manner analogous to the baryon-acoustic oscillations produced by the baryon-photon fluid in the early Universe.

1.3.3 Self-interacting dark matter

Most particles in the standard model of particle physics experience significant self interactions, and there is no reason a priori why this should not be true of the dark matter particle. If the ratio of the interaction cross section to the particle's mass is $\mathcal{O}(1\ \mathrm{cm}^2\ \mathrm{g}^{-1})$, the results of the self-interactions are astrophysically interesting (Spergel & Steinhardt, 2000; Yoshida et al., 2000). Dark matter particles on eccentric orbits can transfer energy to tightly bound particles at the centre of the halo. The result of this effect is to form isothermal cores at the centre of dark matter halos (Burkert, 2000), rather than the cuspy profiles seen in collisionless CDM simulations (Navarro et al., 1996).

1.3.4 Primordial black holes

The failure of experiments to detect dark matter in the form of WIMPs has caused physicists to consider the possibility that dark matter may not even be a particle at all. Scenarios where the dark matter consists of primordial black holes, with masses in the range 10^1–10^3 $M_\odot$, can explain the observed abundance of dark matter whilst evading constraints from lensing and large scale structure (Carr et al., 2016). The potential significance of such models has increased in recent years following the detection of black hole mergers in this mass range by the LIGO project (Abbott et al., 2016).

1.3.5 Fuzzy dark matter

Another radically different form of dark matter, proposed in the absence of the detection of WIMPs, is ultra-light (10^{-22} eV) bosons, which behave as a Bose-Einstein condensate (Hu et al., 2000). Such candidates are well-motivated from a particle physics perspective, as this particle could be an axion, a particle which also simultaneously solves the strong CP problem of quantum chromodynamics (Duffy & van Bibber, 2009). Axion-like particles also occur naturally in string theory, and could just as well comprise the dark matter (Arias et al., 2012). Ultra-light boson dark matter with a de Broglie wavelength on the scale of dwarf galaxies has many testable astrophysical features, including:

- A complete absence of halos below 10^7 $M_\odot$.
- A reduced abundance of 10^7–10^{10} $M_\odot$ halos relative to CDM.
- Halos with central density cores.
- A minimum mass of around 10^8 $M_\odot$ for subhalos near the centre of the Milky Way .
- A delayed onset of galaxy formation relative to CDM.

- The potential formation of dark matter disks (Hui et al., 2017).

1.4 Small scale tests of the ΛCDM model

1.4.1 The disruption of stellar streams

The abundance of dark substructure inside the Milky Way can be probed by studying stellar streams. Stellar streams, which form due to the tidal disruption of globular clusters or dwarf galaxies, can be measurably perturbed by passing substructures which produce gaps in the streams (Carlberg et al., 2012). Surveys such as Gaia (Perryman et al., 2001; Gilmore et al., 2012), DES (The Dark Energy Survey Collaboration, 2005), and LSST (LSST Science Collaboration et al., 2009) have the potential to measure these gaps and thereby determine the mass function of substructures in the Milky Way down to a scale of 10^7 $M_\odot$ (Erkal & Belokurov, 2015b,a). Individual gaps, for example in the GD-1 stellar stream may be studied to characterise peturbers on a case-by-case basis (Bonaca et al., 2019). Alternatively, the number and properties of gaps may be studied on a statistical basis, for example by predicting the observed number of gaps in streams for a given subhalo mass function. Such methods were explored in Erkal et al. (2016); however, their results are limited by their failure to include the effect of a galactic disk, which significantly alters the abundance and orbital distributions of subhalos relative to the DMO simulations used in their study. Furthermore, Erkal et al. (2016) found it necessary to assume a particular subhalo velocity distribution in order to break the degeneracy between the peturber's mass and its velocity.

1.4.2 Perturbations in the giant arcs of strongly lensed galaxies

Light from a distant galaxy can be distorted by mass along the line of sight between the source galaxy and the observer. In the most extreme examples, a massive galaxy

can act as a lens which bends the light from the source galaxy into a ring, known as an Einstein ring. Koopmans (2005) showed that substructure within the lensing halo can perturb the Einstein ring, and that these perturbations can be used to probe the subhalo mass function and therefore constrain cosmological models (Li et al., 2016; Despali & Vegetti, 2017). This method has already yielded detection of a $1.9 \pm 0.1 \times 10^8$ $M_\odot$ dark satellite and, with imaging data of good quality, the detection sensitivity could reach 2×10^7 $M_\odot$The definition of mass here is based on a pseudo-Jaffe model and differs from the standard definition of halo and subhalo masses used in cosmological simulations and in this thesis.(Vegetti et al., 2012).
It has subsequently been shown that, in a CDM universe, the dominant contribution to the lensing signal originates not from substructure in the lensing halo, but from field halos between the source galaxy and the observer (Li et al., 2017; Despali et al., 2018). The abundance of such halos in hydrodynamical cosmological simulations does not depend sensitively on the exact implementation of baryonic physics. Therefore, tests of cosmological models based on the abundance of field halos are quite simple compared with tests which probe the abundance of substructure within halos.

1.5 Cosmological simulations

The formation of cosmic structure is a highly non-linear process. Analytic models provide a helpful theoretical insight into the processes involved, but the nature of the problem means they are often incapable of making the kind of precise theoretical predictions necessary to test the model against observations. Numerical simulations are required to track the formation and evolution of cosmic structure in the non-linear regime.
Cosmological simulations follow the evolution of matter in the Universe through time. The earliest cosmological simulations only considered the gravitational interaction between matter, as this is the only force relevant to structure formation on large distance scales. Matter in these simulations is treated as collisionless, with no

modelling of baryonic physics. They are usually referred to as N-body or DMO simulations.

1.5.1 Initial conditions

Cosmological simulations do not trace the evolution of matter from the Big Bang, but from a time which is sufficiently close to the Big Bang for the evolution of matter up to that point to be described by solvable, linear equations. The simplest method for generating a set of initial conditions is to generate a uniform grid of particles, and then perturb the positions and velocities of each particle. Positions and velocities are assigned to particles based on an input linear power spectrum using some approximate method, e.g the Zel'dovich method (Zel'dovich, 1970) or second order Lagrangian perturbation theory (Buchert, 1994).

It is prohibitively computationally expensive to simulate large regions of the Universe at very high resolution. A common workaround to this issue is to resimulate small patches from a large volume at a higher level of resolution. The large scale tidal fields of the parent simulation are reproduced in the resimulation using a small number of high-mass particles, almost all computational resources are dedicated to simulating the region of interest, often a single halo, at much higher resolution. These kinds of (re)simulation are referred to as zoom-in simulations, or simply zoom simulations. Typically, around 99% of all simulation particles are confined to less than 1% of the total simulation volume.

1.5.2 Halo identification

Analysis of cosmic structure in simulations relies on identifying halos from the raw simulation particle data. All simulations discussed in this thesis use the friends-of-friends (FOF) method (Davis et al., 1985) to identify the tightly-bound groups of dark matter particles which correspond to the halos which envelop galaxies in our Universe. Each FOF group is found by identifying the set of all particles separated by

a maximum distance, known as the linking length. The linking length is a free parameter, and is typically taken to be 20% of the mean inter-particle separation, which is given by the cube root of the simulation averaged number density of particles.

Once FOF groups have been identified, substructure inside halos can also be identified and characterised. Whilst there are several commonly-chosen methods for identifying substructure in simulations[3], all simulations in this thesis are analysed using the SUBFIND algorithm (Springel et al., 2001), which identifies locally overdense regions within a FOF group by calculating the smoothed density at the position of each particle, and selecting sets of particles enclosed by isodensity contours which traverse saddle points in the density field. This is followed by an unbinding procedure which removes particles whose kinetic energies are greater than the magnitude of their potential energies from the list of subhalo particles.

Once halos have been identified at each simulation snapshot, the merging and accretion histories of halos are encapsulated in a structure known as a merger tree (Lacey & Cole, 1993). Merger trees allow for the identification of progenitor halos at earlier snapshots, by following the "main branch" of the tree. Merger trees also describe the process by which smaller field halos are accreted onto larger halos. Simulations in this thesis use the DHALO algorithm (Jiang et al., 2014) to track the merging of subhalos.

1.5.3 Semi-analytic models

To test cosmological models against observations, DMO simulations alone are insufficient. Until recently, the best available method was to take a population of halos from a DMO simulation, and use simple, physically motivated models to populate these with galaxies in a way that depends on the properties and assembly history of the halo. These semi-analytic models are well-motivated and computationally inexpensive, but are unable to predict the effects of baryonic physics on the properties

[3]See Onions et al. (2013) for a detailed list and comparison.

of the dark matter halo.

1.5.4 Hydrodynamical simulations

Hydrodynamical simulations of cosmological structure formation consider the co-evolution of both the dark and baryonic matter. These simulations are much more computationally expensive than DMO simulations, but they are able to track not only the formation of galaxies, but also the interactions between dark matter and baryonic matter. Hydrodynamical simulations can resolve some important physical processes, such as radiative cooling and the mixing of cold and hot gas in halos, however they also require subgrid models to implement physical effects which occur on scales below the resolution limit, such as star formation.
Recent advancements in computing power, efficient algorithms and better physical models have seen numerous simulations reproduce a wide range of observed properties of galaxies (Schaye et al., 2015; Vogelsberger et al., 2014; Hopkins et al., 2014). Below we describe the simulation codes and suites of simulations used in this thesis. A brief summary of key simulation properties is given in Table 1.1.

Eagle

The EAGLE project (Schaye et al., 2015; Crain et al., 2015) comprises a set of cosmological hydrodynamical simulations, performed with a heavily-modified version of the smoothed particle hydrodynamics (SPH) code GADGET3 (Springel et al., 2005). The EAGLE code contains subgrid physics implementations for a wide range of processes important for galaxy formation. These include:

- An equation of state for the interstellar medium
- Star formation
- Stellar evolution and enrichment

- Stellar feedback

- Supermassive black holes

The EAGLE subgrid model has many free parameters which must be calibrated against observables. The observables used for calibration are the redshift $z = 0.1$ galaxy stellar mass function, the galaxy mass-size relation, and the relation between the stellar mass of a galaxy and the mass of its supermassive black hole. The EAGLE REFERENCE model is the EAGLE code with the set of subgrid parameters chosen to reproduce this set of observables.

Apostle

The APOSTLE simulations (Sawala et al., 2016; Fattahi et al., 2016) are a set of zoom simulations of Local Group-like volumes which use the EAGLE REFERENCE model. Each volume contains a pair of $\sim 10^{12}$ $M_\odot$ halos, similar to Andromeda and the Milky Way, as well as a considerable region of field volume. Each high resolution region is approximately spherical, with a radius of 2.5 Mpc centred on the Local Group barycentre. The total mass of each pair of halos is selected to lie in the range 1.6–3.6$\times 10^{12}$ $M_\odot$, with each halo having a mass between 5×10^{11} $M_\odot$ and 2.5×10^{12} $M_\odot$. The separation of each pair of halos is between 600 and 1000 kpc, and the halos are currently moving towards each other with a relative radial velocity between 0 and 250 km/s and a relative tangential velocity of less than 100 km/s. Furthermore, the high-resolution volume is required to contain no other halos more massive than the smaller of the two main halos.

There are 12 APOSTLE volumes simulated at “intermediate" resolution, with a typical dark matter particle mass of approximately 6×10^5 $M_\odot$. There are also five APOSTLE volumes simulated with an order of magnitude better mass resolution.

Auriga

The Auriga simulations (Grand et al., 2016) are a set of zoom simulations of Milky Way-mass halos, performed with the Arepo code (Springel, 2011; Grand et al., 2016) used for the Illustris simulation (Vogelsberger et al., 2014). Much like the Eagle simulations, the Illustris simulations use a complicated subgrid model to model processes below the resolution limit of the simulation. The parameters of the subgrid model in Illustris are calibrated somewhat differently to the Eagle simulations. In Illustris they are tuned to match the $z = 0$ ratio of galaxy stellar to dark matter mass and the cosmic star formation rate across all redshifts. The Arepo code is a magnetohydrodynamics code, and so the Auriga simulations also include the some of the effects of magnetic fields on galaxy formation (Pakmor et al., 2017).

There are 30 Auriga halos simulated at intermediate (level 4) resolution. Each of these halos was selected to have a mass of 1–2$\times10^{12}$ $M_\odot$, and also to have no nearby halos with masses greater than 3% of the target halo's mass. The dark matter particle mass of the level 4 Auriga halos is around 3×10^5 $M_\odot$. There are also 6 level 3 Auriga halos, which have a typical dark matter particle mass of 3×10^4 $M_\odot$.

The parameters of the subgrid models in Eagle and Illustris are calibrated somewhat differently. In Eagle, they are chosen so as to reproduce the $z = 0$ galaxy stellar mass function and size distribution, while in Illustris they are tuned to match the $z = 0$ ratio of galaxy stellar to dark matter mass and the cosmic star formation rate at all times. The main halos in the Apostle and Auriga simulations have broadly similar masses, $\sim 10^{12}$ $M_\odot$; however, the stellar masses of the central galaxies in Auriga are significantly larger, typically around twice as massive as an Apostle galaxy. The Auriga galaxies are also more concentrated than the Apostle galaxies; despite being twice as massive, their half-stellar-mass

radii are similar or smaller than those of APOSTLE galaxies.

New simulations

In Chapter 3 we introduce a new simulation; a zoom simulation of a 10^{13} $M_\odot$ halo and its local environment, run using the EAGLE REFERENCE model. The precise details of the simulation, including candidate selection and construction of the initial conditions are described in full in the first part of that Chapter.

1.6 The structure of this thesis

In this thesis we use cosmological simulations to examine the effects of baryonic physics on the abundance and properties of dark matter halos and subhalos. In Chapter 2 we study how changing the implementation of baryonic physics affects halo substructure using two state-of-the-art simulations of Milky Way-mass halos, APOSTLE and AURIGA. We also show that some results of previous studies of subhalo abundance were incorrect due to the way in which the authors reconstructed the orbits of subhalos between simulation snapshots. We describe a method of integrating subhalo orbits between snapshots which does not suffer the radial bias associated with the other methods.

In Chapter 3 we introduce a new simulation of 10^{13} $M_\odot$ halo, performed using the EAGLE code. This simulation uses a new type of initial conditions, where dark matter particles outnumber gas particles by a ratio of 7:1. We describe the generation of these initial conditions, and the tests we performed to ensure that we did not introduce any numerical effects into the final simulation. We use this new simulation to study the abundance and properties of 10^7–10^{10} $M_\odot$ field halos, and the effects of environment on halo properties.

In Chapter 4 we describe basic properties of the main halo in the simulation introduced in the previous chapter. We use the simulation to study the effect of baryonic physics on the abundance of substructure in the main halo . We also study how

Simulation	Halo Mass [$M_\odot$]	Galaxy Mass [$M_\odot$]	$m_{\rm DM}$ [$M_\odot$]	Cosmology	Galaxy formation model	Number of halos
Apostle	10^{12}	2×10^{10}	4×10^4	WMAP 7	Eagle Reference	8
Auriga	10^{12}	1×10^{11}	4×10^4	Planck 2015	Illustris	6
New zoom	10^{13}	1×10^{11}	8×10^4	Planck 2015	Eagle Reference	1

Table 1.1: Basic properties of the simulations used in this thesis. For Apostle and Auriga the values provided are typical for halos at the highest resolution level in each simulation suite. The halo mass is the total mass of all types of matter in the halo. The galaxy mass is the total mass of all gas and star particles within 30 kpc from the centre of the halo. Halo and galaxy masses given are for redshift $z = 0$. $m_{\rm DM}$ is the mass of the high-resolution dark matter particle used in the hydrodynamical version of the simulation. The number of halos refers to the number of "main" halos in each simulation suite, as opposed to smaller field halos contained in the simulation volumes.

subhalo properties reported by the SUBFIND algorithm depend on various properties of the subhalo and the host halo.

In Chapter 5 we summarise the results of each chapter and we discuss the limitations of this thesis. We conclude by considering the role of cosmological simulations in attempts to discover the nature of dark matter.

Chapter 2

Comparing substructure in the Apostle and Auriga simulations

2.1 Introduction

KEY PREDICTION that distinguishes CDM from some of the alternatives, such as WDM, is the abundance of small-mass halos and subhalos. In CDM, the halo mass function continues to rise to small masses (Diemand et al., 2007; Springel et al., 2008), whereas in WDM, the halo mass function is truncated at a mass on the scale corresponding to dwarf galaxies (Colín et al., 2000; Lovell et al., 2012; Schneider et al., 2012; Hellwing et al., 2016; Bose et al., 2017). In sterile neutrino WDM models, the power spectrum of primordial fluctuations depends not only on the dark matter particle mass but also on an additional lepton asymmetry parameter. In the coldest sterile neutrino model compatible with the 3.5 keV line originating from particle decay, the mass function is suppressed by a factor of 5 relative to CDM at 10^8 $M_\odot$ and is negligible at 10^7 $M_\odot$ (Bose et al., 2017). Thus, detection of halos of mass below 10^7 $M_\odot$ would rule out this candidate particle and set a lower limit larger than 7 keV for the sterile neutrino mass. Conversely, a convincing non-detection of halos of mass below $\sim 10^8$ $M_\odot$ would rule out CDM (Li et al., 2016).

If they exist, the vast majority of these small-mass halos will be dark, that is, almost completely devoid of baryonic matter. This baryon deficit is the result of reionisation and supernova heating (Okamoto et al., 2008; Sawala et al., 2016). These dark objects can be detected through their gravitational interaction with visible matter. Of particular interest is the perturbation of strong lenses by galactic substructure, detailed in §1.4. Although for practical lensing configurations the lensing signal is dominated by field halos rather than subhalos (Li et al., 2017; Despali et al., 2018), the latter make a non-negligible contribution to the lensing distortion. Since dark subhalos in this low-mass range are uncontaminated by baryonic matter at the present day, the only uncertainty in their abundance arises from possible interactions

between subhalos and the central galaxy in their common host halo, for example tidal disruption. Quantifying these effects is necessary to make accurate predictions for the expected lensing signals.

The role of the central galaxy in the destruction of substructure has been studied using N-body simulations that incorporate an analytic disk potential (D'Onghia et al., 2010; Yurin & Springel, 2015), as well as hydrodynamical simulations (Garrison-Kimmel et al., 2017; Sawala et al., 2017). The specific implementation of baryonic physics is important: the choice of subgrid model, physical parameters and method for solving the hydrodynamical equations all individually can affect the abundance of substructure. Errani et al. (2017) also showed that the inner slope of the density profile of infalling substructures affects their survival probability. Benitez-Llambay et al. (2018) showed that the central density of dwarf galaxies depends strongly on the choice of the star formation gas density threshold, with CDM cosmological simulations producing cuspy or cored profiles depending on the choice of this parameter. The effect of changing the subgrid galaxy formation models on subhalo abundance has been investigated by Despali & Vegetti (2017) in the case of the EAGLE and ILLUSTRIS 100^3 Mpc^3 simulations (Schaye et al., 2015; Vogelsberger et al., 2014). Both simulations have relatively poor mass resolution (approximately 10^7 $\mathrm{M}_\odot$) so this study was restricted to massive substructures rather than the small ones that are important for distinguishing CDM from WDM. Furthermore, these simulations have a relatively small number of outputs so the orbits of subhalos cannot be tracked and, as a result, the destruction of subhalos in the innermost regions of galaxies, where processes such as disk shocking are important, is poorly sampled.

With mass resolution of approximately 10^4 $\mathrm{M}_\odot$, the simulations that we analyze in this chapter have at least 100 times better resolution than the simulations studied by (Despali & Vegetti, 2017). In particular, they resolve the small-mass halos (with masses $\sim 10^7$ $\mathrm{M}_\odot$)required to distinguish CDM from WDM. To investigate the dependence of the surviving subhalo abundance on the choice of baryonic physics implementation, we compare the APOSTLE (Sawala et al., 2016; Fattahi et al.,

2016) and Auriga (Grand et al., 2016) CDM simulations. We integrate the orbits of subhalos between snapshots to obtain precise estimates of time-averaged subhalo abundance close to the centre of the halo. This is the first direct comparison of baryonic physics models at such a high level of resolution, both spatially and temporally.

2.2 The orbits of subhalos

The time between snapshots in the simulations (around 300 Myr for Apostle and the hydrodynamical version of Auriga) is greater than the crossing time for the central 20-30 kpc of the main halo. These snapshots are sufficiently infrequent that the subhalo abundance in the central 20 kpc of the halo is poorly sampled. To make precise theoretical predictions for the abundance of substructure near the centre of halos and to quantify the impact of the galactic disk, previous studies inferred the positions of subhalos between snapshots using a cubic spline to interpolate between snapshots (Sawala et al., 2017; Garrison-Kimmel et al., 2017).

2.2.1 We need to talk about the cubic spline

Both Sawala et al. (2017) and Garrison-Kimmel et al. (2017) use a cubic spline to infer the positions of subhalos between simulation snapshots. Specifically, a cubic piecewise polynomial was fit to each Cartesian coordinate of the physical positions of subhalos at the snapshots as a function of time with the condition that the result be twice continuously differentiable, except at the ends, where the first derivative is equal to the linear interpolant slope.

To demonstrate the inaccuracies introduced by cubic spline interpolation, we use the Aquarius simulations. The Aquarius project is a set of DMO zoom-in simulations of 10^{12} $M_\odot$ dark matter halos (Springel et al., 2008). Specifically, we use the Aq-A4 simulation, which has 258 snapshots between $z = 0.5$ and the present day, and a high-

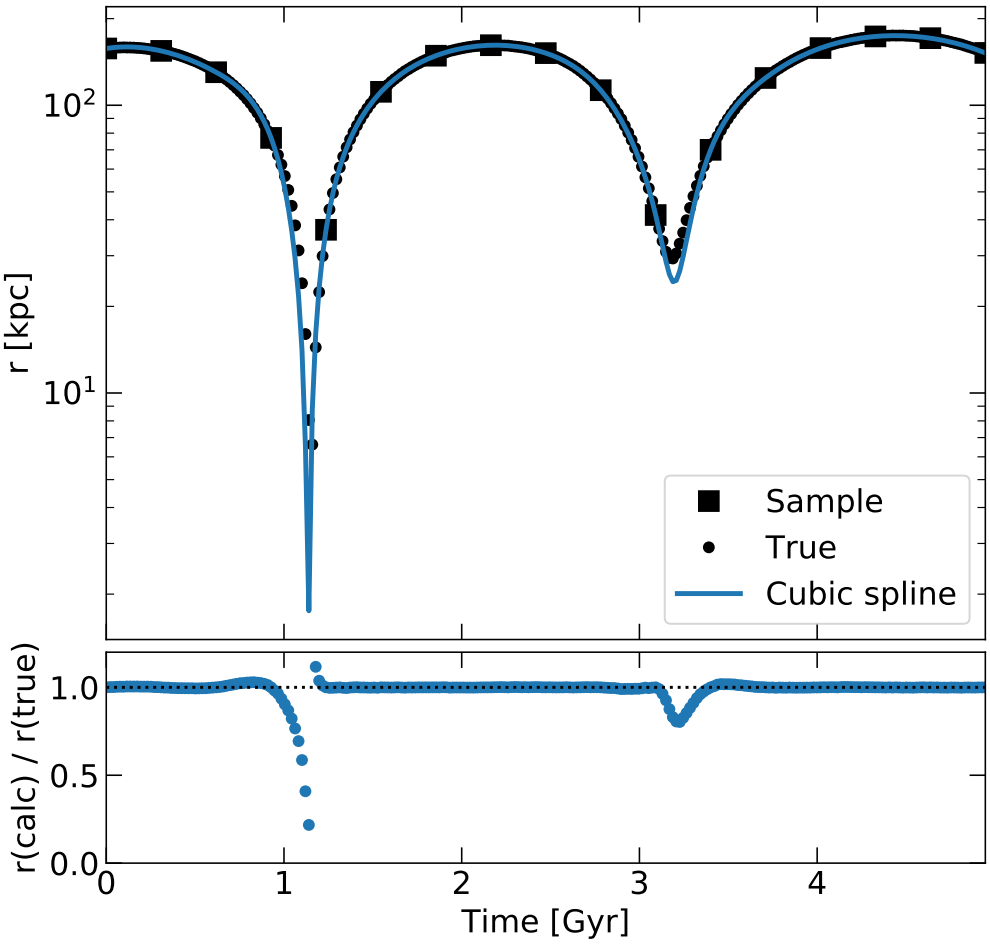

Figure 2.1: The distance of a subhalo from the halo centre of potential over several orbital periods in the Aquarius Aq-A4 simulation. Black circles show the distance measured at each snapshot. Black squares show the distance at snapshots used for orbit integration and fitting cubic splines. The blue line shows the orbit inferred from the cubic spline method used in Sawala et al. (2017). The bottom panel shows the ratio of the inferred distance from the centre of the halo to the distance measured at each snapshot. Major deviations are observed at pericentre, when the constant acceleration assumption of the cubic spline method breaks down.

resolution particle mass of 3.9×10^5 $M_\odot$. This time resolution is approximately sixteen times better than in the APOSTLE simulations. We select a subset of snapshots with the same temporal spacing as the snapshots in the APOSTLE simulations. We can compare the orbits calculated using the cubic spline interpolation on the subset of snapshots to the orbit measured in the additional snapshots not used to fit the cubic splines. Fig. 2.1 demonstrates how the cubic spline interpolation underestimates the orbital radius of a subhalo near pericentre. This underestimation occurs at pericentre as this is where the acceleration experienced by the subhalo is varying most rapidly. The cubic spline, which assumes that the acceleration of the subhalo is linear in time between snapshots, is unable to account for the rapidly varying force acting on the subhalo as its distance from the centre of the halo changes rapidly. In Fig. 2.2 we show a two-dimensional projection of the orbit over a period of 1 Gyr, specifically between the the times 1.5 <t/Gyr< 2.5 shown in Fig. 2.1. The positions plotted for the cubic spline are calculated at the exact time of the AQUARIUS snapshots, so any deviations are due solely to the choice of interpolation.

To quantify the error introduced by the cubic spline interpolation on the calculation of the subhalo radial distribution, we calculate the time-averaged cumulative radial distribution of subhalos over a 5 Gyr period using the positions in the AQUARIUS snapshots and the positions calculated using cubic spline interpolation. We create our sample of subhalos by selecting all subhalos which exist at every snapshot between redshift $z = 0.5$ and the present day. This is to avoid confusion in our results due to the fallibility of the SUBFIND algorithm in high-density regions, or from the destruction of a subhalo halfway between two sample snapshots. Fig. 2.3 shows that the tendency of the cubic spline to underestimate the orbital radius of a subhalo leads to a large overprediction of the abundance of subhalos at radii less than 20 kpc (around 10% of r_{200}). At distances of less than 5 kpc from the halo centre, the cubic spline interpolation method predicts a significant chance of observing substructure despite no object having ever passed so close to the halo centre.

We also calculate the effect of using a cubic spline to measure the velocity distribution

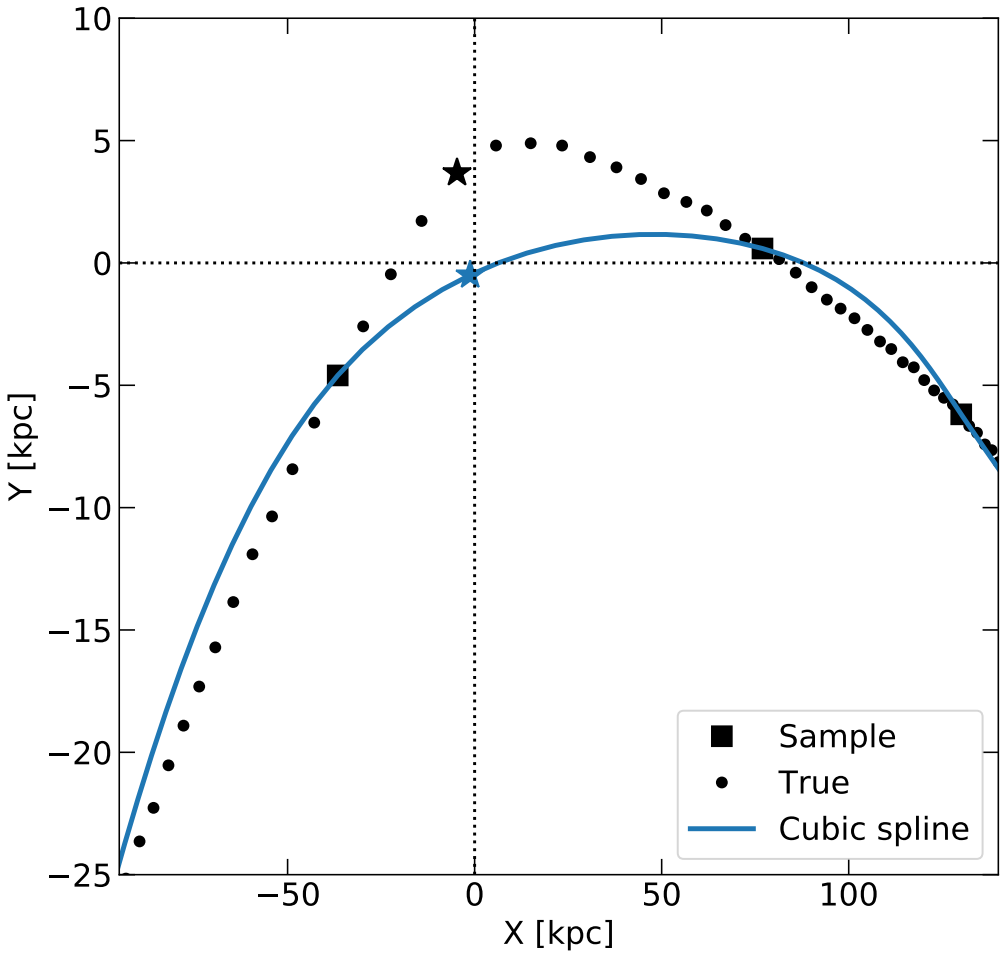

Figure 2.2: A two-dimensional projection of a portion of the subhalo orbit shown in Fig. 2.1. The orbit is close to planar in the z coordinate. The portion of the orbit is chosen from the middle of the whole orbit shown in Fig. 2.1 to prevent edge effects in the cubic spline interpolation. Black circles show the position of the subhalo at each snapshot, and black squares the position of the subhalo at the snapshots used in the cubic spline reconstruction of the orbit (blue line). Stars show the position of the pericentre of the orbit.

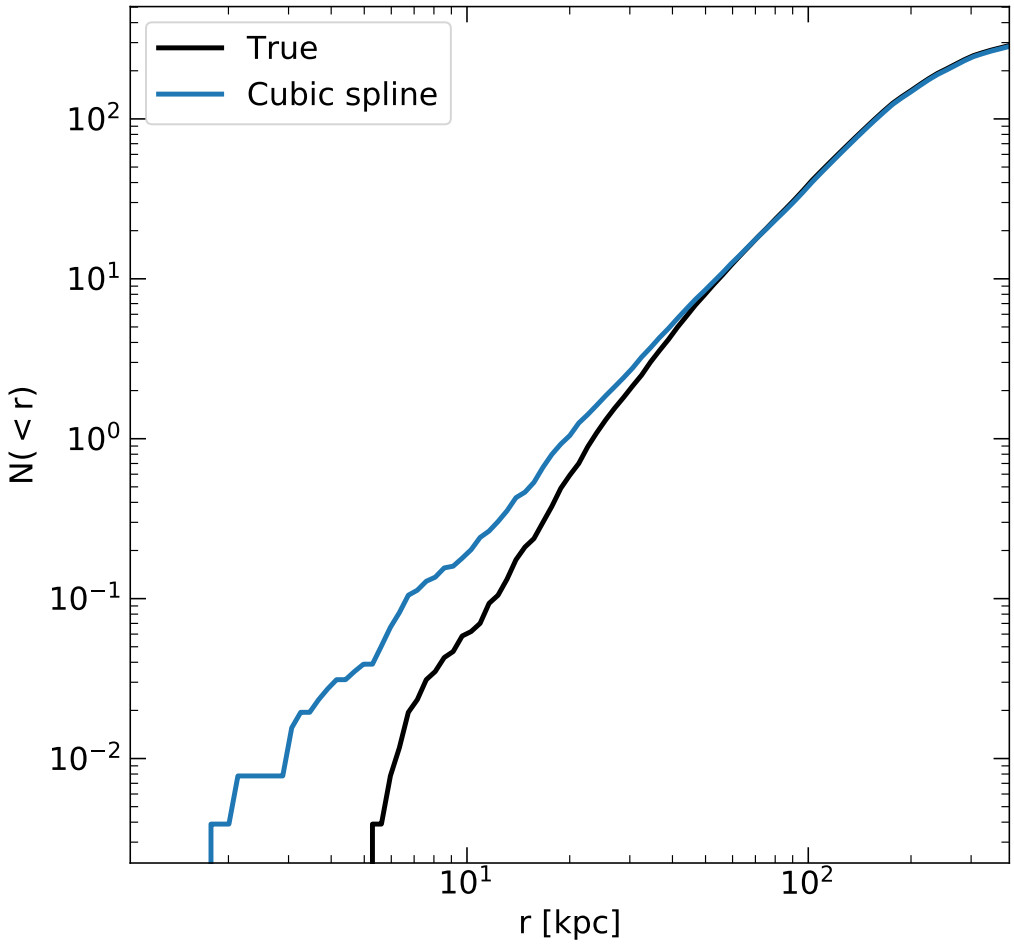

Figure 2.3: Cumulative radial distribution of subhalos, averaged over a 5 Gyr period, calculated using cubic spline interpolation (blue line) on a subset of simulation snapshots. The black line shows the radial distribution of subhalos measured using all snapshots.

of subhalos. Using the same sample of subhalos as described for Fig. 2.3, we calculate the velocity of each subhalo by differentiating its position with respect to time (the same method used by Sawala et al. (2017) to avoid difficulties in defining the rest frame velocity of the halo). We then calculate the time-averaged probability distribution of subhalo speeds inside a sphere of radius 20 kpc. The probability distribution was calculated using kernel density estimation (Rosenblatt, 1956; Parzen, 1962), with the bandwidth calculated using Scott's rule (Scott, 2015).

Fig. 2.4 shows how reconstructing subhalo orbits using a cubic spline leads to an underestimation of subhalo speeds near the centre of the halo. The reason for this underestimation is made clear by examining Fig. 2.2, as the total distance travelled by the subhalos as they pass through the centre of the halo is much shorter for orbits calculated using the cubic spline method. Given that this smaller distance is covered in the same time period, the velocity calculated from differentiating the position will clearly be smaller. The size of this effect is to lower subhalo speeds in the central 20 kpc of the halo by an average of around 80 km/s.

2.2.2 Orbit integration

Instead of interpolating, we track the positions and velocities of subhalos between snapshots by integrating their orbits in the potential of the halo, which we assume to be static over this time and, for simplicity, axisymmetric. We model the potential and integrate the orbits using the publicly available codes Galpy and Pynbody (Bovy, 2015; Pontzen et al., 2013). This method accurately reproduces the orbits of subhalos around the host halo, even in situations where the cubic spline method is most prone to failure. By integrating the orbits of subhalos we can accurately estimate subhalo abundances at galactic distances of less than 10 kpc.

To predict the position of a subhalo accurately, choosing the correct frame of reference is paramount. Following the prescription of Lowing et al. (2011) we take the coordinate origin of the halo to be the position of the particle with the minimum potential energy, and the velocity of the parent halo (which is to be subtracted

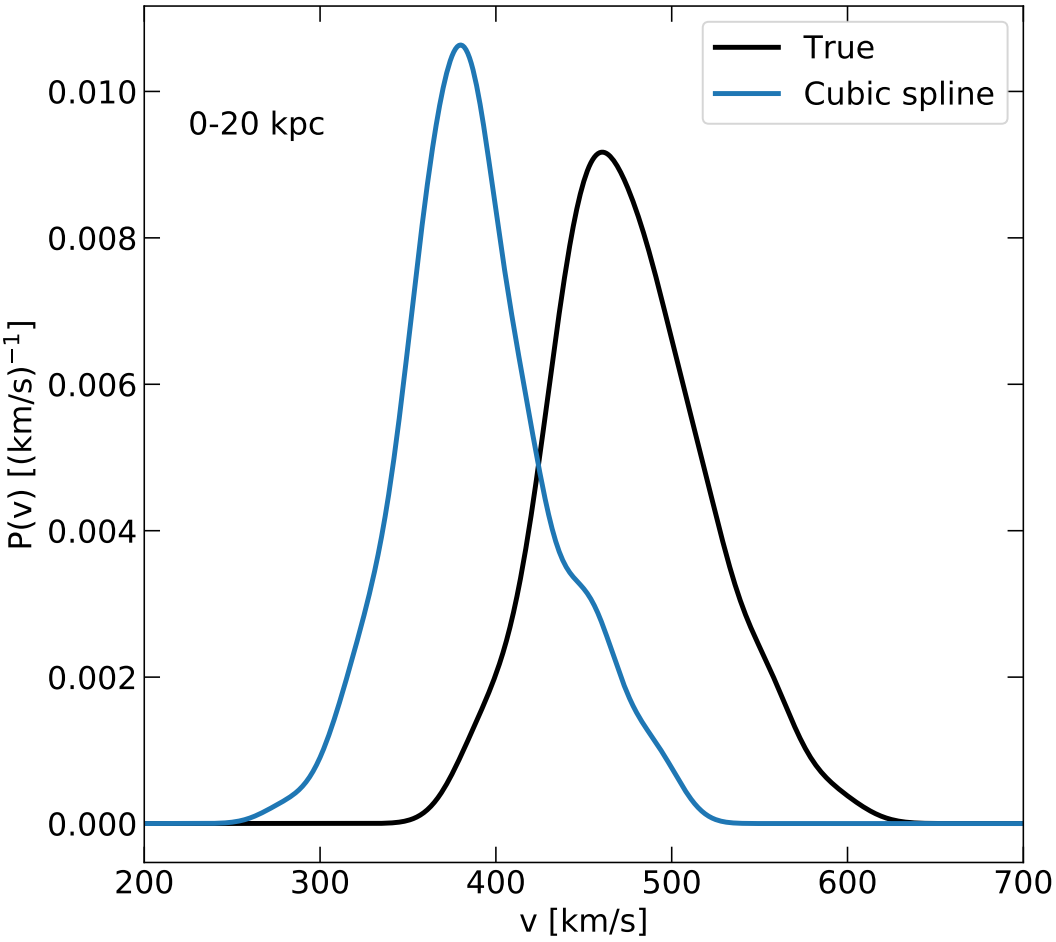

Figure 2.4: Subhalo speed distribution inside a sphere of radius 20 kpc centred on the potential minimum. The results are time-averaged over a period of 5 Gyr. The black line shows the distribution measured using 258 snapshots across this period. The blue line shows the velocity distribution which is inferred when subhalo orbits are reconstructed using the cubic spline method.

from the velocity of the subhalo under consideration) to be the mean velocity of all particles within 5% of r_{200}. We define this reference frame for each snapshot. All calculations are performed in physical coordinates.

We match subhalos between snapshots using a merger tree. To determine the position and velocity of a subhalo between snapshots 1 and 2, in the time interval $t_1 < t < t_2$, we take the following steps:

1. Construct an intermediate "snapshot" by summing the mass distributions of snapshots 1 and 2, halving the mass of each particle.

2. Since the required GALPY routines are written for axisymmetric potentials, we interpolate the mass distribution of the intermediate snapshot on a 2-dimensional $R - z$ grid[1]. We discard particles which are further than 800 kpc from the centre of the halo. The effect of this approximation on the calculated orbits is negligible. The direction of the z-axis is aligned with the net angular momentum of all star particles within 10% or r_{200}.

3. Taking the subhalo at snapshot 1 to be a point mass, integrate its orbit forwards in time in the intermediate potential using the standard GALPY fourth-order symplectic integrator.

4. Integrate the orbit of the subhalo at snapshot 2 backwards in time in the intermediate potential.

5. The orbit of the subhalo is found by taking a weighted sum of the forwards and backwards orbits. The position, $\vec{x}$, of a subhalo at a time t in the interval $t_1 < t < t_2$ is given by:

$$\vec{x}(t) = \vec{x}_f(t)\frac{t_2 - t}{t_2 - t_1} + \vec{x}_b(t)\frac{t - t_1}{t_2 - t_1}, \tag{2.2.1}$$

where $\vec{x}_f$ and $\vec{x}_b$ are the positions of the subhalos being integrated forward and backward in time at time t respectively.

[1] R is the two-dimensional cylindrical radius, and z is the vertical distance.

6. The position and velocity of each subhalo is output every 3 Myr.

To assess the accuracy of the reconstruction of subhalo orbits we perform the following experiment. We select a pair of non-consecutive snapshots from the AURIGA simulation (snapshots 99 and 101, corresponding to a redshift of $z \simeq 0.4$). The time between these snapshots is approximately the same as the time between successive APOSTLE snapshots. Using our method, we calculate the positions of all subhalos at the time of snapshot 100, which we can compare directly with the actual positions calculated at the intermediate snapshot. The results of this test are shown in Fig. 2.5. We can see that orbit integration accurately predicts the positions of subhalos between snapshots, and is therefore an effective tool for studying the dynamics of substructure close to the centre of the halo. The blue points in Fig. 2.5 show the results of the same test when applied to subhalo orbits calculated using the cubic spline method. It is clear that orbit integration does not suffer for the same radial bias described in §2.2.1.

2.3 The abundance of substructure in galactic halos

The central galaxies that form in the AURIGA simulations are significantly more massive than those that form in the APOSTLE simulations, even though they both have broadly similar halo masses. We show in this section that the mass of the galaxy has a marked effect on subhalo abundance, even at distances well beyond the edge of the galaxy. In Fig. 2.6 we compare the radial distribution of subhalos in the APOSTLE, AURIGA and DMO simulations. The effect of the larger AURIGA galaxies is to reduce the abundance of subhalos at all radii. We find that the size of the reduction depends strongly on radius but is broadly independent of mass for subhalos in the range $10^{6.5} - 10^{8.5}$ $M_\odot$, in agreement with the conclusions of Sawala et al. (2017).

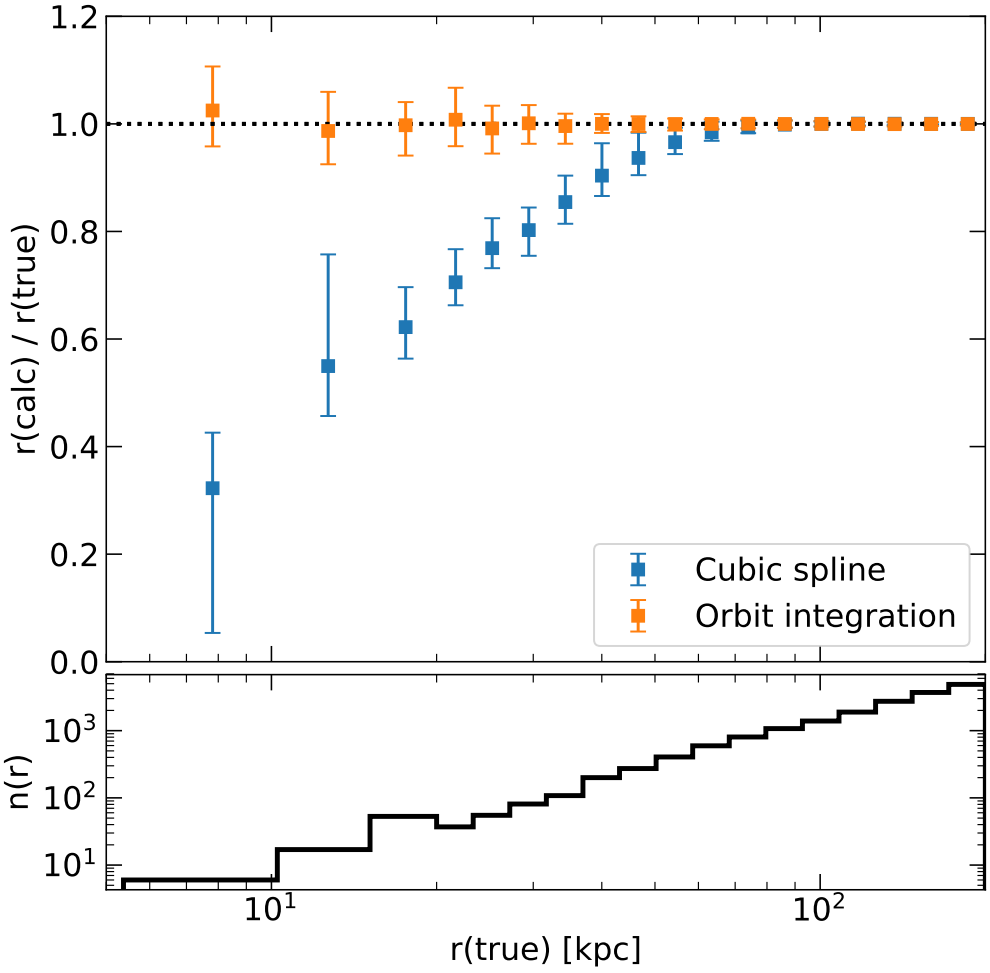

Figure 2.5: The accuracy of orbit integration at predicting the orbital radii of subhalos at an intermediate snapshot. For reference, we compare this method to the cubic spline described in Sawala et al. (2017) and also used in Garrison-Kimmel et al. (2017). The lower panel shows the number of subhalos in each radial bin used for the calculation.

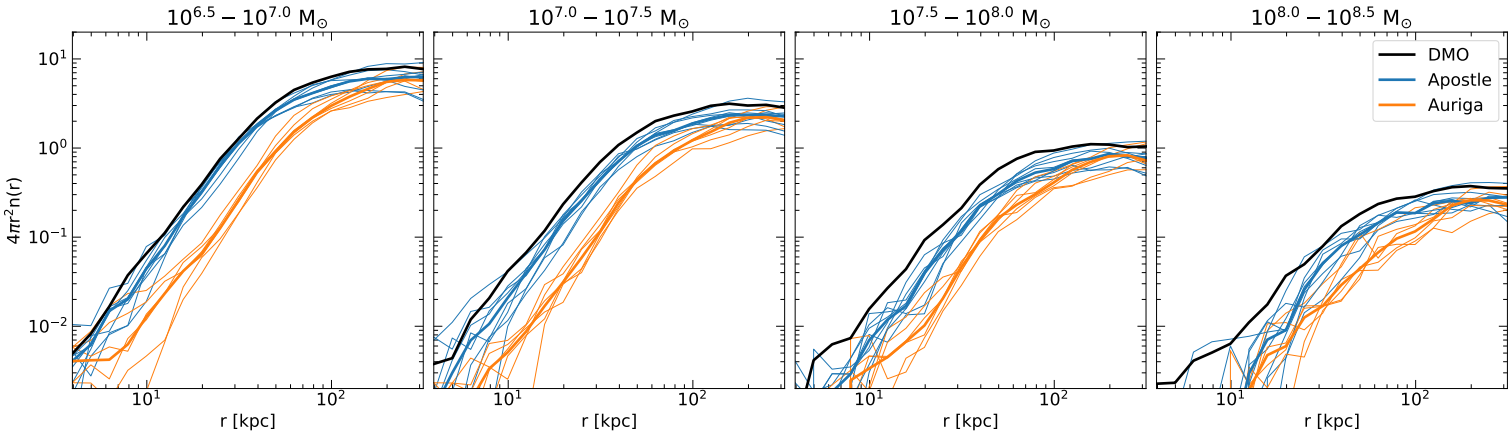

Figure 2.6: Linear density of subhalos in hydrodynamical and DMO versions of the Apostle (blue) and Auriga (orange) simulations as a function of radius. Thin lines show values for individual halos, whilst thick lines show the median values for all halos. The black line shows the median radial density of subhalos in all DMO simulations. Each panel corresponds to a different subhalo mass bin as indicated. The results are time averaged over a period of 5 Gyr.

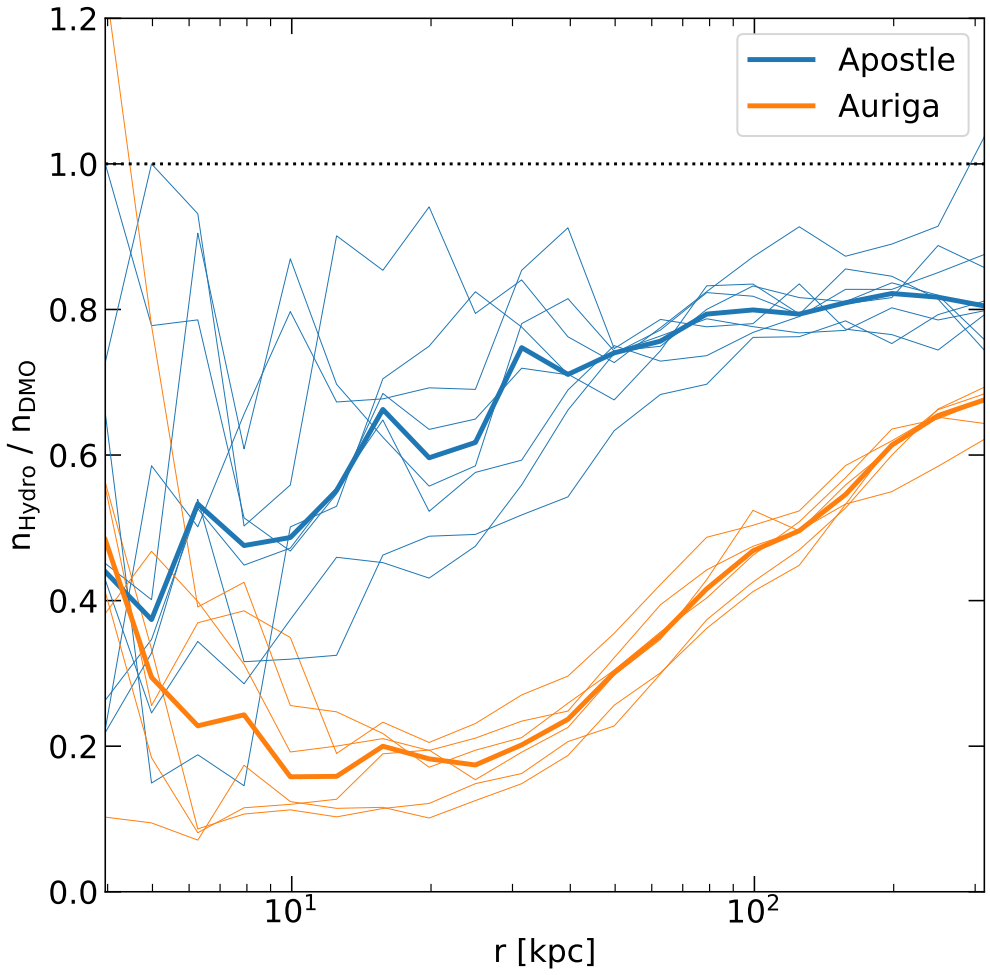

Figure 2.7: Ratio of the radial number density of subhalos in hydrodynamical and DMO versions of the Apostle (blue) and Auriga (orange) simulations, for subhalos with masses in the range $10^{6.5} - 10^{8.5}$ $M_\odot$. Thin lines show the reduction in subhalo abundance for individual halos and the thick lines the median of the thin lines.

The reduction in subhalo abundance as a function of radius is shown explicitly in Fig. 2.7. Fundamental tests of the CDM model, for example using stellar streams to search for substructure, are sensitive to substructure within ∼20 kpc of the centre of the halo (or equivalently ∼ 10% of r_{200} for a Milky Way-sized halo). At these radii, the presence of the galaxy reduces the substructure abundance by 50% in the Apostle and by 80% in the Auriga simulations relative to the DMO case. The Apostle simulations predict over twice as many dark (i.e. low-mass) substructures as the Auriga simulations.

In Fig. 2.8 we show the differential subhalo mass functions in four spherical shells in the DMO and hydrodynamical versions of the Apostle and Auriga simulations. Power-law fits to the differential mass functions have slopes between -1.8 and -1.9 in the two outermost shells, consistent with the findings of both Springel et al. (2008) and Sawala et al. (2017). At distances less than 20 kpc from the halo centre (left panels) we find that the slopes of the mass functions in the Auriga hydrodynamical simulations are significantly shallower than the corresponding slopes in Apostle, suggesting that the implementation of baryonic physics in Auriga leads to a more pronounced reduction of small-mass relative to high-mass halos. This is simply because less massive halos are more prone to tidal disruption, rather than any systematic difference between the orbital distributions of smaller and larger halos. We fit the median mass function in each radial bin with a power law using a non-linear least squares method. In the innermost radial bin the slope in the Auriga hydrodynamical simulations is -1.4, whereas the slope in Apostle simulations is -1.7. Values for all power-law fits are listed in Table 2.1.

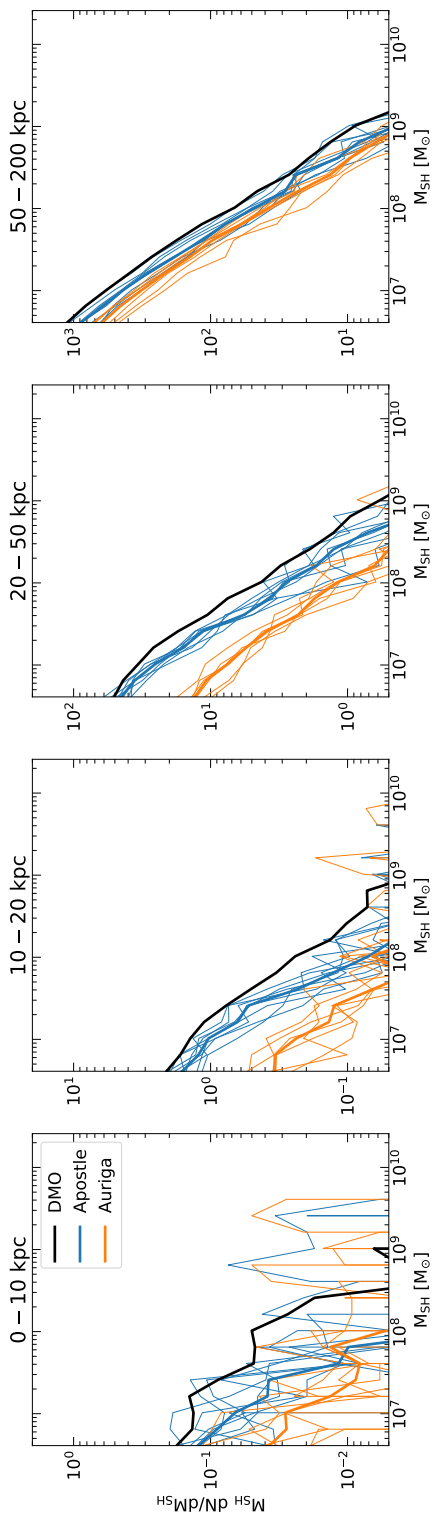

Figure 2.8: Differential subhalo mass functions for subhalos in the APOSTLE (blue) and AURIGA (orange) hydrodynamical simulations in concentric spherical shells, averaged over a period of 5 Gyr. Thin lines show the mass functions of individual halos, whilst solid lines show the median mass functions. The thick black lines show the median subhalo mass function of all APOSTLE and AURIGA DMO subhalos in each radial bin.

	0-10	10-20	20-50	50-200
Apostle DMO	-1.74	-1.88	-1.90	-1.91
Auriga DMO	-1.69	-1.77	-1.92	-1.93
Apostle Hydro	-1.73	-1.86	-1.92	-1.93
Auriga Hydro	-1.44	-1.64	-1.82	-1.94

Table 2.1: Power-law slopes for differential subhalo mass functions in the mass range $(10^{6.5} - 10^{8.5})M_\odot$ in DMO and hydrodynamical simulations, in four spherical shells. The width of each spherical shell (top row) is given in kpc.

2.4 Subhalo abundance far from the central galaxy

As the distance from the central galaxy increases, the reduction in subhalo abundance caused by the inclusion of baryonic physics should asymptote to a constant value, at a radius where the tidal field of the central galaxy has no impact on the evolution of small halos. This can be seen clearly in Fig. 2.9, which shows that the ratio of subhalo abundance in the hydrodynamical and DMO simulations rises with distance from the centre of the halo, until it begins to plateau at a radius of ~ 300 kpc. The radius at which the reduction in subhalo abundance plateaus to a constant value is significantly outside of r_{200} for the Auriga simulations, which have a typical r_{200} of 220 kpc. Thus, the impact of the central galaxy seems to extend surprisingly far, well beyond the extent of the galactic disks.

2.4.1 Global effects

The reason that the lines in Fig. 2.7 do not plateau at a value of 1 is because we computed the number density of subhalos in fixed mass bins. In DMO simulations, the baryonic mass is collisionless: around 15% (the value of Ω_b/Ω_m) of the mass of each simulation particle represents "collisionless baryons". In hydrodynamical simulations, low-mass halos lose much of their baryonic mass during reionisation or, subsequently, through galactic winds powered by supernovae. DMO halos cannot undergo this mass loss, and so they will be approximately 15% more massive than their

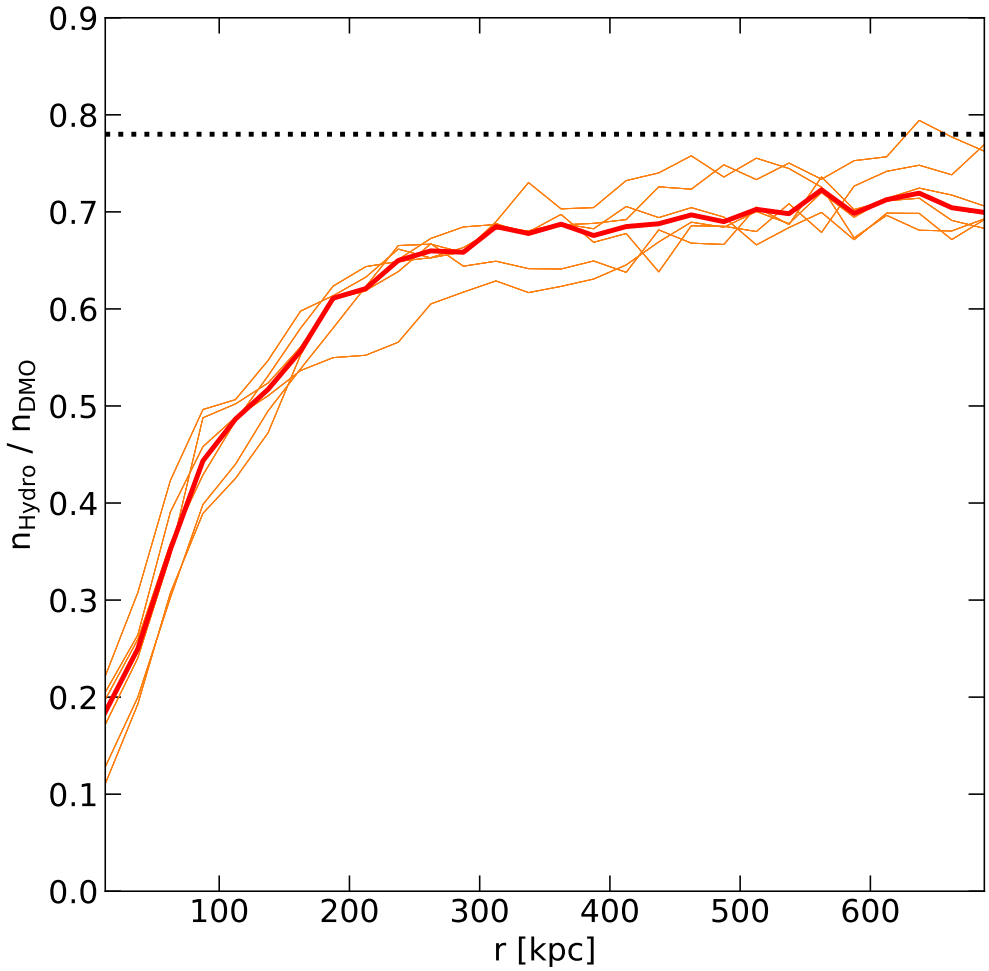

Figure 2.9: The ratio of the radial number density of subhalos in hydrodynamical to DMO versions of the AURIGA simulations for subhalos in the mass range $(10^{6.5} - 10^{8.5})\mathrm{M}_{\odot}$. Thin orange lines show the reduction in subhalo abundance for individual halos, and the thick red line shows the median of the thin orange lines. The dotted black line shows the reduction in subhalo abundance due to global simulation effects shown in Fig. 2.10.

hydrodynamical counterparts at early times. This difference in mass is exacerbated with time because more massive halos accrete mass at a higher rate than smaller mass halos and thus grow faster. For an isolated 10^8 $M_\odot$ halo at redshift $z = 0$, this difference in mass between the same object with hydrodynamics or DMO is typically around 20-30% (Sawala et al., 2013, 2016).

We quantify the magnitude of this effect using the following procedure. We match halos between the DMO and hydrodynamical versions of a simulation using the particle matching criteria of Bose et al. (2017), in which the 50 most bound DM particles of halos are matched bijectively between the DMO and hydrodynamical simulations. We then form a matched "field" sample by selecting halos which are at least 500 kpc from a galaxy in the hydrodynamical version of the simulation, so as to avoid any differences due to evolution in the tidal field of the main halo. For each Auriga level 3 volume, we have approximately 1000 matched objects with mass between 10^7–10^8 $M_\odot$. The numbers for Apostle are significantly larger as a greater fraction of the simulation is field volume. For each pair of matched halos we calculate the ratio of their masses. We take a DMO halo's "effective mass" to be the mass assigned to it by the Subfind algorithm, multiplied by the median of the distribution of mass ratios of this matched sample. The distributions of mass ratios before and after this procedure are shown in Fig. 2.10. When the masses of DMO subhalos are corrected by the median mass ratio, the peak of the mass ratio distribution will occur at a value of 1, by construction (this would not be the case if we had corrected by the mean mass ratio). The width of the corrected distribution is around 30% larger for the corrected distribution. The results shown in Fig. 2.10 are calculated using only subhalos at redshift $z = 0$. We have checked that for redshifts between $z = 1$ and the present day, the size of this effect is independent of redshift.

We find that the correction factor has no dependence on mass for halos with DMO masses between $10^7 - 10^9$ $M_\odot$. For the Auriga simulations, we find a median correction factor of 0.76, and the interquartile range of of correction factors is

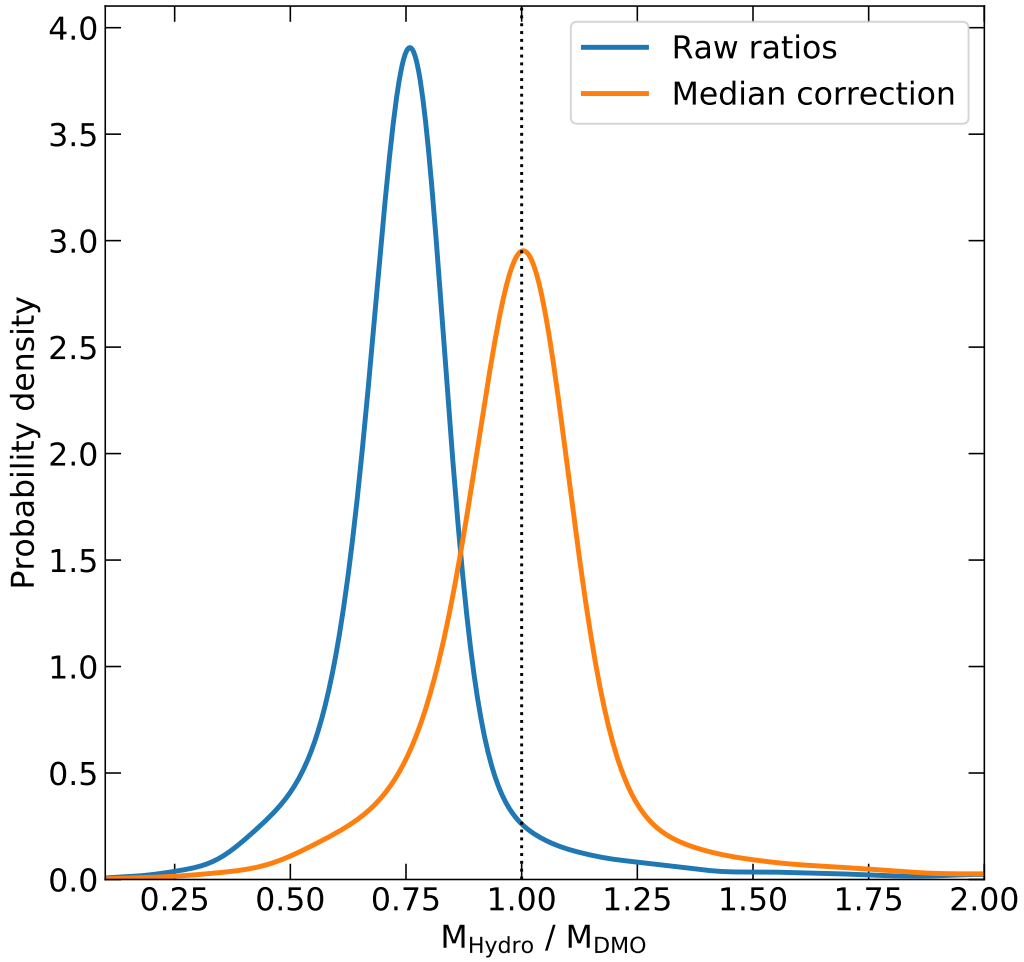

Figure 2.10: Distribution of the ratios of the masses of halos matched between DMO and hydrodynamical versions of a simulation. The blue line shows the distribution of mass ratios when no correction has been applied. The orange line shows the distribution of mass ratios after the masses of DMO halos have been multiplied by the median of the blue distribution (a value of 0.76).

0.12. For the APOSTLE simulations the median correction factor is 0.75, due to the slightly different choice of cosmological parameters in the simulation. We find that this correction procedure does not work well for halos with masses below 10^7 $M_\odot$. The probability of a halo being matched between simulations falls steeply for halos smaller than this. Furthermore, the distribution of mass ratios will be biased as the resolution limit of the simulation imposes a limit on the smallest possible mass ratio. Therefore, when correcting halo masses, we restrict our attention to halos with masses greater than 10^7 $M_\odot$.

We can quantify the contribution of this effect to the overall reduction in abundance as follows. We assume a power-law mass function of the form,

$$\frac{dN}{dM_0} = kM_0^\alpha \ , \tag{2.4.1}$$

where M_0 is the DMO mass. The mass of the subhalo in the hydrodynamical simulation is given by $M_1 = \beta M_0$. Thus,

$$\frac{dN}{dM_1} = k\beta^{-\alpha-1}M_1^\alpha \ , \tag{2.4.2}$$

so the ratio of the mass functions is given by $\beta^{-\alpha-1}$. Taking values of $\alpha = -1.9$ for the power law slope of the subhalo mass function(Springel et al., 2008), and $\beta = 0.76$ for the the difference in growth history the hydrodynamical and DMO simulations) gives a value of 0.78 for the ratio of the mass functions, corresponding to a 22% reduction in the number of objects.

2.4.2 The long arm of the galaxy

We have already remarked upon the surprising result that the reduction in subhalo abundance due to the tidal field of the central galaxy extends well beyond the physical extent of the galactic disk. Here we explain this result.

Splashbacks

The number of halos that have been in and out of the main halo is larger in the DMO than in the hydrodynamical simulations. To show this, we count the number of halos of mass $(10^7 - 10^8)$ $M_\odot$ in a spherical shell between 200 and 300 kpc. For each subhalo we check if it has previously been close to the central galaxy[2]. We find that the difference in the number of subhalos between the hydrodynamical and DMO simulations is strongly correlated with the difference in the number of subhalos that have been close to the centre of the halo. In other words, at large radii there exists a population of DMO subhalos that have fallen into the halo, survived their passage through the centre, and reemerged. These are sometimes called "splashback halos"; (Gill et al., 2005). Many of their hydrodynamical counterparts do not survive the encounter with the galaxy at the centre of the halo, and so we observe the abundance ratio continuing to rise to distances of 300 kpc from the centre of the halo, well beyond r_{200}. The results of this calculation for the level 4 suite of Auriga simulations are shown in Fig. 2.11. Here we compare results with and without the mass correction described above. We see a clear correlation in both cases; however, when the mass correction is applied, the points fall roughly along the expected 1:1 line.

Stripping

We can also use our matched sample of subhalos to assess the role of mass stripping (rather than complete destruction) in the reduction in subhalo abundance. The steepness of the subhalo mass function means that it is possible to measure a reduction in subhalo abundance in a particular mass bin, if subhalos undergo significant stripping without any destruction taking place at all. We select a sample of matched subhalos that lie between 300 and 400 kpc from the centre of the halo at $z = 1$, have a mass in the DMO simulation in the range $(10^{6.5} - 10^{8.5})$ $M_\odot$. We also specify

[2]We adopt a radius of $0.7 \times r_{200}$ as our definition of 'close'. This is a typical radius at which the tidal forces from the spherically averaged mass distributions in the hydrodynamical simulations are equal to the tidal forces in the DMO simulations.

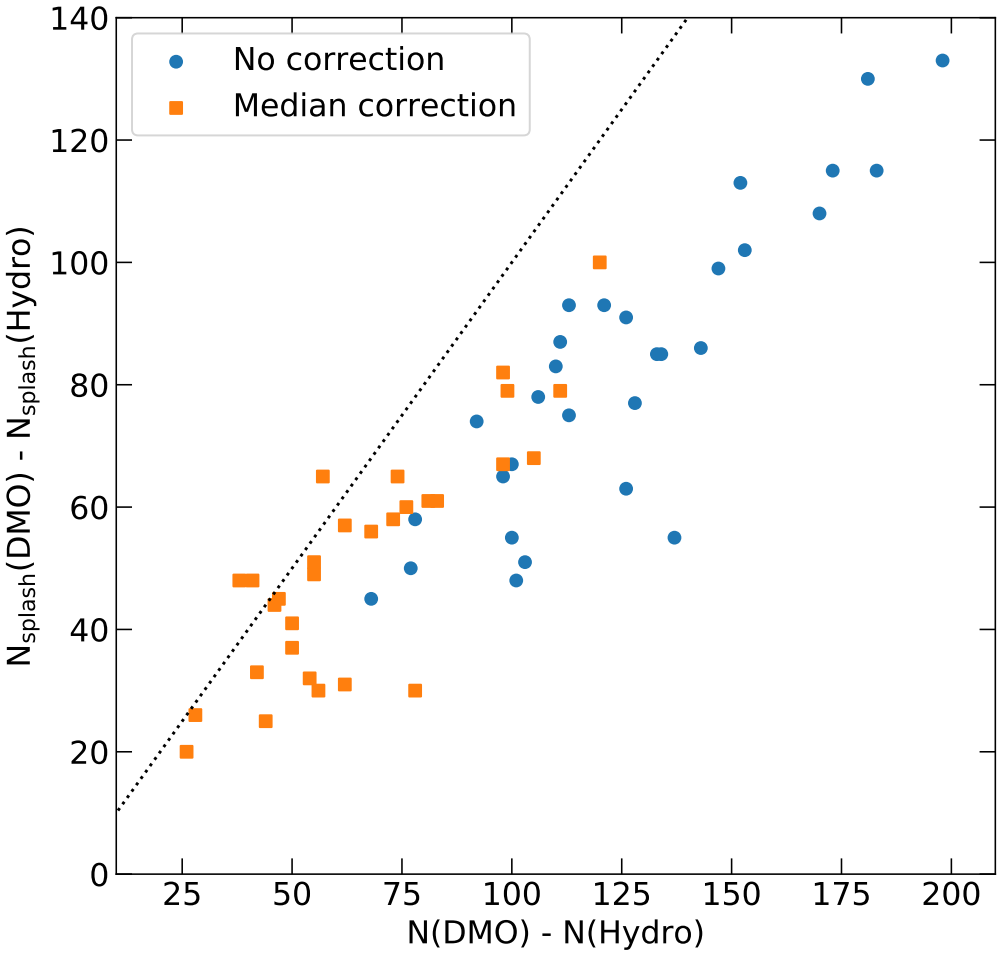

Figure 2.11: Difference in the number of subhalos with masses in the range $(10^7 - 10^8)$ $M_\odot$in a spherical shell of width 200–300 kpc in the DMO and hydrodynamical simulations plotted against the difference in the number of subhalos in this shell that have previously been inside 70% of r_{200}(labelled by the subscript *splash*). Each point represents a halo from the level 4 Auriga suite of simulations. The blue points show the halos where we have not applied any correction to the masses of DMO subhalos. The orange points show the result when we correct the masses of DMO subhalos by the median ratio shown in §2.4.1.

that the subhalos in our sample must survive to the present day, and pass within the virial radius of the halo. Although we do not specify it in advance, we find that the dynamics of these matched objects, specifically their average distance from the centre of the main halo as a function of time, is identical in the hydrodynamical and DMO samples.

Fig. 2.12 shows the median reduction in subhalo mass as a function of time. DMO subhalos lose an average of 41% of their mass, whilst subhalos in Auriga lose an average of 59%. Thus, a halo in the hydrodynamical simulation with the same initial mass as its DMO counterpart at redshift $z = 1$ will be, on average, about 30% less massive today, even if it shares the same radial distance history. This merely reflects the enhanced tidal stripping in the later case due to the presence of the massive central galaxy.

We can quantify the effects of stripping on subhalo abundance using the same method we employed to quantify global effects in §2.4.1. Taking the ratio of the mass functions as $\beta^{-\alpha-1}$, we set $\alpha = -1.9$ and $\beta = 0.7$. This value of β is chosen as the ratio of the amount of stripping in hydrodynamical and DMO simulations shown in Fig. 2.12. This gives a ratio of 0.72 of the mass functions, corresponding to an 28% reduction in the number of objects. This stripping effect is the dominant cause for the reduction in subhalo abundance for distances greater than 200 kpc from the centre of the halo. Stronger stripping in the hydrodynamical simulations also explains why the orange points (i.e. with corrected masses) in Fig. 2.11 lie slightly below the 1:1 line on average.

2.5 Subhalo velocities

An accurate estimate of the expected velocity distribution of low mass substructures is a critical input into methods to search for small-mass dark substructures from measured gaps in cold stellar streams. In this section we examine the velocity distributions in our simulations; contrasting the two sets, we can gain some insight

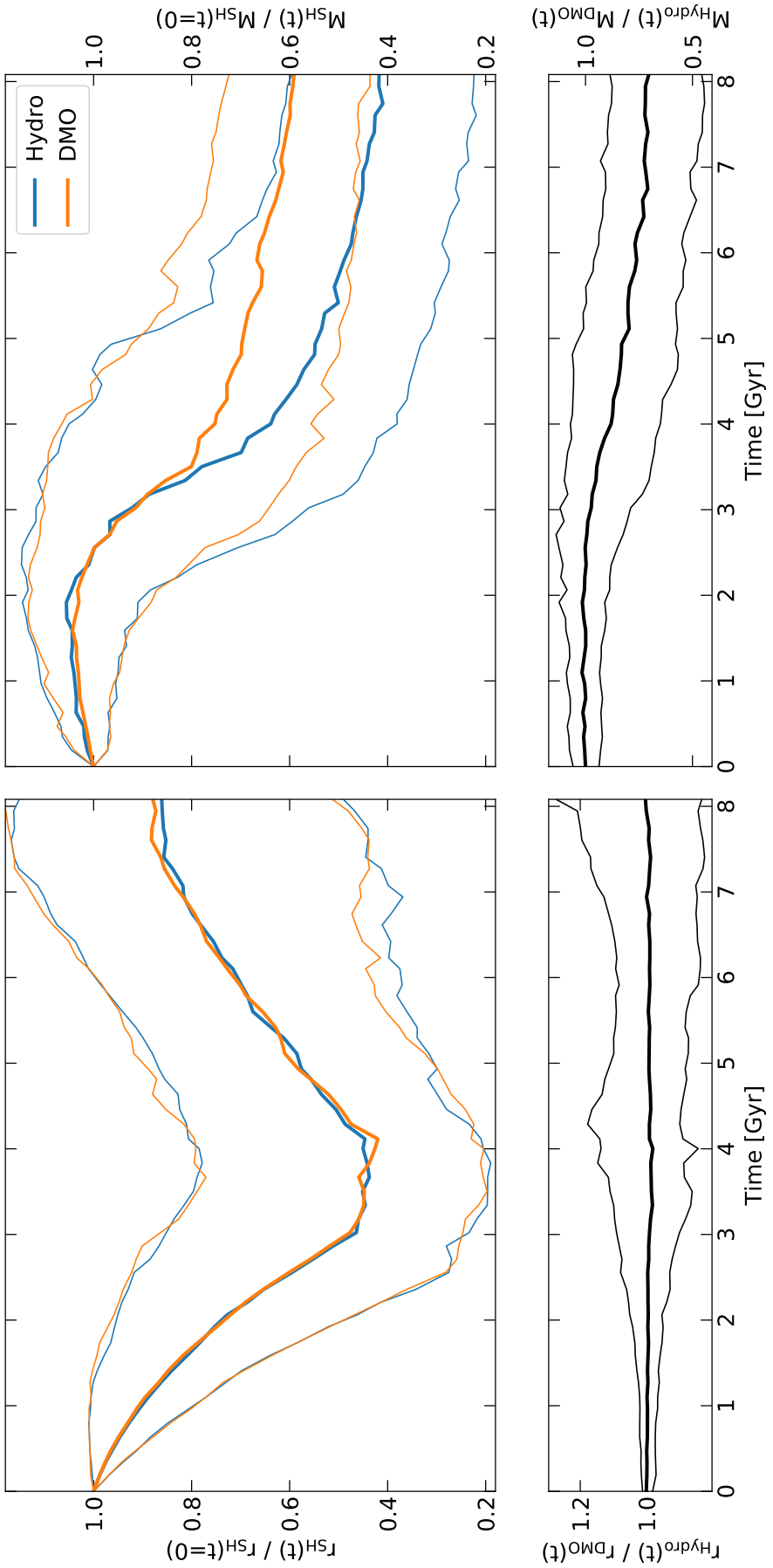

Figure 2.12: The radial (left column) and mass (right column) histories of a set of matched subhalos between redshift $z = 1$ and the present day. Large panels show subhalo radii(masses) relative to their radius(mass) at $z = 1$. Thick lines show the median evolution of each sample, whilst thin lines indicate 68% scatter. Small panels show the relative change in radius(mass) between matched subhalos over this time period.

into the size of the theoretical uncertainties in these distributions. This topic has been explored already by, for example, Sawala et al. (2017).

To obtain a robust estimate of the velocity distributions, we employ kernel-density estimation (Rosenblatt, 1956; Parzen, 1962), using a Gaussian kernel and applying Scott's rule to estimate the bandwidth (Scott, 2015). The distribution of subhalo speeds as a function of radius is shown in Fig. 2.13. The presence of the central galaxy affects the distributions relative to the DMO case for both hydrodynamical sets of simulations. The impact of the more massive central galaxies in the Auriga simulations is clear. The depth of the potential well is larger, leading to a greater radial acceleration as subhalos fall inwards. This effect of the central galaxy is also manifest in the Apostle simulations but it is much weaker reflecting the smaller masses of the central galaxies. We note that no such effect was observed by Sawala et al. (2017), probably as result of inaccuracies in their interpolation scheme.

We find that the distribution of subhalo speeds is generally well fit by a Rician distribution, in agreement with Sawala et al. (2017). The Rician distribution is a two-parameter model given by

$$f(x \mid \nu, \sigma) = \frac{x}{\sigma^2} \exp\left(\frac{-(x^2+\nu^2)}{2\sigma^2}\right) I_0\left(\frac{x\nu}{\sigma^2}\right), \tag{2.5.1}$$

where I_0 is the modified Bessel function of the first kind with order zero. The ν parameter controls the location of the peak, with a value of 0 giving a Maxwellian distribution. The σ parameter controls the width of the distribution. The parameters of the fits are given in Table 2.2.

The distributions of subhalo *radial* velocities in the same radial bins used in Fig. 2.13 are shown in Fig. 2.14. Sawala et al. (2017) found that close to the halo centre, the distribution of subhalo radial velocities in the Apostle simulations was well described by a double Gaussian. Fig. 2.2 shows how plunging orbits calculated using the cubic spline interpolation method pass closer to the centre of the halo than the true orbits, with a velocity that is predominantly tangential during most of the passage through the central region. This is a general feature of orbits constructed

Figure 2.13: Probability distributions of the speed (relative to the host halo) in spherical shells for subhalos of mass in the range $(10^{6.5} - 10^{8.5})$ $M_\odot$ in the APOSTLE (blue) and AURIGA (orange) simulations. Thick black lines show the median velocity distribution of all DMO subhalos in each bin.

	0-10	10-20	20-50	50-200
Apostle DMO	351, 110	310, 101	242, 97	167, 78
Auriga DMO	384, 68	355, 66	285, 75	191, 71
Apostle Hydro	379, 75	326, 83	249, 81	165, 71
Auriga Hydro	554, 48	480, 43	356, 56	211, 63

Table 2.2: Values of the parameters ν and σ obtained from fitting a Rician distribution to the median values of the velocity distributions shown in Fig. 2.13, in km/s. Each column correspond to a different radial bin, with the width of the shell in kiloparsecs.

using the cubic spline interpolation method. Consequently, the dearth of low-radial velocity orbits reported by Sawala et al. (2017) is an artifact of their orbit reconstruction method. This explains why the velocity distributions that we find in the top left panel of Fig. 2.14 do not show such a pronounced dip around $v_{\rm rad} = 0$. In the 50–200 kpc radial bins, we see that one of the Auriga systems has an unusually bimodal velocity distribution. This distribution is the result of an interaction with another halo between redshift $z = 0.5$ and the present day. A population of subhalos belonging to the passing halo have flown in and out of the edge of the halo, resulting in a peak of the negative radial velocity whilst infalling, and a peak in the positive radial velocity distribution after pericentre.

We can see in Fig. 2.14 that the deeper gravitational potential the in hydrodynamical simulations relative to the DMO case leads to a broadening of the radial velocity distribution, with the effect being most pronounced in the Auriga simulations at small radii. This effect is a combination of a greater radial acceleration and the preferential disruption of objects on more circular orbits near the centre of the halo. We also note that the distributions are remarkably symmetrical, even in the outermost spherical shell. This shows that the subhalo abundance at all radii reflects a balance between inflow and outflow.

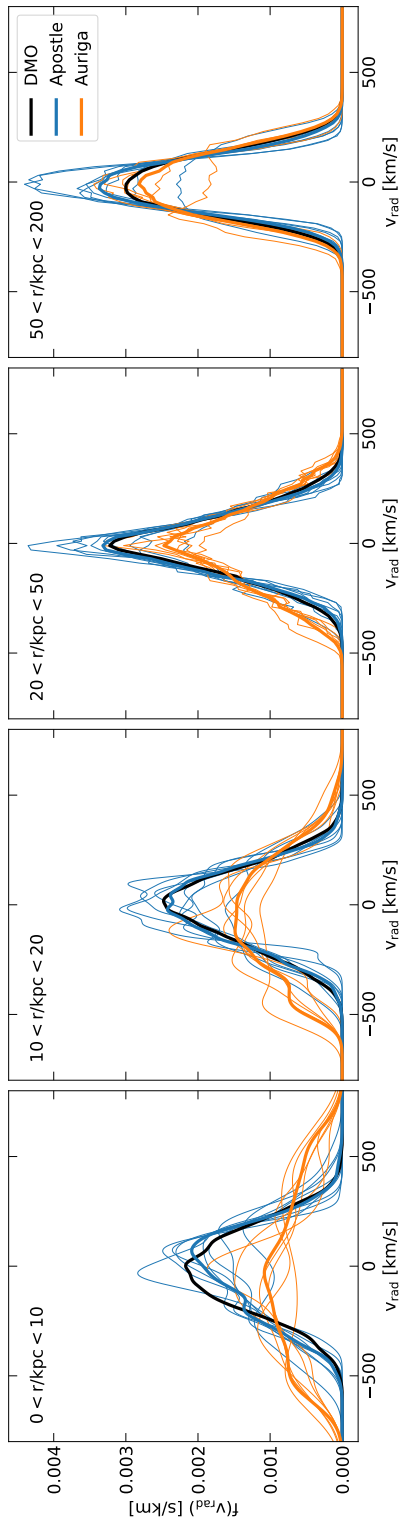

Figure 2.14: Probability distributions of radial velocities (relative to the host host halo) in spherical shells for subhalos with masses in the range $(10^{6.5} - 10^{8.5})$ $M_\odot$ in the APOSTLE (blue) and AURIGA (orange) simulations. Thick black lines show the median velocity distribution of all DMO subhalos in each bin.

2.6 Conclusions

The large number of small-mass halos predicted by N-body simulations to form in a ΛCDM universe provide a key test of the paradigm. In practice, however, the clear-cut predictions from N-body simulations are only part of the answer, as some of these small halos that fall into larger ones can be destroyed by tidal forces whose strength depends on the contents of the halo, particularly the galaxy at the centre. Thus, rigorous predictions for the abundance of subhalos requires modelling the baryonic processes that lead to the formation of the galaxy. In this chapter, we have investigated how the abundance and velocity distribution of small-mass subhalos ($\sim 10^{6.5} - 10^{8.5}$ $M_\odot$) within galaxy-size halos is affected by baryon processes and we have compared two different implementations of such processes using the independent Apostle and Auriga simulations.

Since subhalos are quite rare near the centre of the host halo and are poorly sampled in the limited number of available simulation outputs, to study their orbits we have integrated the orbits of subhalos between snapshots, using the publicly available code Galpy. The results we present are obtained by averaging over a lookback period of 5 Gyr.

We find that the abundance of substructures is significantly affected by the way in which baryon processes are treated. At 10% of the virial radius, r_{200}, the abundance of low-mass substructures is reduced relative the dark matter-only (DMO) simulations by around 50% and 80% in the Apostle and Auriga simulations respectively. We also find differences in the slope of the subhalo mass function and the width and peak location of the velocity distributions, all of which can be explained by the different masses of the galaxies that form at the centre of the halos in the two simulations. The more massive central galaxies in Auriga result in larger tidal forces, which cause enhanced destruction and stripping of substructures. Perhaps surprisingly, we find that the abundance of subhalos in the hydrodynamical simulations is still lower than in the DMO simulations even well beyond the virial radius

of the halo, particularly in Auriga. This happens because objects that spend the majority of their orbit far from the central galaxy have highly radial orbits which take them past the virial radius; some of the objects that emerge unscathed from the DMO simulation, are destroyed in the hydrodynamical counterpart.

A deeper potential also causes subhalos to accelerate more as they move towards the centre of the halo, leading to an increase in the width of the radial velocity distributions. We also find that the peak of the distribution of subhalo speeds is shifted to significantly higher values in the hydrodynamical simulations, with the largest changes occurring near the centre of the Auriga simulations.

Sawala et al. (2017) and Garrison-Kimmel et al. (2017) investigated similar processes to those we have studied here, the former using the same Apostle simulations that we too have analyzed. Our results differ significantly from theirs. We have shown that this is because the cubic spline method they used to interpolate orbits between snapshots is insufficiently accurate to follow the orbits near the centre of the halo. Our orbit integration method predicts less substructure at small distances from the halo centre. We also do not observe the velocity biases described by Sawala et al. (2017). However, we find that the conclusion of Sawala et al. (2017) that objects on radial orbits are more likely to undergo disruption by the central galaxy holds true.

Roughly speaking the Apostle and Auriga simulations bracket the range of theoretical uncertainty for the abundance and velocity distribution of substructures near the centre of a galaxy like the Milky Way. Apostle underpredicts the mass of the Milky Way by factors of 2-3, whereas, on average, the Auriga galaxies overpredict it by factors of 1.5-2. The halo-to-halo variations in the velocity distributions is smaller than the differences seen in our two hydrodynamical simulations. This size of theoretical uncertainty is eminently reducible by improved modelling of the baryonic physics of galaxy formation.

Chapter 3

Simulating a galaxy group and its large scale environment

3.1 Introduction

BSERVATIONS of distortions in strong lensing arcs offer one of the most promising avenues for constraining the abundance of dark halos in our universe (Koopmans, 2005). A convincing non-detection of 10^7 $M_\odot$ halos has the power to entirely rule out the CDM model. To make such a strong statement, the lensing signal predicted by the CDM model must be well-characterised. Li et al. (2017) have shown that the majority of the lensing signal originates from field halos between the source galaxy and the observer, however, up to 30% of the lensing signal is sourced by substructure within the lensing halo in the CDM model (Despali et al., 2018). When calculating the predicted subhalo and field halo contributions to the lensing signal, both Li et al. (2017) and Despali et al. (2018) use results from DMO simulations. We have shown in Chapter 2 that the inclusion of baryonic physics in simulations has major effects on the subhalo population of Milky Way mass halos. The size of these effects in general depends on the size and shape of the galaxy at the centre of the halo. Halos which produce visible lensing arcs are typically ten times more massive than the central halos studied in Chapter 2 (Bolton et al., 2008). Accounting for the effects of baryonic physics in predictions of the lensing signal will therefore require specialised simulations.

Simulating 10^{13} $M_\odot$ halos with a small enough particle mass to resolve the population of 10^7 $M_\odot$ subhalos necessary for strong lensing tests, whilst also including the effects of baryonic physics on the subhalo population, is computationally very expensive. We describe and implement a new way of setting up the initial conditions of a cosmological simulation, so that dark matter particle outnumber gas particles by 7:1. This approach allows us to resolve low-mass substructures within a 10^{13} $M_\odot$ halo, whilst reducing the computational burden of the simulation by simulating the baryonic matter at a lower level of resolution than would be typical for this

level of dark matter resolution. This approach is sufficient to accurately model the subhalo population of our simulated halo, as the dominant impact of baryonic physics on these subhalos is due to the interaction between the subhalos and the central galaxy of the halo, whose mass and size can be well-resolved with lower-resolution simulation elements. This approach has the added benefit of largely avoiding the spurious growth of galaxies described in Ludlow et al. (2019), which results 2-body scattering producing an artificial equipartition of energy between stellar and dark matter particles due to their different masses. In the simulation described in this chapter, the masses of dark matter and gas particles are approximately equal.

In this chapter we describe the construction of the initial conditions. We test the effects of changing the dark matter-gas mass ratio by running a new realisation of the EAGLE 25 Mpc volume using our new initial conditions. We use our simulation to study the environmental dependence of the halo mass function for the low-mass field halos important for lensing tests of the CDM model.

3.2 Methods

3.2.1 Candidate selection

Despali & Vegetti (2017) identified a sample of halos in the EAGLE 100 Mpc simulation (Schaye et al., 2015) which have similar properties to lenses detected using the SLACS Survey (Bolton et al., 2006). The following criteria were used to select halos:

- The halo is identified at a redshift of approximately $z = 0.2$. This a typical redshift at which lensing galaxies are observed in the SLACS survey.
- The halo must be relaxed (using the criteria of Neto et al. (2007)). Methods such as those used by Vegetti et al. (2012) rely on the assumption that the central lensing halo may be modelled as a smooth isothermal sphere. If the halo is unrelaxed, this assumption will not be valid.

- The halo has a virial mass between 10^{12}–$10^{14.5}$ $M_\odot$. Less massive halos will not produce visible Einstein rings.

- The central galaxy is an elliptical. Specifically, at least 25% of all star particles inside 20 kpc must be counter-rotating, where direction of rotation is given by the total angular momentum of all star particles in this region. The SLACS survey was optimised to detect bright, early-type lens galaxies, as these are most suitable for detailed lensing and photometric studies.

- The halo has a velocity dispersion of between 160–400 km/s inside the half-mass radius[1]. Again, this criterion is chosen to maximise the similarity between the simulated galaxies and the galaxies detected in the SLACS survey.

From the sample of halos we select one object for resimulation. In the EAGLE 100 Mpc volume run with the REFERENCE model, the halo has a FOF ID of 129, a mass of $M_{200} = 10^{13.1}$ $M_\odot$, and is located at at [89.742, 42.189, 94.507] Mpc.

3.2.2 Initial conditions

We utilise a zoom simulation to study the halo selected using the criteria above. This allows us resolve the low-mass substructures relevant for tests of the CDM model whilst minimising the computational burden. We identify all particles which are less than 5.5 Mpc from the potential minimum of the halo at redshift $z = 0.2$. We trace these particles back to their comoving coordinates at the Big Bang using the Zel'dovich approximation (Zel'dovich, 1970). This defines the region of space known as the Lagrangian region, which is the patch of the universe from which our target halo will form.

To perform a zoom simulation, the Lagrangian region is populated with particles which have smaller masses than the particles of the parent simulation. The rest of the volume is populated with more massive particles, present only to reproduce the

[1]The half mass radius is calculated in projection, averaging over three orthogonal directions.

correct large scale tidal forces without significantly increasing the overall computational burden. The particles which populate the Lagrangian region must arranged such that i) the whole region has the mean density of the universe, ii) the configuration of particles is very close to being gravitionally stable. Any instabilities in the initial conditions which are not due physical effects will lead to the rapid growth of artificial structure.

For DMO zoom simulations, the Lagrangian region can simply be populated with a uniformly-spaced grid. For hydrodynamical simulations, one takes the uniform grid of DMO particles and splits each DMO simulation particle into a gas particle and a dark matter particle. The mass of each pair of particles is the same as the DMO particle, and they are placed such that their centre of mass is the same as the position of the DMO particle. This is the standard method, as used for example in the Apostle or Auriga simulations. In this setup there is one dark matter particle per gas particle, and the ratio of the particle masses is determined by the cosmological parameters of the simulation, i.e. $m_{DM}/m_{gas} \equiv \Omega_{DM}/\Omega_b$. In the Planck 2015 cosmology, this means that each dark matter particle is 5.36 times heavier than a gas particle.

Our approach differs from the method outlined above by creating initial conditions which have 7 dark matter particles per gas particle. This means that the ratio of the particle masses is given by $m_{DM}/m_{gas} \equiv \Omega_{DM}/7\Omega_b \sim 0.77$. To ensure uniform matter density, and to avoid gravitational instabilities (especially at the boundary of the Lagrangian region), we populate the Lagrangian region with a template, shown in Fig. 3.1.

Each template contains one gas particle, which sits at the centre of the cell. The template also contains 26 dark matter particles, positioned on the faces, edges and vertices of the cell. When two templates are placed next to each other,

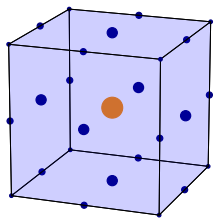

some particles from each template will occupy the same position as particles from the template next door. Overlapping particles are combined into one particle, with a mass equal to the combined mass of the two original particles. Away from the boundary, each face particle will overlap with one other face particle, each edge particle will overlap with three other edge particles, and each vertex particle will overlap with seven other vertex particles. Therefore, the mass of each face particle in the template is one half of the mass of the dark matter particle in the final particle load, whilst edge and vertex particles in the template have masses of one quarter and one eighth of the final particle mass respectively. The effective total number of dark matter particles per template is thus given by $6/2 + 12/4 + 8/8 = 7$. Once the Lagrangian region has been populated with copies of the template, almost all dark matter particles will have the same mass, expect for particles at the boundary, which will have some fraction of modal dark matter mass. These fractional masses at the edge of the Lagrangian region ensure uniform density and gravitational stability.

3.2.3 Running the simulation

The simulation was performed using the EAGLE code with the subgrid parameters adopted from the REFERENCE model described in §1.5.4. Halos and subhalos were identified using the friends-of-friends and SUBFIND algorithms respectively (see §1.5.4 for details). The cosmological parameters for the simulation were taken from the Planck collaboration (Planck Collaboration et al., 2016), and are listed in Table 3.1. The simulation has 29 snapshots between redshift $z = 20$ and the present day, logarithmically spaced in scale factor. We have also stored 50 snipshots between redshift $z = 0.5$ and the present day, each containing basic particle properties such

Cosmological parameter	Value
Ω_m	0.307
Ω_Λ	0.693
Ω_b	0.04825
$h \equiv H_0/(100 \text{ km s}^{-1} \text{ Mpc}^{-1})$	0.6777
σ_8	0.8288
n_s	0.9611
Y	0.248
l_{box} [cMpc]	100
ϵ_0 [kpc]	0.05
m_{DM} [10^4 $\text{M}_\odot$]	8.2676

Table 3.1: Cosmological and numerical parameters used in the simulation. Ω_m, Ω_Λ and Ω_b are the mean density of matter, dark energy and baryons in units of the critical density at redshift $z = 0$. H_0 is the value of the Hubble parameter at redshift $z = 0$. σ_8 is standard deviation of the linear matter distribution smoothed with a top hat filter of radius 8 h^{-1} cMpc. n_s is the index of the power law which describes the power spectrum of primordial fluctuations. Y is the primordial abundance of helium. ł$_{\text{box}}$ is the comoving side length of the simulation box. ϵ_0 is the softening length used in force calculations for high-resolution dark matter particles at redshift $z = 0$. m_{DM} is the mass of a dark matter particle in the high-resolution region of the simulation. Edge effects in the construction of the initial conditions mean that a tiny fraction of the high-resolution dark matter particles (approximately 1.5%) have masses which are a fraction of this value.

as position and velocity. We have also run a dark matter only (DMO) version of the same simulation, identical to the simulation described above, but with gas particles modelled as dark matter particles.

3.2.4 Testing the initial conditions

It is essential that the configuration of particles within the Lagrangian region is gravitationally stable if the final results of the simulation are to be trusted. We check that this is the case by evolving the unpeturbed grid of particles under gravity. The configuration is indeed stable and no artificial structures form.

It is also important to identify any halos in the high-resolution region of the simulation which may be contaminated by low-resolution particles. The large-scale tidal forces are modelled using different particle species to the high-resolution region. We calculate the distance from the potential minimum of the central halo to the closest of these tidal particles at redshift $z = 0$. The distance is around 6.5 Mpc. We adopt a conservative approach, and limit our calculations to halos within a sphere of radius 5 Mpc centred on the main halo. Changing the number of dark matter particles per gas particle can potentially affect important observables in the final simulation. For example, the equipartition of energy between particle species depends on the relative masses of the particles, and may influence observables like the size of small galaxies (Ludlow et al., 2019). To study the effects of increasing the dark matter resolution for a fixed gas mass, we have have run a 25 Mpc cosmological volume with 376^3 gas particles and the same initial phases as the L0025N0376 volume described in Schaye et al. (2015), but with seven times as many dark matter particles. We refer to this run as L0025N0376x7. The mass of gas particles in these two simulation are the same, but our version has seven times as many dark matter particles, giving it comparable dark matter resolution to the L0025N0752 volume.

We check several key properties, the first of which is the mass function of halos and galaxies. Here we take the mass of a galaxy to be the mass of all star particles belonging to the most massive subgroup in each friends-of-friends group. These properties are shown in Fig. 3.2. The mass function of galaxies is almost unchanged between the versions of the simulation which have the same number of gas particles but different numbers of dark matter particles. The effect of increasing the resolution of gas particles has a much more significant impact on the abundance of both smaller and larger galaxies. The L0025N0376x7 also does an excellent job of reproducing the halo mass function at masses below the resolution limit of the L0025N0376 simulation. In general, if the difference between the blue and orange lines is bigger than the difference between either blue-green or orange-green, we conclude that the effects of increasing the gas resolution have a bigger impact on results than changing

the dark matter-gas mass ratio.

We also test the effect of differing species resolution on the internal structure of halos. We match between simulations by mass and position. Specifically, the masses of a potential matched pair must be within a factor of five, and the first halo must lie within the virial radius of the other halo and vice versa. Each halo in the L0025N0376 simulation has a corresponding matched halo in the L0025N0752 and L00N0376x7 simulations. We calculate the density of dark matter, gas, and stars as a function of radius in each halo. For each species, we then calculate the ratio of density in the L0025N0752 and L0025N0376x7 to the density in L0025N0376 simulation. We perform this calculation for the 200 most massive halos in each simulation. The results are shown in Fig. 3.3.

Outside of the Power radius (Power et al., 2003), all three versions of the simulations display excellent agreement in the measured dark matter density profiles. At distances of less than 5 kpc from the centre of the halo, the density of dark matter in the L0025N0376x7 simulation is significantly lower than the simulations which have a standard gas to dark matter particle mass ratio. This result is not unexpected. Ludlow et al. (2019) have shown that the equipartition of energy between multiple species of different-mass particles causes the heavier species to sink artificially towards the centre of the halo. In the case of the L0025N0376 simulation, the dark matter particles are around five times heavier than the star particles, which causes an artificial increase in the density of dark matter at the centre of the halo.

The second panel of Fig. 3.3 shows that beyond the Power radius, where energy equipartition can affect the distribution of particles, the density of gas is generally well reproduced, albeit with considerable scatter. The same cannot be said for the L00N0752 simulation, where the effect of increasing gas resolution has a pronounced effect on the distribution of gas in galaxies. It is clear that the total mass of gas in galaxies is not conserved, most likely as a result of resolution effects in modelling the inflow and outflow of gas. The primary point here is that the uncertainties in the modelling of baryonic effects are significantly larger than variations introduced

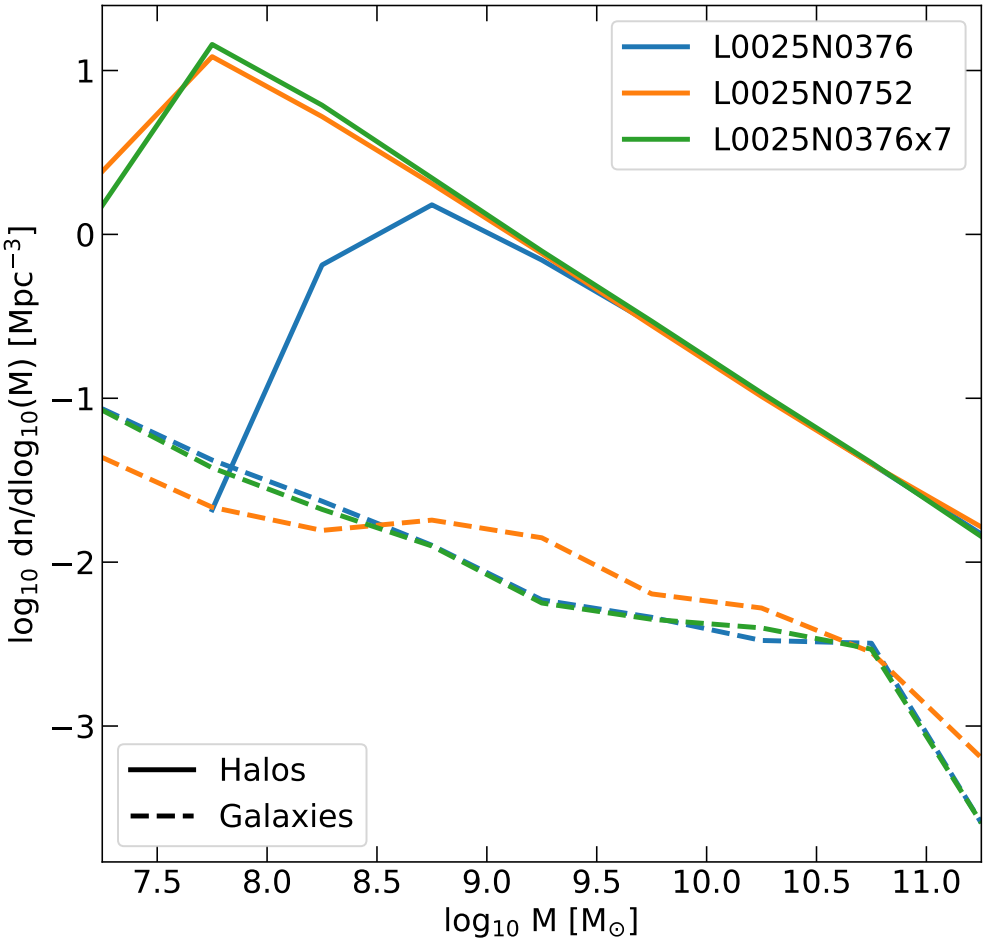

Figure 3.2: The mass function of halos (solid lines) and galaxies (dashed lines) in three realisations of the EAGLE 25 Mpc simulation. The blue lines show the halo and galaxy mass functions at standard EAGLE resolution. The orange lines show the effect of increasing the resolution of both gas and dark matter in the simulation. The green lines show the effect of increasing the resolution of dark matter whilst holding the gas resolution constant, as described in §3.2.2.

by altering the ratio of the mass of dark matter and gas particles.

3.2.5 The finished simulation

A visualisation of the high-resolution region of the simulation is shown in Fig. 3.4. The brightness of each pixel in the image is proportional to the logarithm of the projected density of matter, in a cube of side length 10 Mpc. The projected density of gas in the simulation is encoded in the hue of each pixel. Fig. 3.4 shows that the main halo in our simulation sits at the centre of three large filaments. The inset panels in Fig. 3.4 demonstrate the large dynamic range of the simulation, with the volume of the cube shown in the pink square being a millionth of the volume shown in the main figure. In addition to excellent resolution of the central halo, our simulation also resolves the internal structure of the filaments of the cosmic web, including strands of filaments which are almost entirely devoid of baryonic matter. The region simulated at high-resolution is unusually large for a zoom simulation. The region is approximately spherical, with a radius of around 7 Mpc at redshift $z = 0$. This is approximately 14 times the virial radius of the main halo. For comparison, the high-resolution region in the Auriga suite of zoom simulations (Grand et al., 2016) is approximately 4-5 times the virial radius of the main halo (or around 1 Mpc in absolute terms). The largest halo in the high-resolution region (which we will hereafter refer to as the main halo) has a virial mass of $10^{13.14}$ $M_\odot$ and a virial radius of 506 kpc at redshift $z = 0$. This halo contains $10^{8.3}$ particles (as identified using the friends-of-friends algorithm). In the high-resolution region there are 57 halos with at least one million particles. We list some basic properties of the most halos in Table 3.2.

Running this hydrodynamical version of this simulation required around 1.5 million CPU hours, on 512 cores.

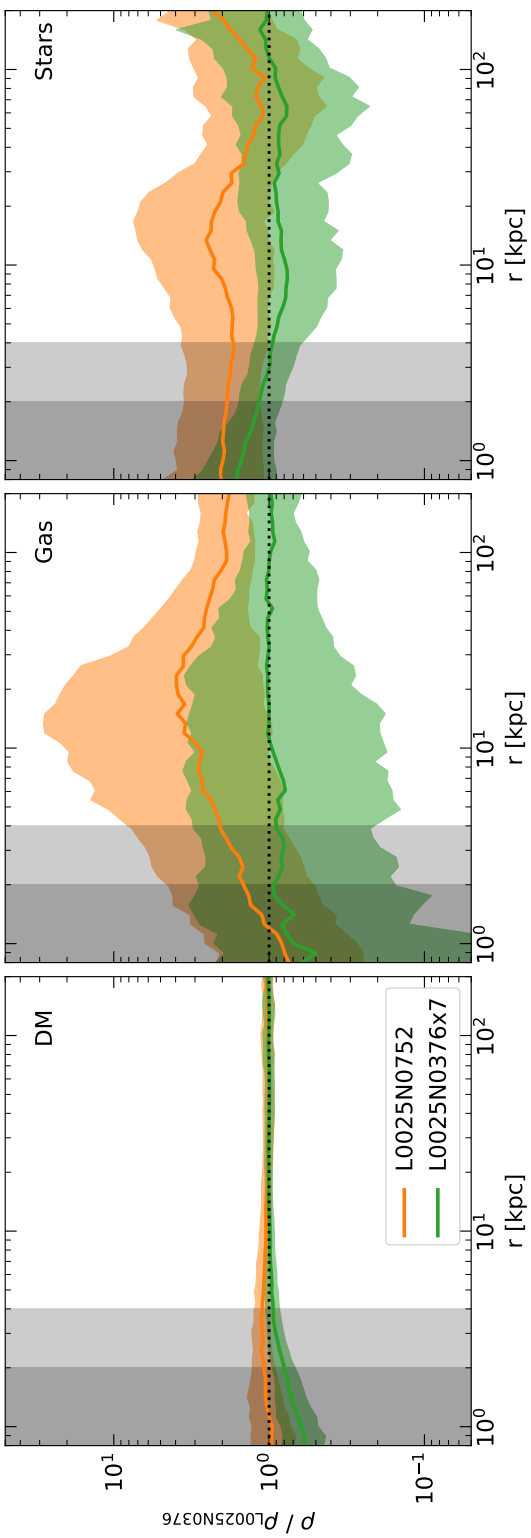

Figure 3.3: The ratio of the density of dark matter/gas/stars in the L0025N0752 (orange lines) and L0025N376x7 (green lines) simulations to the density of dark matter/gas/stars in the L0025N0376 simulation. The sample contains 200 halos matched between simulations. Solid lines show the median ratio as a function of radius for each species. Shaded regions indicate the 68% scatter. The light grey shaded region shows the approximate value of the Power radius (Power et al., 2003) for the L0025N0376 simulation, whilst the dark grey region shows the approximate Power radius for the L0025N0752 and L0025N0376x7 simulations.

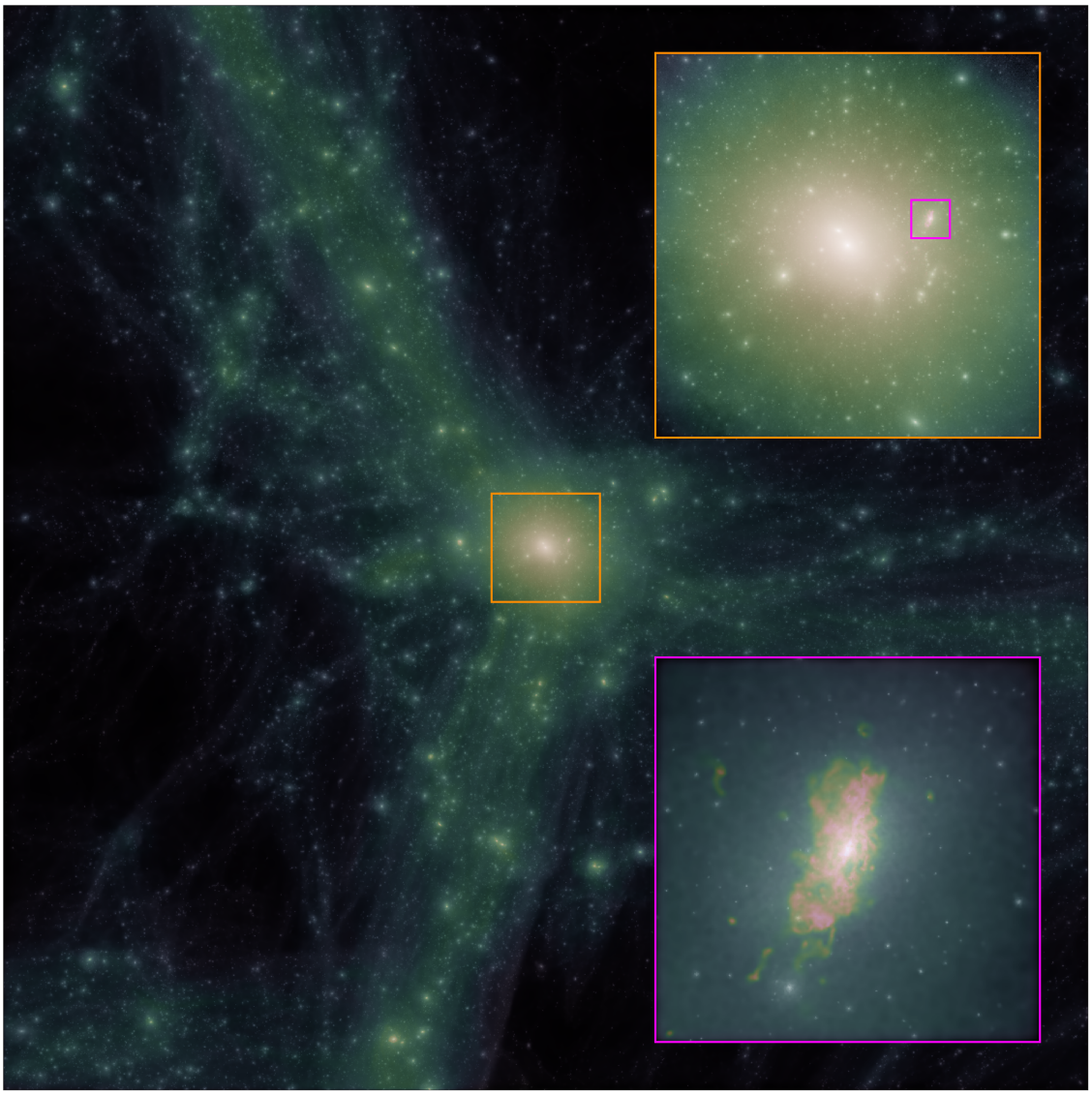

Figure 3.4: Projected density of matter in a cube of side length 10 Mpc, centred on the most massive halo in the high-resolution region of the simulation. The brightness of each pixel is proportional to the logarithm of the density of matter, and the hue encodes the density of gas. The orange inset shows a zoom into the largest halo, with a side length of 1 Mpc, and the pink inset shows a zoom into the subhalo with the greatest baryonic mass in the main halo, with a side length of 100 kpc. The main image contains approximately 500 million particles, whilst the image in the pink inset was created using approximately 1.8 million particles.

Halo	M_{200} [$M_\odot$]	r_{200} [kpc]	N_{sub}	M_{gal} [$M_\odot$]
1	$10^{13.14}$	506.2	22239	$10^{10.98}$
12	$10^{11.52}$	145.4	553	$10^{10.18}$
17	$10^{11.36}$	128.7	325	$10^{9.90}$
19	$10^{11.34}$	126.9	544	$10^{9.72}$
33	$10^{11.07}$	102.9	218	$10^{9.42}$

Table 3.2: Properties of the five largest halos in the high-resolution region of simulation volume at redshift $z = 0$. The value in the first column refers to the position of each halo in the friends-of-friends catalogue. N_{sub} is the number of subhalos identified by the SUBFIND algorithm, with a mass greater than $10^{6.5}$ $M_\odot$, inside r_{200}. M_{gal} is the total mass of all gas and star particles within 30 kpc from the centre of the halo.

3.3 The halo mass function

The majority of the lensing signal measured in the distortion of Einstein rings is produced not by substructure within the lensing halo, but by field halos in the space between the lensing galaxy and the observer. Li et al. (2017) provides an estimate for the number density of field halos along the line of sight by integrating the Sheth-Tormen mass function (Sheth & Tormen, 1999) in the volume of the light cone between the observer and the lensing halo. Li et al. (2017) extrapolated the Sheth-Tormen mass function to much lower halo masses than were used to calibrate it. In this section, we use our simulation to study the mass function of field halos, with the goal of studying whether or not the Sheth-Tormen mass function is suitable for such calculations.

3.3.1 The mass of a halo

There is no single way to define the mass of a halo in cosmological simulations. A number of definitions are widely used in the analysis of simulations, but here we focus on two: i) the friends-of-friends (FOF) mass of a halo, ii) M_{200}.

The FOF mass of a halo is simply the sum of the masses of all particles which are identified as belonging to a halo using the FOF algorithm (Davis et al., 1985).

This method is clearly defined in an algorithmic sense, and depends on a single free parameter, the linking length. This definition is also independent of cosmology.
The M_{200} mass of a halo is defined as the total mass contained inside a sphere in which the mean density of matter is 200 times the critical density of the universe, centred on the particle with the lowest potential in the FOF group. The original motivation for the use of the number 200 stem from the spherical collapse model, and considerations around the radius within which matter is virialised (in an $\Omega_m = 1$ universe). Here we are only concerned with how the choice of mass definition affects the measured halo mass function.

In general, the FOF mass and the M_{200} mass agree to within 10-20%. However, a significant fraction of halos identified by the FOF algorithm have an M_{200} mass of zero. This occurs when there exists no radius inside which the mean enclosed density of a set of FOF particles meets the density threshold required to define M_{200}. Such halos are ubiquitous in mass ranges where halos are resolved with fewer than 1000 particles, and can account for almost 30% of halos in simulations.
Furthermore, the frequency of such occurrences is a function of the simulation particle mass. For example in the Eagle 100 Mpc DMO simulation volume, around 10% of objects identified with the FOF algorithm have an M_{200} mass of 0. This figure rises to around 15% when the particle mass is an order of magnitude smaller. In the simulation presented in this chapter, where the simulation particle mass is two orders of magnitude smaller than the the Eagle 100 Mpc simulation, around 30% of objects identified with the FOF algorithm do have zero M_{200} mass. We find a similar figure when comparing with the Coco simulation, which has a similar particle mass to our simulation.
As an example of this phenomenon, we compare two halos which have the same number of particles in their FOF group, but one of the halos has an M_{200} of zero. These halos are shown in Fig. 3.5. The halo with an M_{200} mass of zero is clearly an artifact of the FOF algorithm, and should not be considered as a halo for the purposes of calculating the halo mass function. Tinker et al. (2008) argue strongly

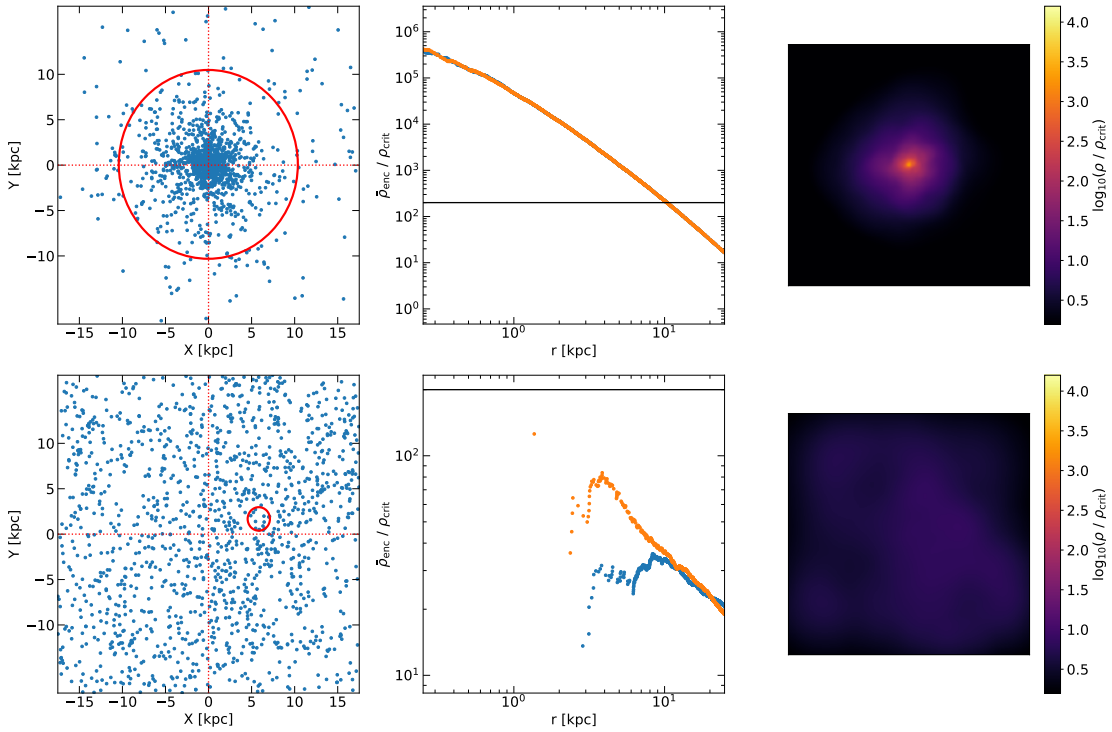

Figure 3.5: Comparison of two halos identified using the FOF algorithm. Both halos have an identical number of particles in their FOF group (1453), however one of the halos has an M_{200} mass of zero (bottom row).
Panels in the left hand column show particles associated to each halo. Dotted red lines show the centre of the halo as identified using the FOF algorithm. The red circle is centred on centre of the halo calculated using the shrinking spheres method, and has a radius equal to the calculated r_{200}.
Panels in the central column show the mean enclosed density as a function of radius, centred on either the FOF centre (blue points), or the shrinking spheres centre (orange points). The horizontal black line indicates the threshold density used in the definition of M_{200}.
Panels in the right hand column show the smoothed projected density of particles belonging to the FOF group.

in favour of using a spherical overdensity method for measuring the mass of a halo, as cluster observables are more strongly correlated with spherical overdensity masses. Furthermore, comparing the halo mass function computed in simulations using FOF masses with observation requires extensive calibration, which depends on cosmology, redshift and mass. Since FOF mass cannot be measured observationally, this calibration would have to be justified purely on theoretical grounds. This argument, coupled with the tendency of the FOF algorithm to identify diffuse sets of particles as halos, which may instead be structures such as sheets, motivates us to use M_{200} as the mass of a halo.

Analytic halo mass functions such as the Sheth-Tormen mass function show good agreement with simulations where halo masses are calculated using the FOF algorithm(Hellwing et al., 2016; Springel et al., 2005). Therefore, it will be useful to compare these two definitions of mass. Fig. 3.6 shows the relationship between the FOF mass and the M_{200} mass of halos in two DMO simulations; the Eagle 100 Mpc volume (shown in blue) and the DMO version of our new simulation (shown in orange). The difference between the two mass definitions clearly depends not just on the mass of the halo being resolved, but also on the mass of the simulation particle. In our simulation, the mass of a halo calculated using the FOF algorithm is around 10% greater than its M_{200} mass.

Warren et al. (2006) have previously highlighted systematic problems with the determination of halo masses using the FOF algorithm, however they offer only a basic correction. A more detailed correction was derived by More et al. (2011), however this correction still assumes that the set of particles identified by the FOF algorithm represents a genuine halo. This systematic difference in mass definitions affects the amplitude of the halo mass function but not the slope.

The lower panel of Fig 3.6 shows the fraction of halos which our halo-finder reports as having a M_{200} mass of zero, as a function of the FOF mass. In the simulation with a smaller particle mass, the proportion is greater for both the total number of halos and the proportion of halos at a fixed particle number. For example, the

probabilities that a FOF halo with 100 particles will be assigned a M_{200} mass of zero are around 10% and 17% in simulations with particle masses of 10^7 and 10^5 $M_\odot$ respectively. We define the effective resolution limit for field halos in our simulation as the mass where at least 10% of halos identified with FOF have an M_{200} mass of zero. For our simulation, this is approximately $10^{7.2}$ $M_\odot$.

3.3.2 The effect of baryonic physics on the halo mass function

The majority of the lensing signal in the distortion of strong lensing arcs is sourced by halos between the source galaxy and the observer. It is computationally difficult to simulate cosmological volumes on the scale of hundreds of megaparsecs with sufficient resolution to characterise the distribution of the low-mass halos of interest for tests of the CDM model. As such, it is necessary to use an analytic prescription for the abundance of field halos when calculating the expected lensing signal.

Li et al. (2017) used the analytic Sheth-Tormen mass function to predict the number of halos lying between the source galaxy and the observer (so-called interlopers). Hellwing et al. (2016) used the DMO zoom simulation Coco to measure the abundance of halos with masses greater than $10^{6.5}$ $M_\odot$. They found that the measured halo mass function at redshift $z = 0$ in their simulation is well fit by the Sheth-Tormen model for halos more massive than 10^9 $M_\odot$, and that the Sheth-Tormen model underpredicts the abundance of 10^8 $M_\odot$ halos in their simulation by around 10%.

Our simulation contains a large enough field volume to allow us to study the abundance of the low-mass halos important for lensing. Fig. 3.7 shows the measured halo mass function in both the hydrodynamical and DMO versions of our simulation at redshift $z = 0$. We find that the mass functions in both versions of the simulation are well fit by a power law, with slopes of -0.89 ± 0.01 and -0.87 ± 0.01 for the hydrodynamical and DMO versions respectively. The amplitude of the halo mass function is greater at all mass in the DMO simulation than in the hydrodynamical

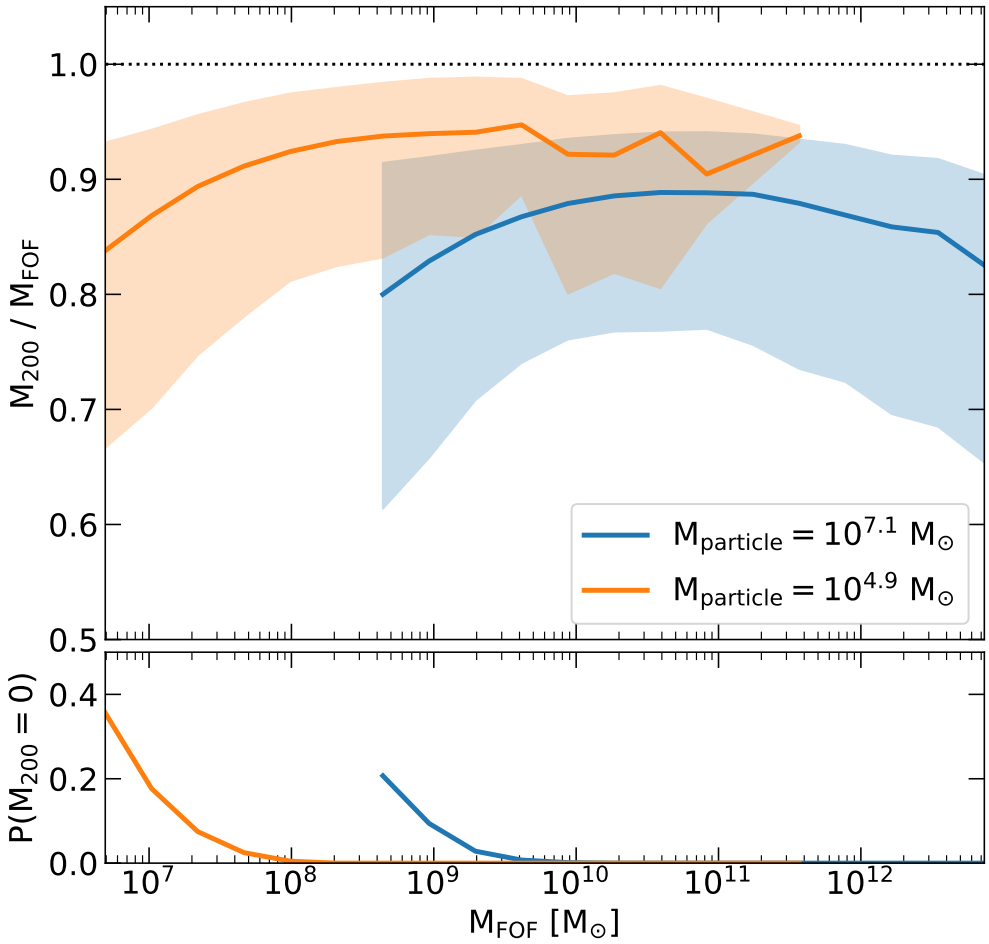

Figure 3.6: Top panel: The relationship between the FOF mass and the M_{200} mass of halos in two DMO simulations with different dark matter particle masses. Blue lines represent halos taken from the EAGLE 100 Mpc simulation, whilst orange lines represent halos taken from the high resolution region of the simulation presented earlier in this chapter. Solid lines show the median relation between the two mass measures, and shaded regions indicate 68% scatter. We only consider halos with a nonzero value of M_{200}. Bottom panel: The fraction of halos which have an a reported M_{200} mass of zero, as a function of FOF mass.

simulation. This is another example of the effect discussed in § 2.4.1, where the inability of a DMO halo to lose gas during reionisation leads to an artificially large mass (by around 25%) at the present day. Reducing the mass of all halos in the DMO simulation yields a mass function in excellent agreement with the hydrodynamical version of the simulation, showing that the baryonic physics included in the hydrodynamical simulation does not cause a reduction in the abundance of field halos. This null result is important for lensing tests of the CDM paradigm, as the abundance of field halos is not subject to any of the uncertainties associated with implementing baryonic physics in cosmological simulations.

We find that the Sheth Tormen model overpredicts the abundance of halos less massive than 10^9 $M_\odot$, by as much as 30% for halos close to the resolution limit of our simulation. The slope of the mass function predicted by the Sheth Tormen model is steeper than the measured slope in our simulations, with a slope of -0.92, compared with -0.89 for the hydrodynamical version of our simulation.

3.4 Halo environments

The high resolution of our simulation allows us to study the effect of environment on the properties of field halos. In this section we will examine the relative abundance of halos in different environments, as well as the effect of environment on the internal structure of halos, and how environmental factors determine the probability of a halo hosting a galaxy.

We use the NEXUS code (Cautun et al., 2013) to classify halo environments. The NEXUS code divides space into a cubic grid, and classifies each cell in the grid as being either a void, a sheet, a filament, or a node. The algorithm for classifying environments is as follows:

- Construct a 3D density field, f, from a simulation snapshot.
- Apply a Gaussian filter of RMS width R_n to f.

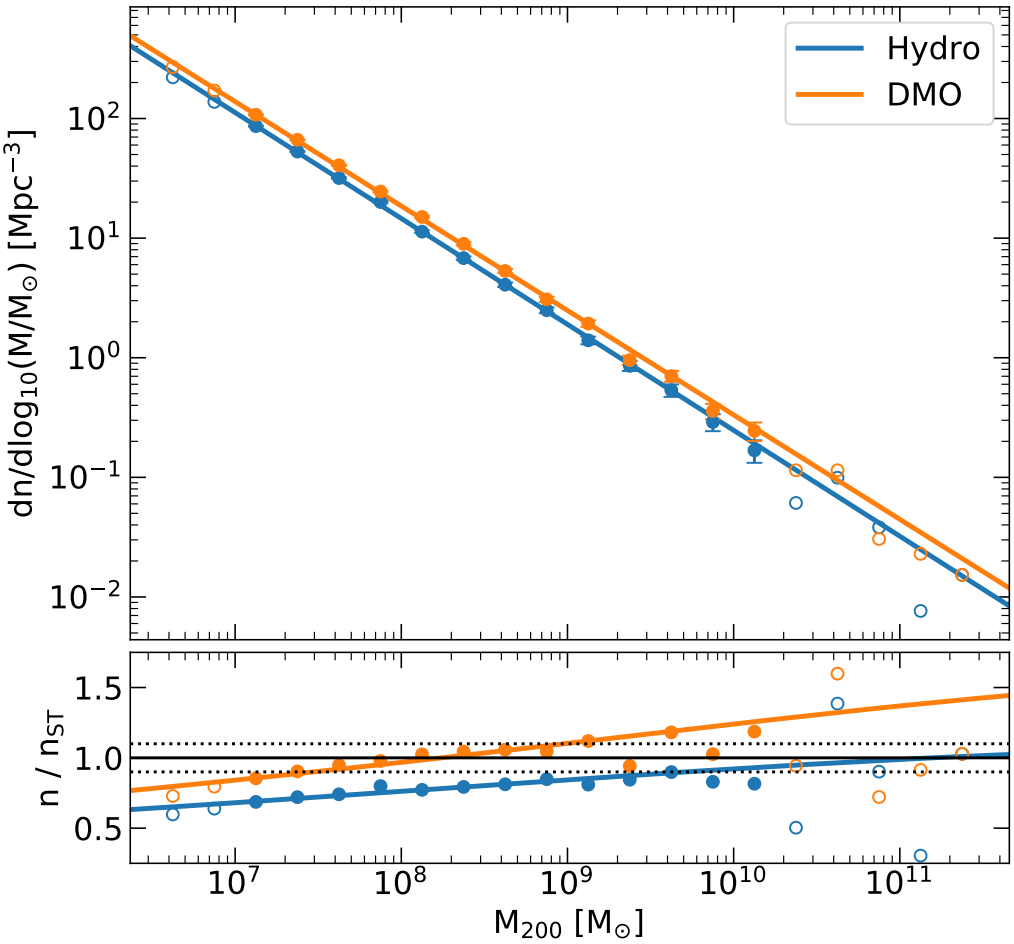

Figure 3.7: Top panel: The differential mass function of field halos in the hydrodynamical and DMO versions of our simulation, shown in blue and orange respectively. The mass function is calculated in a sphere of radius 5 Mpc centred on the potential minimum of the most massive halo in the high resolution region of the simulation. Circles show the measured halo mass function in each mass bin. The errorbars for each point show the Poisson error. Solid lines show power law fits to the halo mass function. Points shown with empty circles were not used when calculating the power law fit. Bottom panel: The ratio of the calculated halo mass function to the analytic Sheth Tormen mass function. The solid black line indicated a value of 1, whilst dotted black lines show a 10% difference level.

- Compute the eigenvalues of the Hessian matrix of the smoothed field.
- Use the eigenvalues to assign each point a void/filament/sheet/node signature.
- Repeat the previous steps over a range of smoothing scales $(R_0, R_1, ...)$ to construct the scale space representation of the field.
- Combine the results from all smoothing scales to obtain scale-free environment signatures.
- The detection threshold for nodes is set by requiring that half of the identified objects have an average density of at least $\Delta = 370\rho_{\rm crit}$ (effectively measuring whether a cluster is virialised.
- The detection thresholds for filaments and sheets are set by finding the signature value S which maximises the function $|{\rm d}M^2/{\rm dlog}S|$, where M is the mass in filaments or sheets.

3.4.1 The abundance of halos in different environments

We begin by comparing the relative abundances of halos in different environments. We compute the mass function of halos in voids, sheets, and nodes, as shown in Fig. 3.8. The slope of the mass function does not depend strongly on halo environment, which suggests that the only relevant effect is the increased density of matter in filaments relative to voids. The difference in average density is large. In the high-resolution region of our hydrodynamical simulation, the average density of dark matter in filaments is forty times greater than the average density of dark matter in voids at redshift $z = 0$.

As one would expect, the amplitude of the halo mass function depends strongly on environment. The amplitude of the halo mass function in filaments is around eight times greater than in voids. Since voids represent the majority of the volume in our simulation, the halo mass function for the whole volume has an amplitude which is two times greater than the voids-only mass function. The significant difference in

the amplitude of the mass function has implications for lensing tests of the CDM paradigm, as the majority of the signal is expected to originate from field halos. The expected abundance of such halos will depends sensitively on the the structure of the cosmic web between the source galaxy and the observer.

3.4.2 Environmental effects on the internal structure of halos

We can also study how the environment in which a halo forms affects its concentration. Here, we take the concentration of a halo to be the ratio of r_{200} to r_s, where r_s is the scale radius in the NFW density profile (Navarro et al., 1996), given by

$$\rho_{\rm NFW}(r) = \frac{\rho_s}{(r/r_s)(1+r/r_s)^2} \, . \tag{3.4.1}$$

Our procedure for fitting NFW profiles to halos is as follows:

- Using the potential minimum of the FOF group as a starting point, we find the centre of each halo using the shrinking spheres algorithm.
- We calculate r_{200} for each halo using the new halo centre.
- We calculate the density of dark matter in logarithmically spaced radial bins. For each halo, we use twice r_{200} to as outermost bin edge, and the number of bins is calculated as $2n^{1/3}$, where n is the number of particles closer to the centre than $2sr_{200}$.
- We fit an NFW profile to the logarithm of the density, using a least squares fit and assuming constant error per bin, as in Neto et al. (2007).

The calculated concentration-mass relation for halos in voids and filaments is shown in Fig. 3.9. Halos in filaments are systematically more concentrated than halos in voids, for all halo masses studied. Halos in filaments tend to be around 10-20% more concentrated than similar mass halos in voids. This result is expected, as a halo's

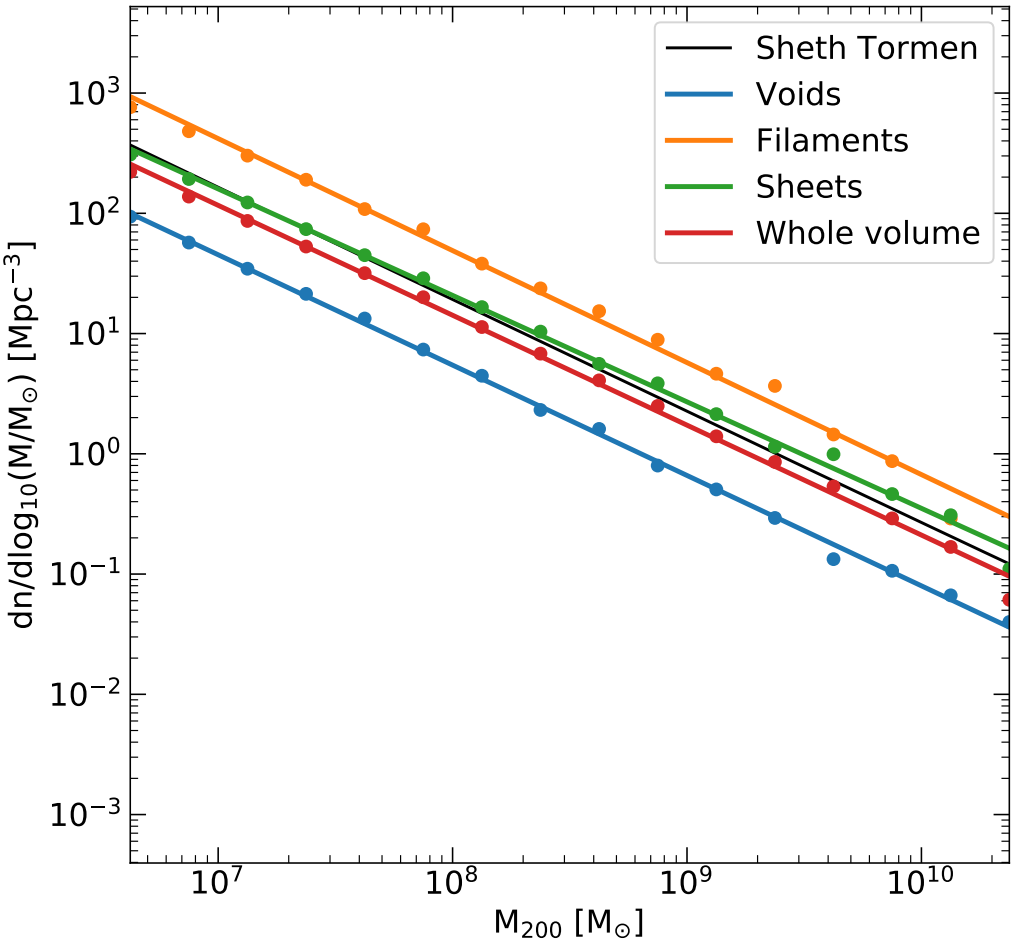

Figure 3.8: The differential halo mass function for halos in voids (blue), filaments (orange), sheets (green), and the entire volume. The environment of a halo is determined using the NEXUS algorithm. Circles show the measured mass function, whilst lines show power law fits.

concentration reflects the density of the universe at its formation time. For a fixed mass, halos tend to form earlier in filaments than voids (Hahn et al., 2007), when the universe was denser.

3.4.3 The galaxy population of different environments

Understanding the relationship between galaxies and the halos in which they form is essential for using observations of galaxy clustering to constrain cosmological parameters and models of galaxy evolution(Berlind et al., 2003). Proposed solutions to the small-scale challenges to the CDM model, such as the missing satellites problem, will require a detailed understanding of galaxy formation in small ($< 10^{11}$ $M_{\odot}$) halos if they are to prove satisfactory. The small particle mass of our simulation allows us to study the abundance of galaxies in small halos. Here we focus on the effect of environment on the likelihood of hosting a galaxy.

Fig. 3.10 shows the cumulative stellar mass function of galaxies in the high-resolution region of our simulation in three kinds of environment, voids, filaments and sheets. Here we take the stellar mass of a galaxy to be the sum of the masses of all star particles belonging to the most massive subhalo in the FOF group. The total galaxy population is dominated by galaxies in sheets. This is unsurprising as the fraction of the simulation volume identified as sheets is around 4 times larger, whilst Fig. 3.8 shows that the number density of halos in filaments is around 2–3 times as large as it is in sheets. The vast majority of the most massive galaxies in our simulation reside in either sheets or filaments. Voids occupy around 60% of the simulation volume, however the contribute only a tiny fraction of the total number of galaxies due to the very low number density of halos.

We also calculate the probability of a halo in each environment hosting a galaxy as a function of the halo's M_{200}. The results are shown in Fig. 3.11. The probability of hosting a galaxy is very low in any environment for halos in the mass range considered, but halos in filaments are the most likely to host a galaxy. This makes sense, as

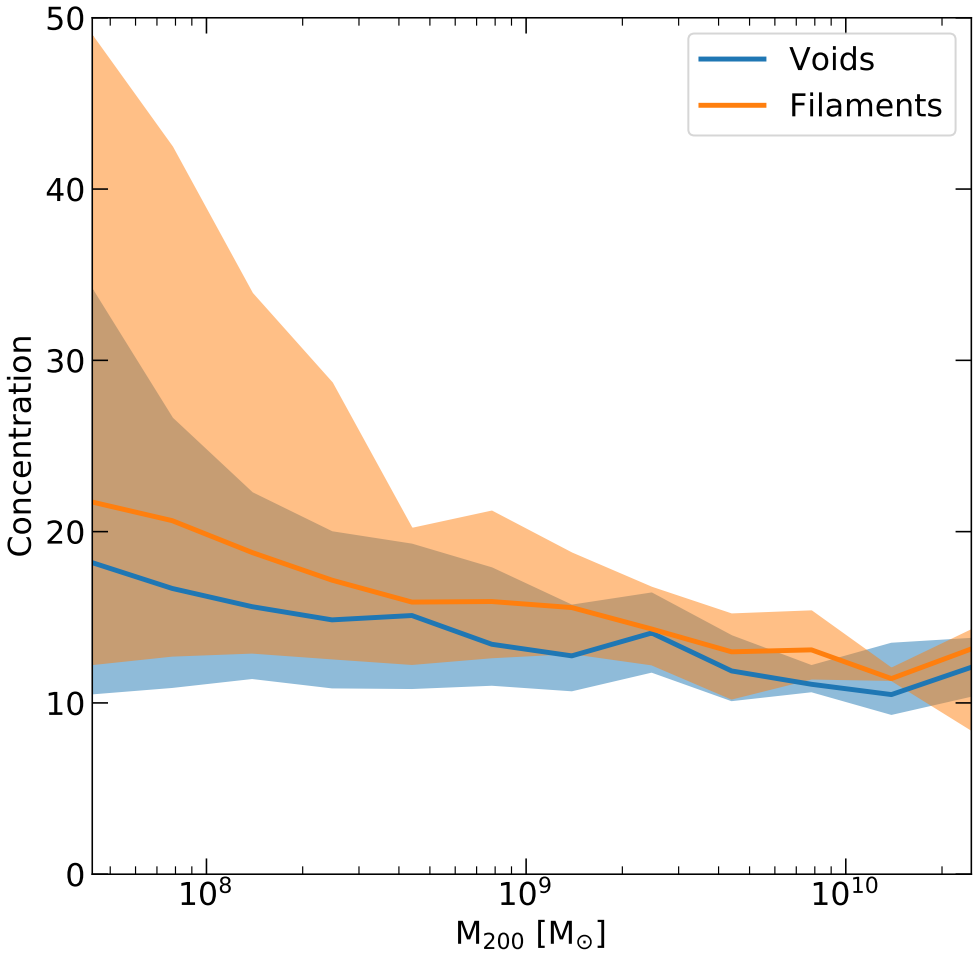

Figure 3.9: The concentration-mass relation at redshift $z = 0$ for halos in the hydrodynamical version of our simulation. Halo concentrations were determined by fitting NFW profiles to the logarithm of the dark matter radial density profiles. Solid lines show the median concentration-mass relation for halos in voids(blue) and filaments (orange). Shaded regions show the 68% scatter in the relation.

we have already seen in Fig. 3.9 that halos in filaments are more concentrated that similar-mass halos in voids. The more concentrated halos will be more more resistant to gas-loss through processes such as reionisation and stellar feedback. A greater abundance of gas then allows for the formation of more and larger galaxies.

3.5 Conclusions

Strong lensing tests of the CDM paradigm require detailed knowledge of the abundance and distribution of the small halos whose existence (or not) will allow us to discriminate between CDM and WDM models. In this chapter we have introduced a new simulation technique which allows us to increase the resolution of the dark matter component of our simulation without increasing the resolution of the hydrodynamical parts.

Using this technique we have simulated a 10^{13} $M_{\odot}$ group of galaxies, and its surrounding large scale environment, a volume of over 500 Mpc^3. The large field volume of our simulation allows us to study the abundance and properties of dark matter halos in hydrodynamical simulations. In particular, we have calculated the mass function of field halos, a vital ingredient in the aforementioned strong lensing tests, and found significant disagreement between the calculated halo mass function and the analytic model used in previous works.

We have also studied the effects of local environment on halo properties. We have focused on three key diagnostics, the relative abundance of halos in different environment, the effect of environment on the internal structure of halos, and the relative abundance of low stellar mass galaxies in different environments. We find that the abundance of halos is almost an order of magnitude greater in filaments compared to voids, and that halos in filaments are approximately 10-20% more concentrated for fixed halo mass. We find that halos in filaments are also much more likely to host galaxies, however around half the galaxies in our simulations are contained in sheets as filaments only occupy a small percentage of the total volume.

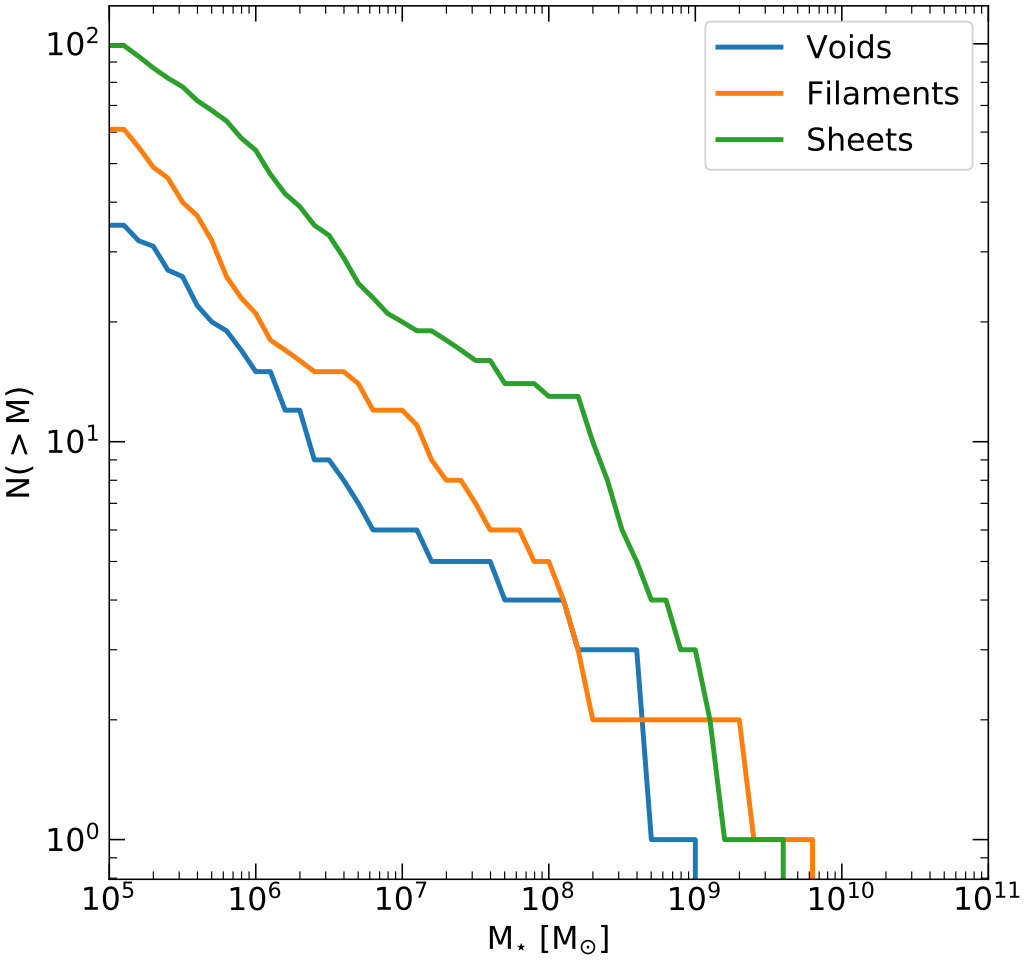

Figure 3.10: The cumulative number of galaxies in the high-resolution region of our simulation at redshift $z = 0$ according to the halo environment identified by the NEXUS algorithm.

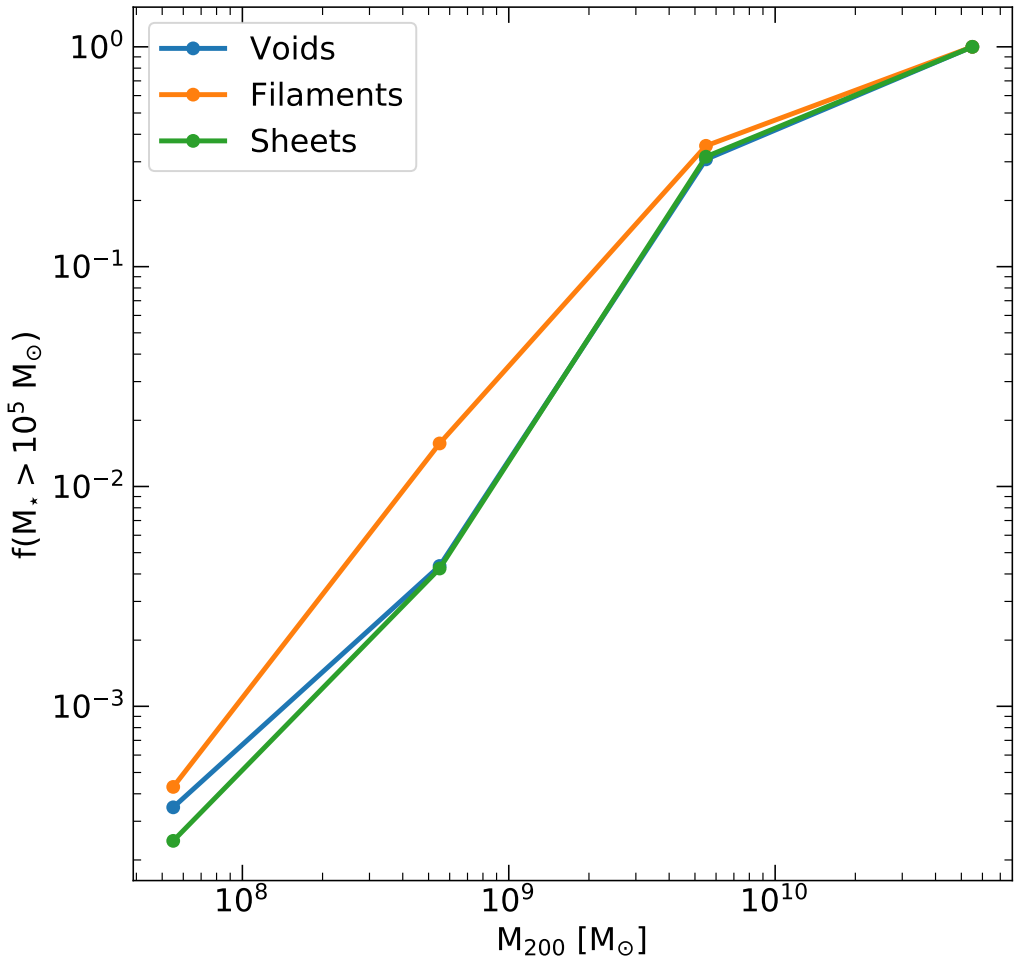

Figure 3.11: The fraction of halos, categorised by environment, which contain a stellar mass of at least 10^5 $M_\odot$ at redshift $z = 0$.

When considering halo properties, it is crucial to define the mass of the halo correctly. We have shown in this chapter that the FOF mass of a halo, which produces results in excellent agreement with the widely used Sheth Tormen mass function, is not a reliable indicator of halo mass in simulations where the particle mass is smaller than $\sim 10^7$ $M_\odot$. We have also quantified the difference between the M_{200} mass and the FOF mass of halos as a function of halo mass, however the exact nature of this relationship again depends on the mass of dark matter particle used in the simulation.

Chapter 4

The substructure of a simulated galaxy group

4.1 Introduction

UBSTRUCTURES within the lensing halo produce a significant fraction of the expected signal in strong lensing tests of the CDM model. Predictions for the subhalo contribution to the lensing signal are based on DMO simulations(Li et al., 2017; Despali et al., 2018), which cannot model the interaction between the central galaxy of the lensing halo and the halo's substructure. In this chapter we use a zoom simulation of a 10^{13} $M_{\odot}$ halo to study the effects of baryonic physics on the abundance and properties of substructure in galaxy groups.

We begin this chapter with a discussion of potential biases of the SUBFIND algorithm, which we use to identify and characterise substructure in our simulation. We then examine the main halo in our simulation, with a focus on how the inclusion of baryonic physics affects the distribution of matter near the centre of the halo. We then describe the effects of baryonic physics on subhalos, with a focus on the reduction in subhalo abundance near the centre of the halo. Since observations of gravitational lensing depend on the distribution of matter along the line of sight, we also study the variation in subhalo abundance along different projected lines of sight, and compare the degree of variation in hydrodynamical and DMO simulations.

4.2 Methods

We begin with a brief recap of the properties of our simulation introduced in the previous chapter. We performed a zoom simulation, centred on a 10^{13} $M_{\odot}$ halo selected from the EAGLE 100 Mpc volume. Using a custom set of initial conditions, where dark matter and gas particles have approximately equal masses, we simulate the evolution of this halo and its environment up to the present day. We have performed two versions of the simulation, a DMO version, and a version which uses

the EAGLE REFERENCE model. The mass of the dark matter particle in the high-resolution region of the simulation is around 8.3×10^4 $M_\odot$ in the hydrodynamical simulation.

As discussed in Chapter 2, the time between simulation snapshots is generally large compared to the the time taken for a subhalo to traverse the centre of the halo. We therefore integrate subhalo orbits between snapshots using the methodology developed in Chapter 2.

4.2.1 The Subfind algorithm

Halo substructure in our simulation is identified using the SUBFIND algorithm (Springel et al., 2001). The SUBFIND algorithm identifies subhalos by selecting a list of particles inside locally overdense regions, and then removing particles from this list based on their binding energy (see Chapter 1 for a more complete description.). The mass of a subhalo as calculated by the SUBFIND algorithm therefore depends upon the local environment of the subhalo. Near the centre of a large halo, the reported mass of a subhalo will be lower than if the same set of particles were analysed at a greater distance from the halo centre.

Here we study whether this radial-dependent property of the SUBFIND algorithm will affect our comparison of substructure properties in hydrodynamical and DMO simulations. In the simulations we study, DMO halos and subhalos tend to be around 25% more massive than their hydrodynamical counterparts. We have discussed the reasons for this in §2.4.1 and §3.3.2. It is important to know whether this systematic difference in mass, coupled with the radial bias of the SUBFIND algorithm, could lead to a reduction or enhancement of any differences between the two realisations of the simulation.

To shed light on this issue, we perform the following test. We create an idealised NFW halo using 5×10^7 particles, with $M_{200} = 10^{12}$ $M_\odot$ and a concentration of $c = 10$,

a typical value for halos of this mass[1]. We then create a smaller NFW halo, with a concentration of $c = 20$, whose particles have the same mass as the particles in the larger NFW halo. We then implant the smaller halo inside the larger, at various distances from the centre of the larger halo. For each placement of the smaller halo, we run the SUBFIND algorithm on the total set of particles. This procedure was repeated for subhalos with different numbers of particles. Individual particles in both the subhalo and main halo have velocities consistent with their NFW distribution functions, however we do not add a bulk velocity to the test subhalo. We have checked and found the difference in identified mass of stationary and fast moving subhalos is negligible compared to the size of the other effects discussed in this section.

The results of this test are shown in Fig. 4.1. We see a clear trend in the reduction of the calculated subhalo mass as the distance to the centre of the halo decreases. The size of this effect does not depend strongly on subhalo mass, except for cases in the very centre of the halo where the SUBFIND algorithm fails to even identify the existence of the smallest halo tested. Since the effect of radius on reported mass is approximately the same for subhalos with masses spanning two orders of magnitude, we do not expect that the SUBFIND algorithm to behave differently for hydrodynamical and DMO simulations, where the systematic difference between subhalos masses is only around 25%.

We also quantify this radial effect on the quantity $V_{\rm max}$, the maximum value of a subhalo's rotation curve. The radial dependence of the calculated $V_{\rm max}$ is much weaker than for the total subhalo mass. This is because the value of $V_{\rm max}$ depends on the innermost particles, whereas the outermost particles in our idealised subhalos are the ones most likely to be identified as belonging to the host halo.

A different but related effect is the increased central density of the main halo itself. The formation of galaxies at the centre of halos means that the ambient density at the

[1]We create this halo using the publicly available code PYICS, described in (Herpich et al., 2017), which is in turn based on the algorithm introduced by Kazantzidis et al. (2004).

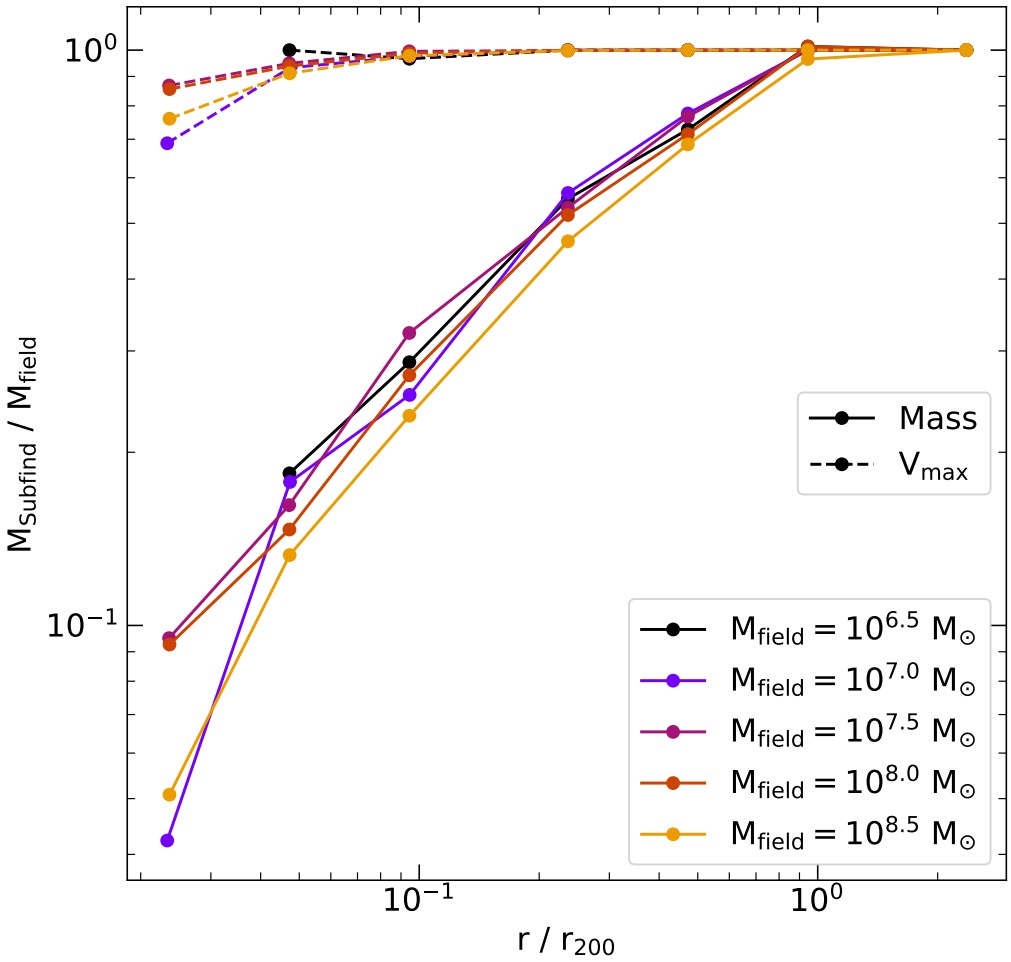

Figure 4.1: The ratio of subhalo mass/$V_{\rm max}$ to the field mass/$V_{\rm max}$ of the same set of particles, as calculated by the SUBFIND algorithm, as a function of distance from the centre of the halo. The field mass is defined as the mass reported by the SUBFIND algorithm when the subhalo is placed far from the edge of the parent halo. Solid lines show the reduction in subhalo mass, whilst dashed lines show the reduction in $V_{\rm max}$.

small radii is greater in simulations which incorporate baryonic physics. This effectively sets a higher threshold for the identification of substructure in hydrodynamical simulations. Following the method described above, we have placed subhalos of fixed mass at different radii inside two halos, one with a concentration of $c = 10$ and one with a concentration of $c = 12$. The higher concentration in the second halo mimics the increase in central density one would expect when a galaxy forms at the centre of the halo.

The results of this test are shown in Fig. 4.2. In this case, we can see that the increased central density of the more concentrated halo leads to a reduction in reported of subhalo mass of approximately 10% relative to the less concentrated halo. This effect is strongest at the centre of the halo, and rapidly becomes negligible beyond distances greater than 10% of r_{200}. The relative reduction in the reported subhalo $V_{\rm max}$ values is much smaller, once again showing that $V_{\rm max}$ is a quantity which depends much less strongly on the environment in which it is calculated.

4.3 Halo properties

In this section we describe the central halo in our simulation. We begin by calculating the density of matter in our halo, using logarithmically spaced radial bins. The density profile of the hydrodynamical halo is shown in the top panel of Fig. 4.3, with circles, triangles and stars showing the measured density in dark matter, gas and stars respectively The calculated density profiles do not include particles which belong to subhalos of the main halo. We see that stars dominate the density at the centre of the halo, but only out to a radius of around 5 kpc. The density of gas in the halo decreases very slowly with radius compared to either the stars or the dark matter. The most notable feature of the gas distribution is the high density of cold gas in the central 3 kpc.

The lower panel of Fig. 4.3 compares the density profiles of the hydrodynamical and DMO realisations of the central halo. We see the expected large increase in density

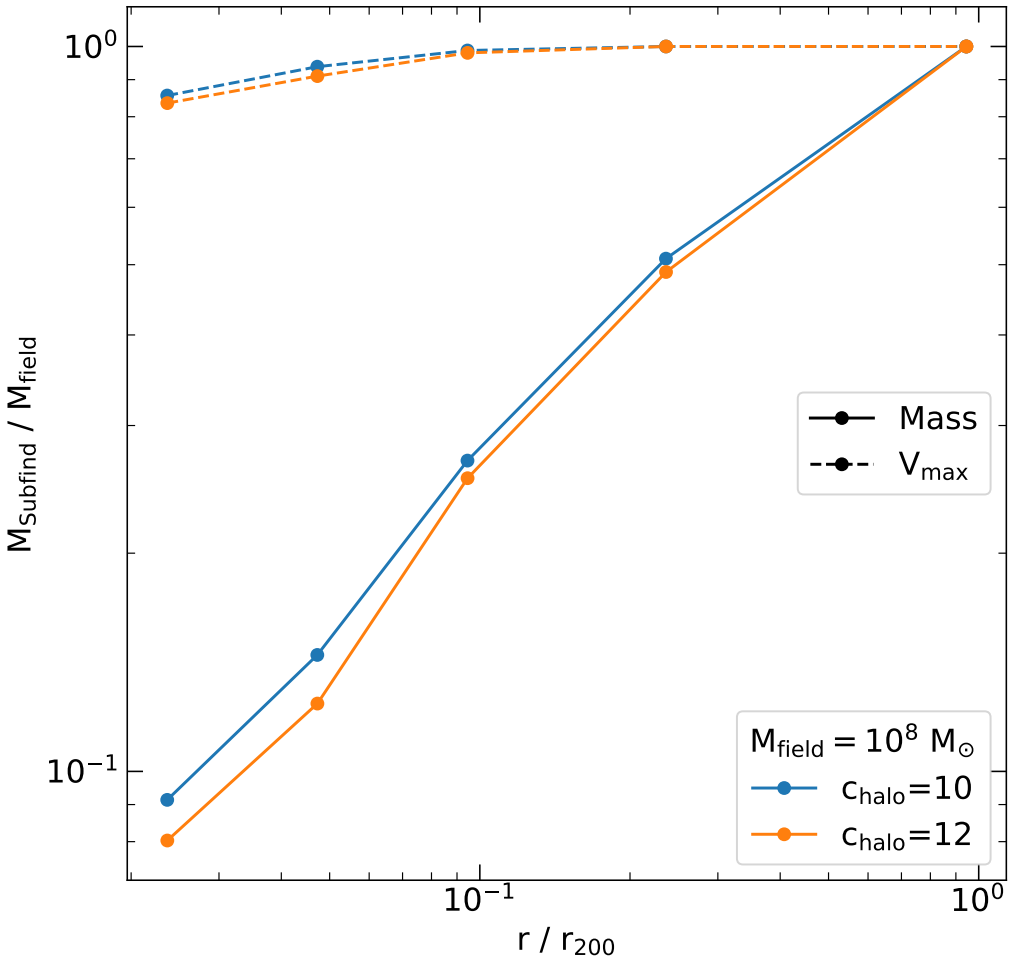

Figure 4.2: The ratio of subhalo mass/$V_{\rm max}$ to the field mass/$V_{\rm max}$ of the same set of particles, as calculated by the SUBFIND algorithm, as a function of distance from the centre of the halo. Blue and orange points show the reduction in subhalo mass/$V_{\rm max}$ in halos with concentrations $c = 10$ and $c = 12$ respectively. Solid lines show the reduction in subhalo mass, whilst dashed lines show the reduction in subhalo $V_{\rm max}$.

in the hydrodynamical version, out to distances of roughly 5 kpc. The density of matter in the hydrodynamical version is slightly lower between 20 and 200 kpc. This is the result of halo contraction in the hydrodynamical simulation, as the large increase in density at small radii is offset by a slight decrease in density for large radii, whilst leaving the total mass of the halo unchanged.

We study the distribution of dark matter in our halo more closely in Fig. 4.4. The density of dark matter in both versions of the simulation is well fit by an NFW profile, for radii greater than around 5 kpc. The effects of adiabatic contraction are visible on the dark matter in the hydrodynamical simulation, as distance from the halo centre decreases, the density of dark matter increases more rapidly in the hydrodynamical version of the simulation. The concentration of the halo, given by r_{200}/r_s, is almost identical in the two versions of the simulation, showing that any contraction effects are limited to the central few kpc.

The enhanced destruction of subhalos in simulations which include baryonic physics is usually attributed to the increased tidal forces near the centre of the halo. The gravitational potential at a distance r from the centre of the halo is given by

$$\phi(r) = -4\pi G \left[\frac{1}{r} \int_0^r r'^2 \rho(r') dr' + \int_r^\infty r' \rho(r') dr' \right] , \tag{4.3.1}$$

where $\rho(r)$ is the spherically averaged density profile. In Fig. 4.5 we show the escape velocity (as a measure of the depth of the potential well), and spherically averaged radial tidal force in both the hydrodynamical and DMO versions of our simulation. We find that the potential in the hydrodynamical version of our simulation is deeper for distances smaller than 2kpc. This is somewhat surprising, as the total density of matter at the radius is still greater in the hydrodynamical simulation. When comparing the tidal forces however (the lower panel of Fig. 4.5), we see that the tidal forces are greater in the hydrodynamical simulation out to a distance of 10 kpc, approximately the same distance at which the density of matter in the hydrodynamical and DMO simulations reaches equality.

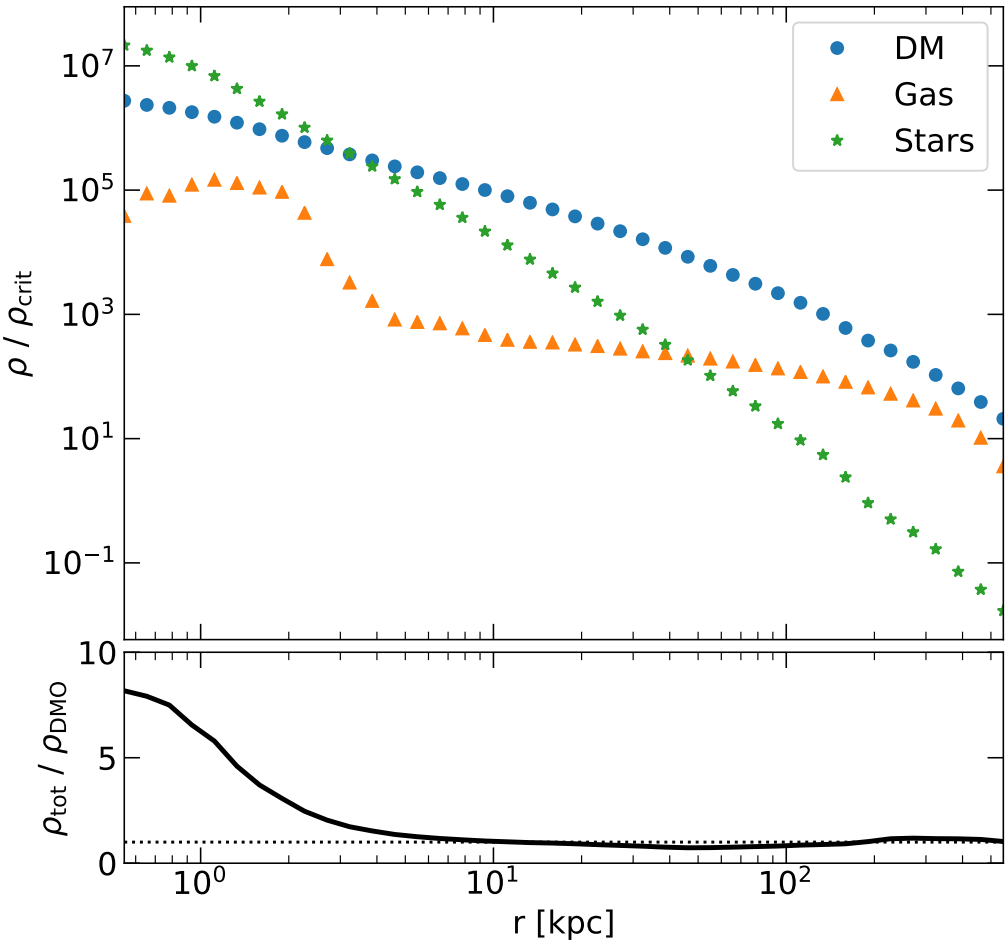

Figure 4.3: Top panel: The density of dark matter (blue circles), gas (orange triangles) and stars (green stars) as a function of distance from the centre of the halo. Densities were calculated using only particles which belong to the most massive subhalo in the FOF group. Bottom panel: the ratio of the total matter density (the sum of density of dark matter, gas and stars) to the density of matter in the DMO realisation of the halo.

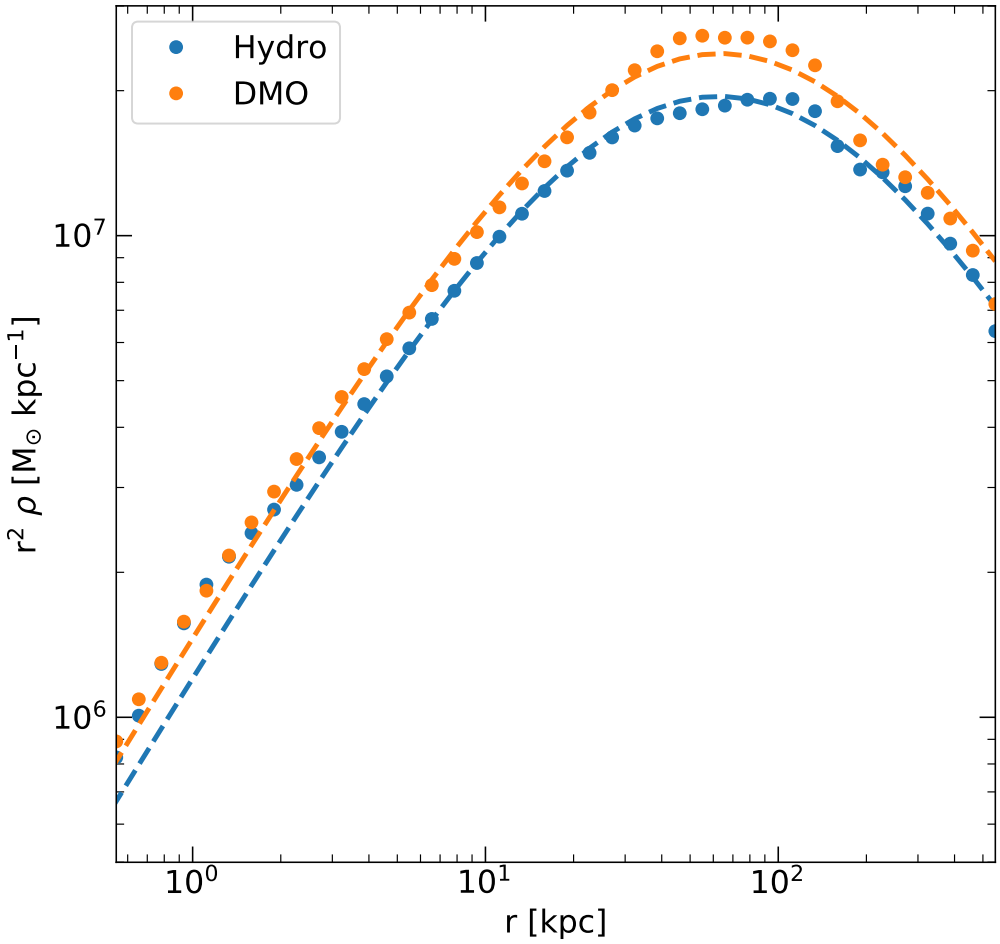

Figure 4.4: The density of dark matter (multiplied by the square of the radius) in the hydrodynamical (blue points) and DMO (orange points) versions of the simulation. Dashed lines show the best-fit NFW profiles.

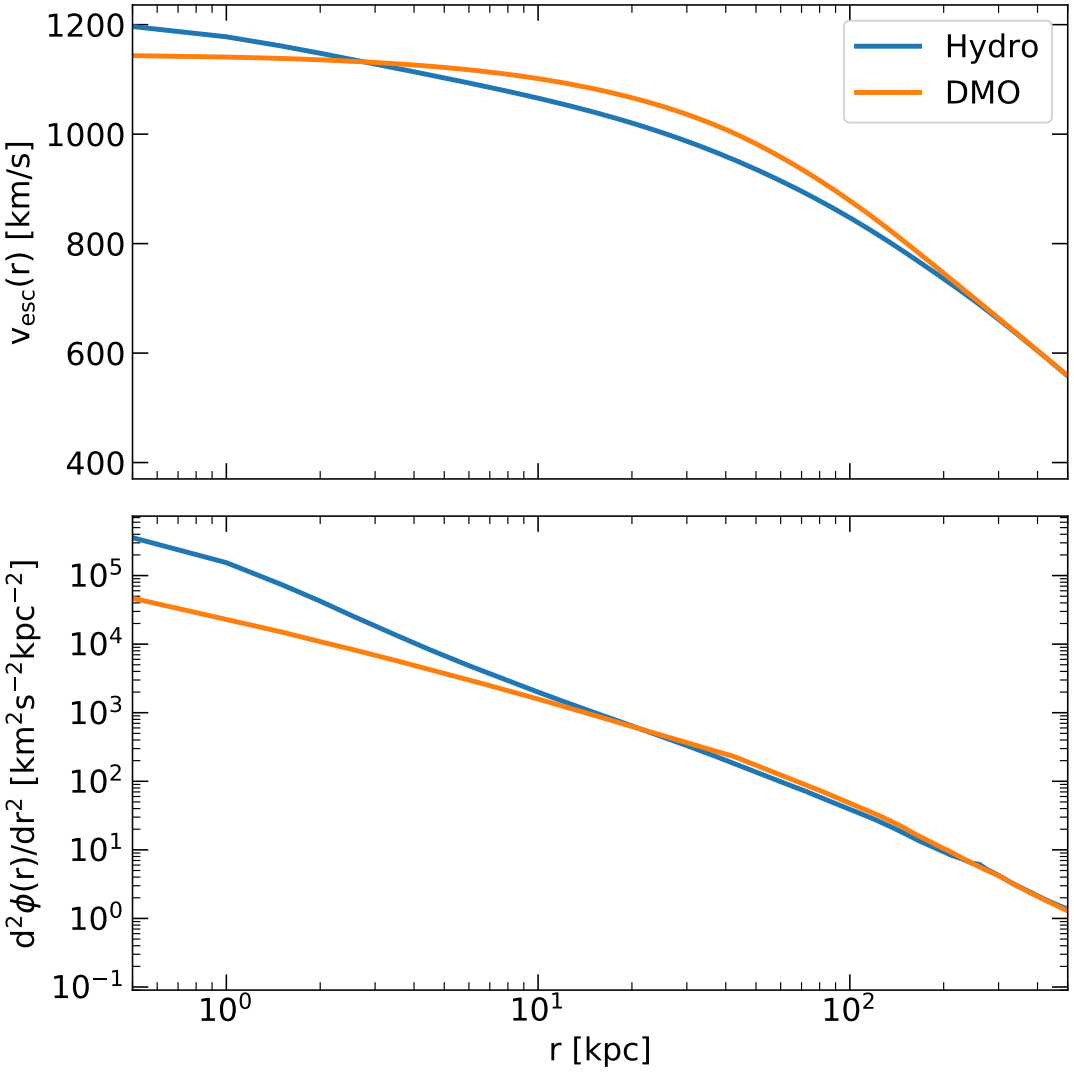

Figure 4.5: Top panel: escape velocity as a function of radius for the main halo in the hydrodynamical and DMO versions of our simulation at redshift $z = 0$. Bottom panel: The radial tidal force of the spherically averaged mass distribution of the host halo as a function of distance from the halo centre, calculated by taking the second derivative of the potential with respect to radius.

4.4 Subhalo properties

4.4.1 Subhalo abundance

In this section we describe the properties of subhalos in our simulation, with a focus on the effects of baryonic physics on subhalo properties. We begin by comparing the radial distribution of subhalos in the hydrodynamical and DMO versions of our simulation. Fig. 4.6 shows the cumulative subhalo mass function in four concentric spherical shells, centred on the potential minimum of the halo. Each panel also shows the relative reduction in subhalo abundance in that radial bin.

Inside 50 kpc (approximately 10% of r_{200}), subhalo abundance in the hydrodynamical version of our simulation is reduced by around 50% for 10^8 $M_\odot$ subhalos. This effect size is similar to the reduction in subhalo abundance observed in the APOSTLE simulations described in Chapter 2. We do not find a significant mass dependence for the reduction in substructure abundance. It is possible that some small effect may exist, however for distances smaller than 50 kpc, the time-variation in the abundance of substructure is a large enough cause of uncertainty that more definitive statements are not possible.

In the innermost spherical shell, we find that the probability of finding subhalos more massive than $\sim 2 \times 10^8$ $M_\odot$ in the DMO simulation is around 10%, whereas no objects greater than 10^8 $M_\odot$ enter the central 20 kpc over the 5 Gyr period we consider. We see a clear radial trend in the reduction in subhalo abundance; for distances greater than 100 kpc the subhalo abundance in the hydrodynamical realisation of the halo is identical to the DMO abundance, excepting effect of DMO subhalos having systematically greater masses due to their inability to lose mass at high redshifts to processes such as reionisation (see §2.4.1 for a more thorough explanation).

In the previous section, we showed that the tidal forces were greater in the hydrodynamical halo out to a radius of around 10 kpc. These enhanced tidal forces are responsible for the reduction in subhalo abundance observed inside 100 kpc. The

mismatch between the radial extent of the enhanced tidal forces and the radial extent of the measured destruction supports the interpretation we presented in Chapter 2, namely that differences between DMO and hydrodynamical subhalo populations far from the central galaxy are produced by the differing fates of subhalos on highly radial orbits. DMO subhalos have a higher probability of surviving a passage through the halo centre than their hydrodynamical counterparts.

4.4.2 Satellite galaxies

Here we examine the properties of luminous subhalos. We define a subhalo as being luminous if it contains at least one star particle. A strong theoretical understanding of the relationship between satellite galaxies and the subhalos which host them is essential for satisfactory explanations to the missing satellites and too big to fail problems (described in Chapter 1).

The leftmost panel in Fig. 4.7 shows the mass-$V_{\rm max}$ relation for all subhalos inside r_{200}. Dark subhalos are shown in blue whilst luminous subhalos are shown in orange. The mass-$V_{\rm max}$ relation has very broad scatter for subhalos less massive than 10^9 $\rm M_\odot$, however there is a clear tendency for luminous subhalos to reside at the top end of this distribution. For a given subhalo mass, only the subhalos with the deepest potential wells are likely to host a galaxy. The large scatter in the mass-$V_{\rm max}$ relation is in large part due to the stripping and disruption caused by interactions between subhalos and the host halo. It is probable that the smallest subhalos which host galaxies were much larger in the distant past, and have since undergone significant stripping.

Subhalos with a $V_{\rm max}$ smaller than around 10 km/s very rarely host a galaxy, whereas subhalos with a $V_{\rm max}$ greater than 30 km/s almost always contain a galaxy. The transition between these two values occurs over a small range of $V_{\rm max}$. Using a fixed number of star particles to define whether a subhalo contains a galaxy is clearly a resolution-dependent statement. In the central panel of Fig. 4.7, we show how the probability of a subhalo hosting a galaxy varies for a range of minimum stellar

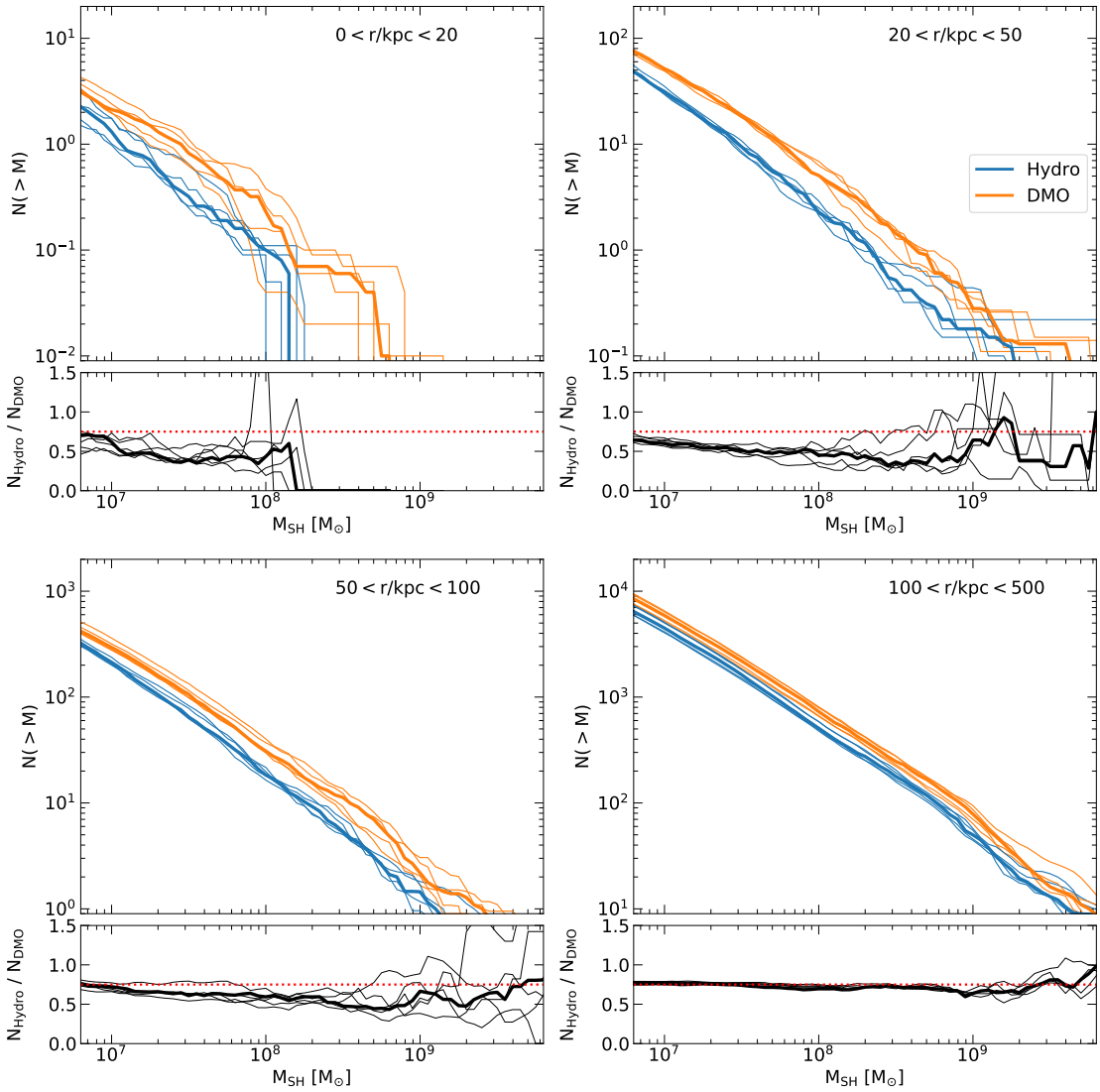

Figure 4.6: Large panels: Cumulative subhalo mass functions in concentric spherical shells centred on the potential minimum of the central halo. Thin lines show the abundance of subhalos averaged over a period of 1 Gyr. Thick lines show the abundance of subhalos averaged over the 5 Gyr period between redshift $z = 0.5$ and the present day. Small panels: Thin black lines show the ratio of the cumulative subhalo mass functions in the hydrodynamical and DMO versions of the simulation. Thick black lines show the average reduction in subhalo in subhalo abundance as a function of mass over a 5 Gyr period. Dotted red lines show the expected reduction in subhalo abundance due to global effects (as opposed to disruption or stripping) described in §2.4.1.

masses. The results are consistent with findings of the APOSTLE simulation (Sawala et al., 2016), suggesting that the properties of the host halo do not have a strong effect with regards to the onset of galaxy formation.

The right-hand panel in Fig. 4.7 shows the relationship between the $V_{\rm max}$ and stellar mass of subhalos, for all subhalos inside r_{200}. The solid red line shows the median relation between subhalo $V_{\rm max}$ and stellar mass. We note a clear upturn in the gradient of the median relation around 30 km/s. This value of 30 km/s is the approximate threshold at which all subhalos host galaxies. Fig. 4.7 implies that the gas resolution of our simulation is not sufficient to study the low-mass end of galaxy formation as even the least massive subhalos have a non-zero probability of hosting a galaxy.

4.5 Projection effects in lensing

One of the principal motivations for running this simulation was to study the effects of substructure in the distortion of strong lensing arcs, a key test of the ΛCDM paradigm. Observations of lenses are made in projection, so the variability in observations due to the angle of observation is an important component in the uncertainty of observational tests. The distribution of subhalos in the main halo of our simulation is far from spherically symmetric. The central halo in our simulation sits at the intersection of three filaments. The number density of substructures along these filaments is greater than the average over the whole halo, so an observation with a line of sight co-linear with a filament will measure a much stronger signal due to substructure than is representative of the halo.

We visualise the effect of viewing angle on the observed abundance of substructure in Fig. 4.8. We took 10^6 lines of sight distributed uniformly on the surface of a sphere[2] centred on the potential minimum of the main halo. Along each line of sight,

[2]Technically, an exactly uniform spacing of points on the surface of a sphere is impossible for all but a set of special numbers of points(Saff & Kuijlaars, 1997). Here we use the python package SEAGEN(Kegerreis et al., 2019) to distribute points on the surface of a sphere with such that the

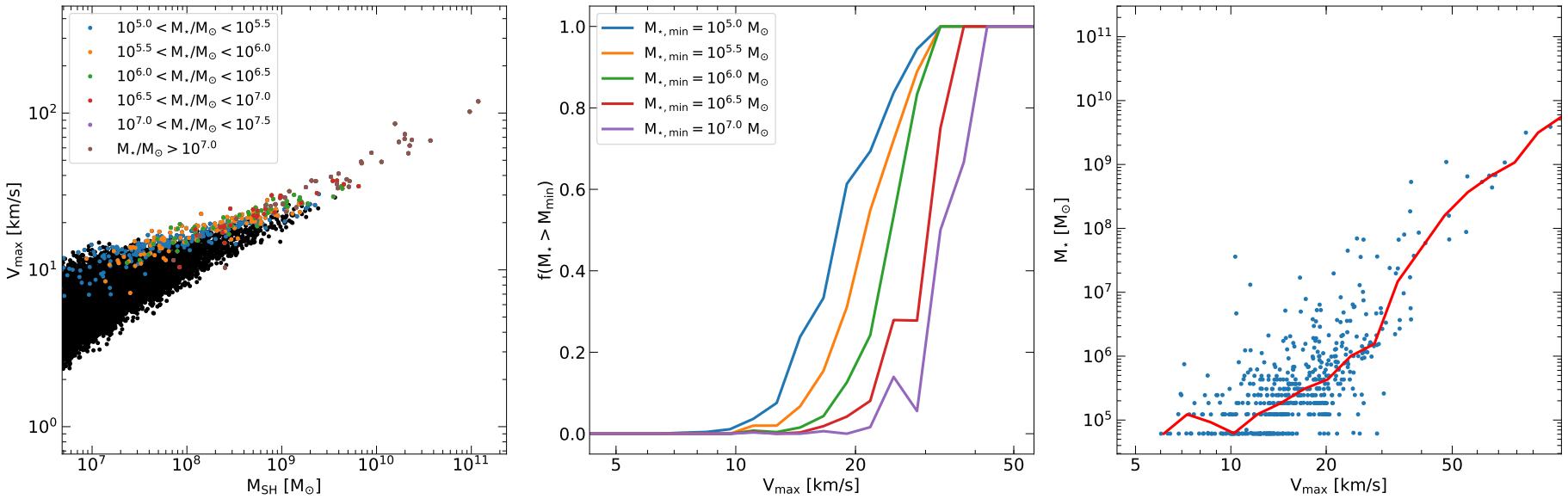

Figure 4.7: Left panel: The mass-$V_{\rm max}$ relation for subhalos inside r_{200} in the hydrodynamical version of our simulation at redshift $z = 0$. Coloured point indicate luminous subhalos, with the colour of each point indicating the stellar mass of the subhalo. Central panel: The probability of a subhalo hosting a galaxy as a function of subhalo $V_{\rm max}$ at redshift $z = 0$. Each line shows the relation for a different minimum stellar mass. Results are computed using subhalos inside r_{200}. Right panel: The relationship between stellar mass and subhalo $V_{\rm max}$ for subhalos inside r_{200} at redshift $z = 0$. Blue points show individual subhalos, whilst the solid red line shows the median relation.

we calculate the number of objects with a SUBFIND mass between 10^7–10^8 $M_\odot$, in a cylinder of radius 10 kpc and length 10 Mpc, centred on the main halo. This measurement includes the subhalos of the main halo in the simulation, but also other halos and their subhalos which fall in the projected line of sight. We show the number of observed objects along each line of sight in Fig. 4.8. The map is smoothed over a scale of one degree. We perform this calculation at redshift $z = 0.1$, as this is the redshift used for calculations in Li et al. (2017) and is a redshift at which lensing galaxies are typically observed (Bolton et al., 2006).

As one would expect, the number of objects observed depends strongly on viewing angle. Viewing angles which contain many objects are closely aligned with filaments, and will often contain 2–3 times as many objects as viewing angles which do not intersect a filament. We record the FOF group membership of objects along each line of sight. The dominant contribution to the signal originates from subhalos, as opposed to nearby field halos. We do not make a distinction between halos and subhalos, as the shape of the halo (and thus the number of subhalos along a particular line of sight), is strongly correlated with the direction of the filaments. From an observational perspective, the distinction between subhalo and nearby halo is artificial.

We compare the distribution of the number of objects along different lines of sight in the hydrodynamical and DMO versions of our simulation in Fig. 4.9. We fit a Poisson distribution to each data set, which is shown using the orange line. The mean of the hydrodynamical and DMO fits are 21 and 31 respectively. For both versions of our simulation, we see that a Poisson distribution underpredicts the number of viewing angles containing an above-average number of objects. The number of objects along a given line of sight in the hydrodynamical simulation is around 30% smaller on average. This is a combination of DMO halo mass function having a systematically greater amplitude, and the reduction in subhalo abundance in the fixed mass range due to destruction and stripping effects in the hydrodynamical simulation. The

density of points over the sphere is very close to uniform, including at the poles.

Figure 4.8: The number of halos and subhalos between 10^7–10^8 $M_\odot$ along projected lines of sight at redshift $z = 0.1$ in the hydrodynamical version of our simulation. Each line of sight is a cylinder of 10 Mpc in length and radius of 10 kpc. The map shows 10^6 lines of sight spread evenly across the surface of a sphere of radius 5 Mpc, and is smoothed on a scale of one degree. We use the equal-area Mollenweide projection.

destruction effect is smaller compared the global change in the amplitude of the halo mass function, with destruction/stripping contribution around one third of the observed reduction.

4.6 Conclusions

In this chapter we have examined how the inclusion of baryonic physics affects the abundance and properties of substructure in galaxy groups. It is important to accurately quantify these effects if strong lensing tests are to make definitive statements on the validity of the CDM model. We have used the zoom simulation introduced in Chapter 3 to quantify the effect that the inclusion of baryonic physics, in particular the presence of the central galaxy, has on the abundance and properties of subhalos.

We find that subhalo abundance is reduced by the presence of the central galaxy out to distances of roughly 100 kpc. The magnitude of this effect is consistent with the effect size reported for the Apostle simulations in Chapter 2. The radial extent of this effect is large in comparison to the extent of the galaxy. We have measured the effect of including baryonic physics on the tidal forces in the main halo, and found that there are no significant differences beyond a radius of roughly 10 kpc. This supports the conclusion presented in Chapter 2, that the differences between DMO and hydrodynamical subhalo populations far from the central galaxy originate when subhalos on radial orbits pass near the centre of the halo, and survive this passage in the DMO simulation, but are destroyed by the greater tidal forces in the hydrodynamical simulation.

We have also calculated the number of halos and subhalos in projection, by taking lines of sight through the main halo and its local environment. We have found that in both the hydrodynamical and DMO versions of the simulation, the distribution of subhalos along different lines of sight is poorly fit by a Poisson distribution. This is most likely due to filamentary accretion producing an asymmetric distribution of

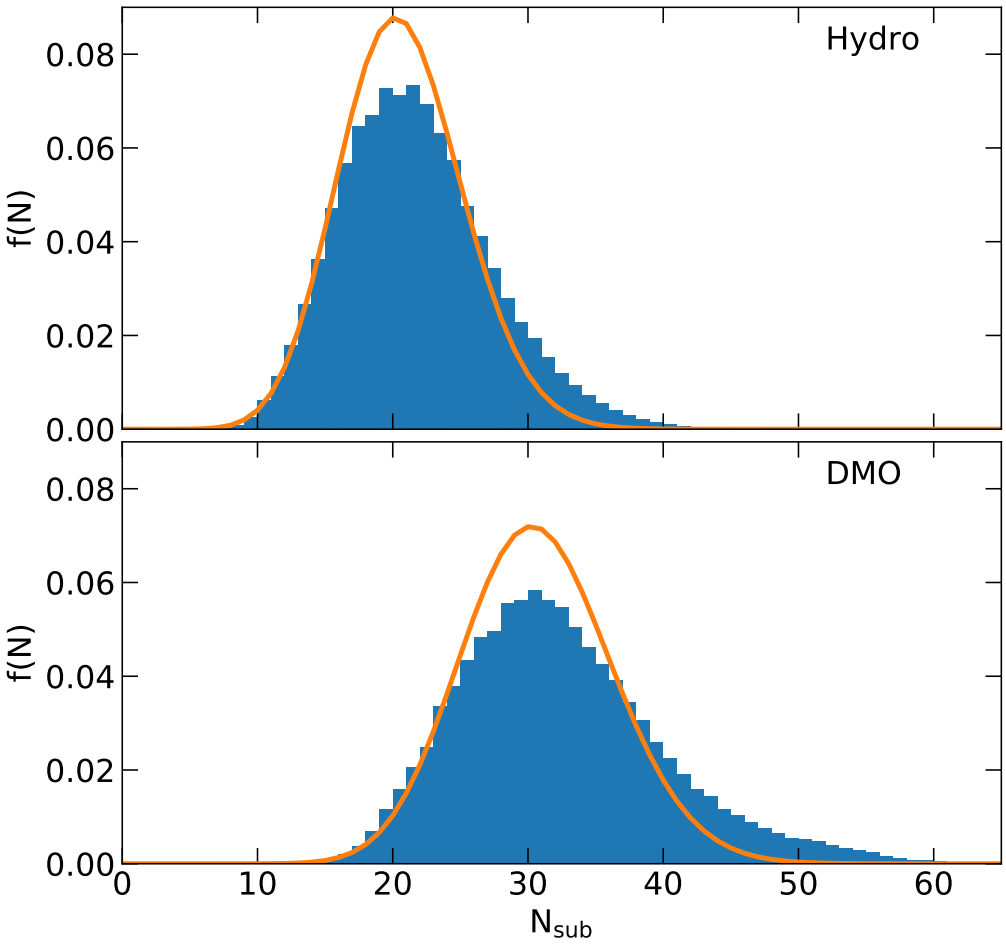

Figure 4.9: The distribution of the number of halos and subhalos with masses between between 10^7–10^8 $M_\odot$ along lines of sight projected through the centre of the main halo at redshift $z = 0.1$. Each projection is a cylinder of 10 Mpc in length and has a radius of 10 kpc. Orange lines show Poisson distributions fit to the measured distribution.

subhalos within the main halo, as well as the relatively high abundance of field halos in filaments.

The primary limitation of this investigation is the small sample size. The halo-to-halo variation in the reduction in subhalo abundance in Milky Way-mass halos encompasses the reduction observed in this halo. We are thus unable to make firm statements about the effect of halo/galaxy size on the reduction in substructure abundance. Our limited sample size also means we are unable to characterise the variation in substructure abundance between halos in the same mass range. A third limiting factor is our consideration of only one implementation of baryonic physics. Whilst we have investigated the impact of baryonic physics implementation on subhalo abundance from Milky Way-mass halos, there is no guarantee that the conclusions derived will also apply to much larger halo where the halo mass–stellar mass relation may differ significantly.

We conclude this chapter by commenting on the expected differences between the CDM and WDM models for simulations of this kind. (Lovell et al., 2016) have shown that the abundance of subhalos with a $V_{\rm max}$ of less than 10 km/s is reduced by at least a factor of five in hydrodynamical simulations of Milky Way-mass halos. In this chapter we have shown that the effect of baryonic physics on the subhalo population is significant near the centre of 10^13 $M_\odot$ halos. However, the size of these effects is small compared to the expected reduction in subhalo abundance associated with current viable WDM models. It is therefore the case that the kind of lensing tests described in this thesis have the potential to to either strongly constrain WDM models or even rule out the CDM model.

Chapter 5

Conclusions

The success enjoyed by the standard model of cosmology on large scales has not been replicated on small scales. In spite of the fact that there are not yet observations that directly contravene the CDM model, the difficulty in drawing unambiguous conclusions from observations means that whether or not the CDM model is correct remains an open question. At the heart of this problem is the inability of modern cosmological simulations to model complex baryonic processes. This complicates matters in two ways. On the one hand, we do not yet have a clear picture of how baryonic matter is influenced by the underlying dark matter distribution, and so we are unable to confidently infer the properties of dark matter in our galaxy from observations. On the other hand, an incomplete modelling of the interactions between dark matter and baryons limits our ability to form a complete picture of the expected distribution of dark matter for a given model. The aim of this thesis has been to study the effects of baryonic physics on dark matter halos and subhalos, with a specific view to testing the CDM model.

In Chapter 1 we introduced the standard cosmological model, and presented some of the challenges that this model faces on the scale of dwarf galaxies. We presented arguments suggesting that these problems may be alleviated with a better understanding of the effects of baryonic physics on dark matter halos and subhalos. We also introduced several alternative dark matter models, each of which aims to alleviate at least one of the tensions between observations and the CDM model. We concluded the chapter by introducing the one of the key tools of modern astrophysics, the cosmological simulation.

In Chapter 2 we compared two state of the art cosmological simulations of Milky Way-mass halos, Apostle and Auriga. We used these simulations to study how

changing the implementation of baryonic physics affected the substructure of Galactic halos. Compared with the dark matter-only (DMO) version of each simulation, the abundance of substructure near the centre of the halo is reduced by around 40% in the APOSTLE hydrodynamical simulations. In the AURIGA simulations the magnitude of the reduction is around twice as large. The driving factor in this large difference is the presence of more massive central galaxies in the AURIGA simulations. We also showed that the central galaxy has a strong influence on the abundance of substructure far beyond the edge of the galaxy, even beyond r_{200}. Subhalo velocities also depends strongly on the implementation of baryonic physics, with the more massive central galaxies in the AURIGA simulations producing broader radial velocity distributions and increasing the average speed of subhalos near the centre of the halo.

In Chapter 3 we introduced a new hydrodyamical zoom-in simulation of a 10^{13} $M_{\odot}$ halo and its environment, which can be used to study the impact of baryonic physics on low-mass halos and subhalos. We developed a new method for generating initial conditions, which allowed us to simulate the dark matter at a higher resolution than the gas. We showed that this new approach did not affect the properties of baryons in our simulation, aside from alleviating the numerical effects associated with energy equipartition of different-mass particle species. The finished simulation has a large field volume, which we used to study the abundance of the low-mass halos expected to dominate the signal in strong lensing tests of the CDM model. We also used the NEXUS code to study the effect of environment on the abundance and properties of field halos, and highlighted a shortcoming of the friends-of-friends algorithm commonly used to identify halos in simulations.

In Chapter 4 we studied the properties of substructure in the 10^{13} $M_{\odot}$ halo introduced in the previous chapter. We applied the orbit integration method developed in Chapter 2 to study the effects of baryonic physics on subhalo abundance near the centre of the halo. We found that the abundance of substructure near the centre of the halo was reduced by around 50%, approximately the same as the reduction

observed in the APOSTLE simulations in Chapter 2. When studied in projection, the number of objects along a given line of sight is reduced by around 30% when baryonic physics is included. In this chapter we also quantified how the properties of subhalos reported by the SUBFIND algorithm depend on both the distance from the centre of the main halo and the concentration of the main halo.

The goal of this thesis has been to study the effects of baryonic physics on dark matter halos and their substructure. We have shown that the impact is significant, and the uncertainties are large. There clearly remains much work to be done in this realm if future tests of the CDM paradigm are to make conclusive statements. We have not considered how a different implementation of baryonic physics will affect the subhalos of halos in the mass range relevant for lensing tests. The computational burden of simulating these halos at sufficiently high resolution means that we have not produced an estimate of the halo-to-halo scatter for the effects studied. Furthermore, a recent study (van den Bosch & Ogiya, 2018) has hinted at potential deficiencies in the modelling of halo-subhalo interactions. If the preliminary results of these studies are validated by subsequent investigations, many of the longstanding results in the simulation literature, as well as those in this thesis, will need to be revised.

Genuine progress on the question of the nature of dark matter must come from detection of the dark matter particle, if indeed such a detection is even possible. A deeper understanding of the properties of dark matter on an astrophysical level may well help to guide this search. From an astronomical perspective, future measurements of the properties of small scale structure have the potential to overturn the current consensus model of structure formation. However, it is clear that a great deal of progress in the modelling of baryonic physics must be made if any conclusions are to be drawn on either a fundamental or an astrophysical level.

Bibliography

Abbott B. P., et al., 2016, Physical Review Letters, 116, 061102

Adams J. J., et al., 2014, Astrophys. J., 789, 63

Agnello A., Evans N. W., 2012, Astrophys. J. Lett., 754, L39

Anderson M. E., Churazov E., Bregman J. N., 2015, Mon. Not. R. Astron. Soc., 452, 3905

Arias P., Cadamuro D., Goodsell M., Jaeckel J., Redondo J., Ringwald A., 2012, J. Cosmo. Astrophys., 2012, 013

Asaka T., Shaposhnikov M., 2005, Physics Letters B, 620, 17

Benitez-Llambay A., Frenk C. S., Ludlow A. D., Navarro J. F., 2018, arXiv e-prints, p. arXiv:1810.04186

Benson A. J., Frenk C. S., Sharples R. M., 2002, Astrophys. J., 574, 104

Berlind A. A., et al., 2003, Astrophys. J., 593, 1

Boehm C., Schaeffer R., 2005, Astron. Astrophys., 438, 419

Bœhm C., Schewtschenko J. A., Wilkinson R. J., Baugh C. M., Pascoli S., 2014, Mon. Not. R. Astron. Soc., 445, L31

Bolton A. S., Burles S., Koopmans L. V. E., Treu T., Moustakas L. A., 2006, Astrophys. J., 638, 703

Bolton A. S., Burles S., Koopmans L. V. E., Treu T., Gavazzi R., Moustakas L. A., Wayth R., Schlegel D. J., 2008, Astrophys. J., 682, 964

Bonaca A., Price-Whelan A. M., Hogg D. W., Conroy C., Caldwell N., Cargile P., Johnson B. D., 2019, in American Astronomical Society Meeting Abstracts. p. 214.03

Bose S., et al., 2017, Mon. Not. R. Astron. Soc., 464, 4520

Bovy J., 2015, Astrophys. J. Supp., 216, 29

Boyarsky A., Ruchayskiy O., Iakubovskyi D., Franse J., 2014, Physical Review Letters, 113, 251301

Boylan-Kolchin M., Bullock J. S., Kaplinghat M., 2011, Mon. Not. R. Astron. Soc., 415, L40

Brooks A. M., Zolotov A., 2014, Astrophys. J., 786, 87

Buchert T., 1994, Mon. Not. R. Astron. Soc., 267, 811

Bulbul E., Markevitch M., Foster A., Smith R. K., Loewenstein M., Randall S. W., 2014, Astrophys. J., 789, 13

Bullock J. S., Kravtsov A. V., Weinberg D. H., 2000, Astrophys. J., 539, 517

Burkert A., 1995, Astrophys. J. Lett., 447, L25

Burkert A., 2000, Astrophys. J. Lett., 534, L143

Carlberg R. G., Grillmair C. J., Hetherington N., 2012, Astrophys. J., 760, 75

Carr B., Kühnel F., Sandstad M., 2016, Phys. Rev. D, 94, 083504

Cautun M., van de Weygaert R., Jones B. J. T., 2013, Mon. Not. R. Astron. Soc., 429, 1286

Cautun M., Bose S., Frenk C. S., Guo Q., Han J., Hellwing W. A., Sawala T., Wang W., 2015, Mon. Not. R. Astron. Soc., 452, 3838

Colín P., Avila-Reese V., Valenzuela O., 2000, Astrophys. J., 542, 622

Crain R. A., et al., 2015, Mon. Not. R. Astron. Soc., 450, 1937

D'Onghia E., Springel V., Hernquist L., Keres D., 2010, Astrophys. J., 709, 1138

Davis M., Efstathiou G., Frenk C. S., White S. D. M., 1985, Astrophys. J., 292, 371

Despali G., Vegetti S., 2017, Mon. Not. R. Astron. Soc., 469, 1997

Despali G., Vegetti S., White S. D. M., Giocoli C., van den Bosch F. C., 2018, Mon. Not. R. Astron. Soc., 475, 5424

Diemand J., Kuhlen M., Madau P., 2007, Astrophys. J., 667, 859

Dodelson S., Widrow L. M., 1994, Physical Review Letters, 72, 17

Duffy L. D., van Bibber K., 2009, New Journal of Physics, 11, 105008

Einasto J., Kaasik A., Saar E., 1974, Nature, 250, 309

Erkal D., Belokurov V., 2015a, Mon. Not. R. Astron. Soc., 450, 1136

Erkal D., Belokurov V., 2015b, Mon. Not. R. Astron. Soc., 454, 3542

Erkal D., Belokurov V., Bovy J., Sanders J. L., 2016, Mon. Not. R. Astron. Soc., 463, 102

Errani R., Peñarrubia J., Laporte C. F. P., Gómez F. A., 2017, Mon. Not. R. Astron. Soc., 465, L59

Fattahi A., et al., 2016, Mon. Not. R. Astron. Soc., 457, 844

Flores R. A., Primack J. R., 1994, Astrophys. J. Lett., 427, L1

Franse J., et al., 2016, Astrophys. J., 829, 124

Garrison-Kimmel S., et al., 2017, preprint, (arXiv:1701.03792)

Genina A., et al., 2018, Mon. Not. R. Astron. Soc., 474, 1398

Gill S. P. D., Knebe A., Gibson B. K., 2005, Mon. Not. R. Astron. Soc., 356, 1327

Gilmore G., et al., 2012, The Messenger, 147, 25

Grand R. J. J., Springel V., Gómez F. A., Marinacci F., Pakmor R., Campbell D. J. R., Jenkins A., 2016, Mon. Not. R. Astron. Soc., 459, 199

Guth A. H., 1981, Phys. Rev. D, 23, 347

Hahn O., Carollo C. M., Porciani C., Dekel A., 2007, Mon. Not. R. Astron. Soc., 381, 41

Hellwing W. A., Frenk C. S., Cautun M., Bose S., Helly J., Jenkins A., Sawala T., Cytowski M., 2016, Mon. Not. R. Astron. Soc., 457, 3492

Herpich J., Stinson G. S., Rix H.-W., Martig M., Dutton A. A., 2017, Mon. Not. R. Astron. Soc., 470, 4941

Hopkins P. F., Kereš D., Oñorbe J., Faucher-Giguère C.-A., Quataert E., Murray N., Bullock J. S., 2014, Mon. Not. R. Astron. Soc., 445, 581

Hu W., Barkana R., Gruzinov A., 2000, Physical Review Letters, 85, 1158

Hubble E., 1929, Proceedings of the National Academy of Science, 15, 168

Hui L., Ostriker J. P., Tremaine S., Witten E., 2017, Phys. Rev. D, 95, 043541

Ibata R. A., Famaey B., Lewis G. F., Ibata N. G., Martin N., 2015, Astrophys. J., 805, 67

Jeltema T., Profumo S., 2015, Mon. Not. R. Astron. Soc., 450, 2143

Jiang L., Helly J. C., Cole S., Frenk C. S., 2014, Mon. Not. R. Astron. Soc., 440, 2115

Kazantzidis S., Magorrian J., Moore B., 2004, Astrophys. J., 601, 37

Kegerreis J. A., Eke V. R., Gonnet P. G., Korycansky D. G., Massey R. J., Schaller M., Teodoro L. F. A., 2019, arXiv e-prints, p. arXiv:1901.09934

Klypin A., Kravtsov A. V., Valenzuela O., Prada F., 1999, Astrophys. J., 522, 82

Koopmans L. V. E., 2005, Mon. Not. R. Astron. Soc., 363, 1136

LSST Science Collaboration et al., 2009, preprint, (arXiv:0912.0201)

Lacey C., Cole S., 1993, Mon. Not. R. Astron. Soc., 262, 627

Li R., Frenk C. S., Cole S., Gao L., Bose S., Hellwing W. A., 2016, Mon. Not. R. Astron. Soc., 460, 363

Li R., Frenk C. S., Cole S., Wang Q., Gao L., 2017, Mon. Not. R. Astron. Soc., 468, 1426

Linde A. D., 1982, Physics Letters B, 108, 389

Lovell M. R., et al., 2012, Mon. Not. R. Astron. Soc., 420, 2318

Lovell M. R., et al., 2016, preprint, (arXiv:1611.00010)

Lowing B., Jenkins A., Eke V., Frenk C., 2011, Mon. Not. R. Astron. Soc., 416, 2697

Lubimov V., Novikov E., Nozik V., Tretyakov E., Kosik V., 1980, Physics Letters B, 94, 266

Ludlow A. D., Schaye J., Schaller M., Richings J., 2019, arXiv e-prints, p. arXiv:1903.10110

Lynden-Bell D., 1976, Mon. Not. R. Astron. Soc., 174, 695

Macciò A. V., Kang X., Fontanot F., Somerville R. S., Koposov S., Monaco P., 2010, Mon. Not. R. Astron. Soc., 402, 1995

Malyshev D., Neronov A., Eckert D., 2014, Phys. Rev. D, 90, 103506

McConnachie A. W., et al., 2009, Nature, 461, 66

Moore B., 1994, Nature, 370, 629

Moore B., Ghigna S., Governato F., Lake G., Quinn T., Stadel J., Tozzi P., 1999, Astrophys. J. Lett., 524, L19

More S., Kravtsov A. V., Dalal N., Gottlöber S., 2011, Astrophys. J. Supp., 195, 4

Navarro J. F., Frenk C. S., White S. D. M., 1996, Astrophys. J., 462, 563

Neto A. F., et al., 2007, Mon. Not. R. Astron. Soc., 381, 1450

Newton O., Cautun M., Jenkins A., Frenk C. S., Helly J. C., 2018, Mon. Not. R. Astron. Soc., 479, 2853

Oh S.-H., et al., 2015, Astrophys. J., 149, 180

Okamoto T., Gao L., Theuns T., 2008, Mon. Not. R. Astron. Soc., 390, 920

Oman K. A., Marasco A., Navarro J. F., Frenk C. S., Schaye J., Benítez-Llambay A. r., 2019, Mon. Not. R. Astron. Soc., 482, 821

Onions J., et al., 2013, Mon. Not. R. Astron. Soc., 429, 2739

Ostriker J. P., Peebles P. J. E., Yahil A., 1974, Astrophys. J. Lett., 193, L1

Pakmor R., et al., 2017, Mon. Not. R. Astron. Soc., 469, 3185

Parzen E., 1962, Ann. Math. Statist., 33, 1065

Peebles P. J. E., 1982, Astrophys. J. Lett., 263, L1

Perlmutter S., et al., 1999, Astrophys. J., 517, 565

Perryman M. A. C., et al., 2001, Astron. Astrophys., 369, 339

Planck Collaboration et al., 2016, Astron. Astrophys., 596, A108

Pontzen A., Governato F., 2012, Mon. Not. R. Astron. Soc., 421, 3464

Pontzen A., Roškar R., Stinson G. S., Woods R., Reed D. M., Coles J., Quinn T. R., 2013, pynbody: Astrophysics Simulation Analysis for Python

Power C., Navarro J. F., Jenkins A., Frenk C. S., White S. D. M., Springel V., Stadel J., Quinn T., 2003, Mon. Not. R. Astron. Soc., 338, 14

Riemer-Sørensen S., 2016, Astron. Astrophys., 590, A71

Riess A. G., et al., 1998, Astrophys. J., 116, 1009

Rodríguez-Torres S. A., et al., 2016, Monthly Notices of the Royal Astronomical Society, 460, 1173

Rosenblatt M., 1956, Ann. Math. Statist., 27, 832

Rubin V. C., Ford Jr. W. K., 1970, Astrophys. J., 159, 379

Rubin V. C., Ford Jr. W. K., Thonnard N., 1980, Astrophys. J., 238, 471

Saff E. B., Kuijlaars A. B. J., 1997, The Mathematical Intelligencer, 19, 5

Sawala T., Frenk C. S., Crain R. A., Jenkins A., Schaye J., Theuns T., Zavala J., 2013, Mon. Not. R. Astron. Soc., 431, 1366

Sawala T., et al., 2016, Mon. Not. R. Astron. Soc., 457, 1931

Sawala T., Pihajoki P., Johansson P. H., Frenk C. S., Navarro J. F., Oman K. A., White S. D. M., 2017, Mon. Not. R. Astron. Soc., 467, 4383

Schaller M., Dalla Vecchia C., Schaye J., Bower R. G., Theuns T., Crain R. A., Furlong M., McCarthy I. G., 2015, Mon. Not. R. Astron. Soc., 454, 2277

Schaye J., et al., 2015, Mon. Not. R. Astron. Soc., 446, 521

Schewtschenko J. A., Wilkinson R. J., Baugh C. M., Bœhm C., Pascoli S., 2015, Mon. Not. R. Astron. Soc., 449, 3587

Schneider A., Smith R. E., Macciò A. V., Moore B., 2012, Mon. Not. R. Astron. Soc., 424, 684

Schramm D. N., Steigman G., 1981, Astrophys. J., 243, 1

Scott D., 2015, Multivariate Density Estimation: Theory, Practice, and Visualization, 2 edn. Wiley

Sheth R. K., Tormen G., 1999, Monthly Notices of the Royal Astronomical Society, 308, 119

Somerville R. S., 2002, Astrophys. J. Lett., 572, L23

Spergel D. N., Steinhardt P. J., 2000, Physical Review Letters, 84, 3760

Springel V., 2011, in Alves J., Elmegreen B. G., Girart J. M., Trimble V., eds, IAU Symposium Vol. 270, Computational Star Formation. pp 203–206, doi:10.1017/S1743921311000378

Springel V., White S. D. M., Tormen G., Kauffmann G., 2001, Mon. Not. R. Astron. Soc., 328, 726

Springel V., et al., 2005, Nature, 435, 629

Springel V., et al., 2008, Mon. Not. R. Astron. Soc., 391, 1685

Starobinsky A. A., 1980, Physics Letters B, 91, 99

Strigari L. E., Frenk C. S., White S. D. M., 2010, Mon. Not. R. Astron. Soc., 408, 2364

Taylor A. N., Dye S., Broadhurst T. J., Benítez N., van Kampen E., 1998, Astrophys. J., 501, 539

The Dark Energy Survey Collaboration 2005, ArXiv Astrophysics e-prints,

Tinker J., Kravtsov A. V., Klypin A., Abazajian K., Warren M., Yepes G., Gottlöber S., Holz D. E., 2008, The Astrophysical Journal, 688, 709

Vegetti S., Lagattuta D. J., McKean J. P., Auger M. W., Fassnacht C. D., Koopmans L. V. E., 2012, Nature, 481, 341

Vogelsberger M., et al., 2014, Nature, 509, 177

Walker M. G., Peñarrubia J., 2011, The Astrophysical Journal, 742, 20

Warren M. S., Abazajian K., Holz D. E., Teodoro L., 2006, Astrophys. J., 646, 881

Wetzel A. R., Hopkins P. F., Kim J.-h., Faucher-Giguère C.-A., Kereš D., Quataert E., 2016, Astrophys. J. Lett., 827, L23

Wolf J., Martinez G. D., Bullock J. S., Kaplinghat M., Geha M., Muñoz R. R., Simon J. D., Avedo F. F., 2010, Monthly Notices of the Royal Astronomical Society, 406, 1220

Yoshida N., Springel V., White S. D. M., Tormen G., 2000, Astrophys. J., 544, L87

Yurin D., Springel V., 2015, Mon. Not. R. Astron. Soc., 452, 2367

Zel'dovich Y. B., 1970, Astron. Astrophys., 5, 84

Zwicky F., 1937, Astrophys. J., 86, 217

van den Bosch F. C., Ogiya G., 2018, Monthly Notices of the Royal Astronomical Society, 475, 4066